Adaptive Semi-Implicit Particle-in-cell Simulations of Magnetotail Reconnection Onset

by

Talha Arshad

A dissertation submitted in partial fulfillment
of the requirements for the degree of
Doctor of Philosophy
(Climate and Space Sciences and Engineering)
in The University of Michigan
2026

Doctoral Committee:

Assistant Research Scientist Yuxi Chen, Co-Chair
Research Professor Gabor Toth, Co-Chair
Professor Krzysztof Fidkowski
Professor Tuija Pulkkinen
Professor Shasha Zou

Talha Arshad
talhaa@umich.edu
ORCID iD: 0000-0003-4704-0942

© Talha Arshad 2026

DEDICATION

To my family, whose unwavering support and sacrifices have made this journey possible. Your encouragement has been a constant source of strength through every challenge. To my mentors and teachers, for their guidance, patience, and inspiration, which have shaped not only this work but also my growth as a person and researcher.

ACKNOWLEDGEMENTS

I would like to acknowledge my advisor, Professor Gabor Tóth, whose support and guidance have been invaluable throughout my Ph.D. journey. He has always made himself available whenever I needed assistance. He maintained an open-door policy and was always willing to help whenever I had questions or needed advice, even if it meant pausing his own work. I am deeply thankful for his support and for the countless science- and politics-filled conversations we shared over coffee.

I would also like to thank Dr. Yuxi Chen for his mentorship and kind support. I learned a great deal from him. At the very beginning of my research, Yuxi taught me the fundamentals of high-level C++ programming. He was generous with his time and always willing to help with a smile and a positive attitude.

I am also grateful to Dr. Timothy Keebler for teaching me how to install and run the SWMF code, as well as for the countless friendly exchanges we shared. Tim is truly inspirational. He is kind to everyone and universally loved by all. I am fortunate to have had the opportunity to work with him and to call him my friend.

TABLE OF CONTENTS

DEDICATION ii

ACKNOWLEDGEMENTS iii

LIST OF FIGURES vii

LIST OF TABLES xi

LIST OF ACRONYMS xii

LIST OF SYMBOLS xiii

ABSTRACT xiv

CHAPTER

1 Introduction 1

1.1 Solar Wind 1
1.2 Earth's Magnetosphere 2
1.3 Scale Separation in Space Plasma Physics 4
1.4 Interaction of Solar Wind with Earth's Magnetosphere 5
1.4.1 Dungey Cycle 5
1.4.2 Magnetic Reconnection 6
1.4.3 Onset of Tail Reconnection 7
1.5 Global Dynamics and the Magnetohydrodynamics (MHD) model 8
1.6 Kinetic Effects and the Particle-In-Cell (PIC) method 9
1.7 Particle-In-Cell method 10
1.7.1 Explicit PIC 12
1.7.2 Fully Implicit PIC 13
1.7.3 Semi-Implicit PIC 13
1.8 Multi-scale Modeling and Coupling MHD with PIC 15
1.9 Need for Adaptive Mesh Refinement (AMR) in Semi-Implicit PIC 15
1.10 Overview of the Thesis 16

2 Adaptive Mesh Refinement in Semi-Implicit Particle-in-Cell Method . . 17

2.1 Introduction 17
2.2 AMR semi-implicit particle in cell method 18

2.2.1 Grid Structure . . . 20
2.2.2 Refinement Initialization . . . 21
2.2.3 Particles . . . 21
2.2.4 Updating Electric Field . . . 22
2.2.5 Moving Particles . . . 23
2.2.6 Updating Magnetic Field . . . 23
2.2.7 Synchronizing Fields . . . 23
2.2.8 Particle Merging and Splitting . . . 24
2.2.9 Pre-splitting . . . 24
2.2.10 Gauss's Law Correction . . . 25
2.2.11 Dynamic AMR . . . 27
2.2.12 Time step . . . 27
2.3 Numerical tests . . . 28
2.3.1 Light wave test . . . 28
2.3.2 Fast wave test . . . 30
2.3.3 Magnetic reconnection tests . . . 33
2.4 Speed-up analysis of AMR PIC . . . 42
2.4.1 Fast wave test speed-up . . . 44
2.4.2 Multi-level (R=2) static reconnection test speed-up . . . 44
2.4.3 Single (R=4) static refinement reconnection test speed-up . . . 44
2.4.4 Single (R=4) adaptive refinement reconnection test speed-up . . . 44
2.5 Conclusions . . . 44
3 Modeling Kinetic Reconnection Onset in Global Magnetospheric Simulations . . . 46
3.1 Introduction . . . 46
3.2 Model Description . . . 48
3.3 Simulation Results . . . 50
3.3.1 Resolving the electrons scale . . . 50
3.3.2 Effect of ion-electron mass ratio . . . 53
3.3.3 Effect of kinetic scaling . . . 55
3.3.4 Optimal PIC parameters . . . 57
3.3.5 Current Sheet Thickness . . . 57
3.3.6 Comparison with Ideal and Hall MHD . . . 58
3.3.7 Kinetic Reconnection onset . . . 59
3.4 Conclusions . . . 64
4 Modeling Tail Reconnection Onset with AMR-PIC . . . 66
4.1 Simulation Setup . . . 66
4.2 Results . . . 67
4.2.1 Timing and Location of Reconnection Onset . . . 67
4.2.2 Before Reconnection Onset . . . 67
4.2.3 After Reconnection Onset . . . 69
5 Conclusion and Future Work . . . 72

BIBLIOGRAPHY 74

LIST OF FIGURES

FIGURE

1.1 Schematic of the solar wind interplanetary magnetic field (IMF) lines according to the Parker spiral model (from Hundhausen, 1972) [28]. 2
1.2 Schematic showing the meridional cross-section of Earth's magnetosphere. The dotted line represents the bow shock. The magnetopause, lobes, and current sheet are also shown (from Hunsucker, 2002) [29]. 3
1.3 Cartoon showing the different stages of the Dungey cycle (from Eastwood et al., 2015) [18]. 5
1.4 Schematic that shows different regions around a magnetic reconnection site (from Lee et al., 2020) [35]. 7

2.1 Schematics of the AMR grid structure. Left: Three refinement levels are shown in black, red and green. Right: Refinement levels with surrounding ghost cells shown by dotted lines. 20
2.2 The interpolation function W^L used to interpolate between grid level L and particles is based on the b_1 spline function. 21
2.3 Particles belonging to three different refinement levels are shown in black, blue, red, purple and green. The ghost cells of the grid levels are indicated by dotted lines. Black particles belong to level 0, blue particles belong to level 0 but are inside the ghost cells of level 1, red particles belong to level 1, purple particles belong to level 1 but are inside the ghost cells of level 2 and green particles belong to level 2. 22
2.4 Gauss's Law enforcement at a grid resolution change. The extent of the fine interpolation function W^L is shown by the blue dotted square around the blue particle on the left side of the dashed purple line. It does not reach any fine cell centers (black dots), so this particle can be moved without changing the net charge in the fine grid. The fine interpolation function (red dotted square) of the red particle on the right of the dashed purple line does reach the fine cell centers, therefore these particles are not moved when the Gauss Law error is eliminated on the coarse grid. 26
2.5 Light wave test solution at $t = 384$. The E_y component of the electric field is shown. The base grid resolution is $\Delta x_0 = 1$. The white rectangle surrounds the refined region with $\Delta x_1 = 1/2$. 29
2.6 Light wave test. E_z error at $t = 384$. Left: Base grid resolution $\Delta x_0 = 1$. Right: Base grid resolution $\Delta x_0 = 1/2$. 29

2.7 Fast wave test solution at $t = 600$. Top left: Magnetic field B_y. Top right: X component of the ion velocity $U_{x,i}$. Bottom left: Number of ion particles per cell PPC_i. Bottom right: Magnitude of Gauss's Law error $|\nabla \cdot \mathbf{E} - 4\pi q_c|$. 30
2.8 Comparison between AMR and high resolution uniform grid fast wave test. B_y, ion velocity $U_{x,i}$ and electron velocity $U_{x,e}$ are shown at $t = 600$ for the AMR simulation (top row) and uniform grid simulation (bottom row). The white box shows the refined region in the AMR simulation. 32
2.9 Energy conservation plot for the fast wave test. The x-axis represents time, while the y-axis represents the change in total energy of the system normalized to the initial energy. Uniform grid energy plot with two different resolutions as well as AMR energy plot with varying target particles-per-cell number, are shown. . . . 33
2.10 2D double current sheet reconnection test with two levels of refinement at time $t = 400$. Each white rectangle shows a factor of 2 refinement change. Top left: Out-of-plane Hall field B_z. The other three panels show the three off-diagonal elements of the electron pressure tensor. 35
2.11 Comparison of various quantities near the reconnection site at $t = 400$ for three simulations. The left and right columns show the solution obtained on uniform grids with $\Delta x = 0.2$ and $\Delta x = 0.05$, respectively. The middle column shows the refined grid level $L = 2$ with $\Delta x_2 = 0.05$ of the AMR simulation shown in Figure 2.10. The six rows show the out-of-plane magnetic field B_z, electron velocity component $U_{x,e}$, three off-diagonal pressure tensor elements $P_{xz,e}$, $P_{xy,e}$, $P_{yz,e}$ and the net charge q_c. 36
2.12 Change in energy plot for the multi-level AMR reconnection test. The left figure shows the change in total energy normalized to the initial energy. The middle figure shows the normalized change of energy for ions, while the right figure shows the same for electrons. The results for uniform grid solutions as well as AMR results are shown. 37
2.13 The region of interest to study particle velocity distribution functions is shown at the top. Electron and ion velocity space distributions at $t = 400$ for the multi-level AMR simulation and uniform grid simulations are shown below. . . 38
2.14 Reconnection test results at $t = 400$ with a single AMR level with refinement ratio $R = 4$. The out-of-plane Hall field B_z and the off-diagonal elements of the electron pressure tensor are shown. The white rectangle shows a factor of 4 refinement change ($R = 4$) 39
2.15 Reconnection test results with a single AMR level with refinement ratio $R = 4$ that is moving together with the reconnection site in the $-x$ direction. The $P_{xz,e}$ element of the electron pressure tensor is shown at four different times. The white rectangle shows the dynamically adapted refined region. 40
2.16 Reconnection test with moving reconnection sites. The white rectangles show two disconnected stationary single-level refinements with refinement ratio $R = 2$. The $P_{xz,e}$ element of the electron pressure tensor is shown at four different times. The white rectangles show the refined regions. 41

3.1 Overview of the simulation setup. The MHD domain spans across the entire figure while the PIC domain is represented by the white rectangle. 48

3.2 Density and magnetic field lines as the magnetotail elongates. The top panel is at t = 50 minutes, the middle panel is at t = 60 minutes, and the bottom panel is at t = 70 minutes. 49
3.3 Electron velocity in the x-direction with $f = 16$, $m_i/m_e = 25$ for three runs with PIC grid resolutions $\Delta x = 1/8$, 1/16, and $1/32\,R_E$ (top to bottom) at $t = 95\,\mathrm{m}$. The reconnection occurs at about the same location $x \approx -15.4\,R_E$ and at the same time for the $\Delta x = 1/16$ and $1/32\,R_E$ runs, while the reconnection occurs earlier and closer to Earth for the $\Delta x = 1/8\,R_E$ run. 50
3.4 Out-of-plane current density, J_y, at the onset of reconnection for three simulations with grid resolutions $\Delta x = 1/8\,R_E$, $1/16\,R_E$, and $1/32\,R_E$, using $f = 16$ and $m_i/m_e = 25$. The profiles for the $\Delta x = 1/16\,R_E$ and $1/32\,R_E$ cases closely overlap, indicating convergence at these resolutions. In contrast, the $\Delta x = 1/8\,R_E$ case exhibits a broader profile, implying a thicker current sheet and a lack of grid convergence at this coarser resolution. 52
3.5 Off-diagonal electron pressure tensor components $P_{xz,e}$, $P_{xy,e}$, and $P_{yz,e}$ after the reconnection site has fully formed for the $\Delta x = 1/8\,R_E$, $\Delta x = 1/16\,R_E$, $\Delta x = 1/32\,R_E$ (top to bottom) runs with $f = 16$ and $m_i/m_e = 25$. 53
3.6 Electron velocity in the x-direction at $t = 84, 86.5, 89, 91.5$ minutes for f=16 with mass ratio $m_i/m_e = 25$ (left) and $m_i/m_e = 100$ (right). The reconnection starts at roughly the same time and location for both runs, but the $m_i/m_e = 100$ case has extra flux ropes and reconnection sites that develop in the tail. 54
3.7 Electron number density, electron velocity in the x-direction, and ion velocity in the x-direction for $m_i/m_e = 25$ (left) and $m_i/m_e = 100$ (right) at t = 92 minutes. Both simulations show similar electron number densities and ion velocities, while the electron velocity is higher for the $m_i/m_e = 100$ case. The electron jet in the $m_i/m_e = 100$ case is also narrower and shorter than the $m_i/m_e = 25$ case. . . . 55
3.8 Electron number density, electron velocity in the x-direction, and ion velocity in the x-direction for $f = 16$ (left) at t = 76 minutes and $f = 8$ (right) at t = 82 minutes. 56
3.9 Velocity in the x-direction for three ideal MHD simulations with different grid resolutions Δ x = 1/8, 1/16, 1/32 R_E (top to bottom). While the reconnection happens at similar locations, the jet speeds vary significantly. 58
3.10 Velocity in the x-direction for Hall MHD simulation with different grid resolutions $\Delta x = 1/8, 1/16, 1/32\,R_E$ from top to bottom. Note the variation of the locations of the X-line and the jet speeds. 59
3.11 Electron temperature anisotropy $T_{e\perp}/T_{e\parallel}$ (left) and ion temperature anisotropy $T_{i\perp}/T_{i\parallel}$ (right) at t = 67, 72, 77, and 82 minutes (top to bottom). An electron temperature anisotropy of $T_{e\perp}/T_{e\parallel} \approx 1.1 - 1.3$ develops in the current sheet just before reconnection onset. 60
3.12 B_z and electron velocity in the x-direction ($U_{x,e}$) along $z = 0$ at different times. Every $B_z = 0$ crossing acts as a seed for a reconnection site to develop. 61
3.13 Electron and ion velocities in the x-direction at t = 85 minutes. 61
3.14 Electron and ion velocities in the x-direction at t = 92 minutes. 62

3.15 Total, parallel, and perpendicular electron and ion temperatures at t = 92 minutes. The electrons are heated preferentially in the perpendicular direction near the neutral line, while the ions are heated preferentially in the parallel direction near the neutral line. 63
3.16 The ratio of ion to electron temperature at t = 92 minutes. The ion temperature in the electron diffusion region can be roughly 8 to 10 times higher than the electron temperature. 64

4.1 AMR grid setup for the reconnection onset problem. The black rectangle represents the refined region. 66
4.2 Comparison of electron number density, electron velocity, ion velocity, electron pressure, ion pressure, and out-of-plane current density between uniform grid (right) and AMR-PIC (left) simulations at 80 minutes, before reconnection onset. Refined region is outlined by the black rectangle. 68
4.3 Comparison of electron and ion temperature anisotropy between uniform grid (right) and AMR-PIC (left) simulations at 82 minutes, before reconnection onset. Refined region is outlined by the black rectangle. 69
4.4 Comparison of electron number density, electron velocity, and ion velocity between uniform grid (right) and AMR-PIC (left) simulations at 85 minutes, after reconnection onset. 70
4.5 Comparison of electron number density, electron velocity, and ion velocity between uniform grid (right) and AMR-PIC (left) simulations at 92 minutes, after reconnection onset. Refined region is outlined by the black rectangle. 70
4.6 Comparison of ion to electron temperature ratio between uniform grid (top) and AMR-PIC (bottom) simulations at 92 minutes, after reconnection onset. 71

LIST OF TABLES

TABLE

3.1 Timing and location of reconnection onset for different PIC grid resolutions. . . 51
3.2 Timing and location of reconnection onset for different kinetic scaling factors. . 56
3.3 Current sheet thickness δ at reconnection onset for different scaling factors f and mass ratios m_i/m_e using the converged grid resolution Δx_c. For all runs, $\delta \approx 3d_e$. 57

4.1 Timing and location of reconnection onset for uniform grid and AMR-PIC simulations. 67

LIST OF ACRONYMS

IMF Interplanetary Magnetic Field

MHD Magnetohydrodynamics

PIC Particle-in-Cell

AMR Adaptive Mesh Refinement

FLEKS Flexible Exascale Kinetic Simulation

MHD-EPIC Magnetohydrodynamics with Embedded Particle-in-Cell

MHD-AEPIC Magnetohydrodynamics with Adaptively Embedded Particle-in-Cell

LIST OF SYMBOLS

ρ	Density
$\mathbf{u}$	Velocity
$\mathbf{B}$	Magnetic field
$\mathbf{E}$	Electric field
$\mathbf{J}$	Current density
$\mathbf{v}_p$	Particle velocity
$\mathbf{x}_p$	Particle position
q_p	Particle charge
m_p	Particle mass
Δt	Time step
Δx	Spatial grid size
λ_D	Debye length
ω_{pe}	Electron plasma frequency

ABSTRACT

Fluid models such as magnetohydrodynamics (MHD) have proven to be very useful for studying the global structure and dynamics of Earth's magnetosphere with modest computational cost. However, MHD models ignore kinetic effects, which can be important in certain regions of the magnetosphere. These kinetic effects can lead to phenomena such as magnetic reconnection, which can change magnetic topology and hence lead to changes in the global structure of the magnetosphere. These kinetic effects can be captured by the particle-in-cell (PIC) method, which is a powerful tool for studying kinetic plasma physics. However, PIC simulations can be computationally very expensive, especially for large-scale systems like Earth's magnetosphere, where the separation of global and kinetic scales can be several orders of magnitude. This has prompted the use of coupled MHD-PIC models, where the PIC method is localized to small regions of interest and the rest of the domain is modeled with MHD to reduce computational cost. Even with coupled MHD-PIC models, the computational cost to well resolve electron scales in a global magnetospheric simulation can be prohibitively expensive.

To address this issue, a novel semi-implicit PIC method with adaptive mesh refinement (AMR) is developed in the first part of this thesis. This AMR-PIC method allows for the resolution of electron-scale physics only in small regions within the PIC domain, while using a coarser grid elsewhere. This enables us to resolve electron-scale physics in regions of interest, like the vicinity of magnetic reconnection sites, while keeping the computational cost manageable. The AMR-PIC method supports multiple refinement levels and different refinement ratios, which allows for flexible resolution of electron scale physics in different regions of the domain.

The second part of the thesis applies the Magnetohydrodynamics with Embedded Particle-in-Cell (MHD-EPIC) model to study the onset of reconnection in Earth's magnetotail. MHD-EPIC is a coupled MHD-PIC model as described above. Using a PIC region with a uniform grid, a robust convergence criterion is identified for the grid resolution required to accurately capture the reconnection onset time and location as well as the microphysics of the reconnection region. The impact of the kinetic scaling factor and ion-to-electron mass ratio on the reconnection onset is also studied, and recommendations for optimal parameters are provided. The optimal parameters are then used to perform simulations that satisfy the

convergence criterion, and the microphysics of the reconnection onset process is studied. We find that irrespective of the scaling factor and mass ratio, the current sheet thickness at the reconnection site at the onset time is roughly 3 electron inertial lengths (d_e). We also find that a grid resolution of roughly 1.5 cells per d_e is required to accurately capture the reconnection onset process. An electron temperature anisotropy of $T_{e\perp}/T_{e\parallel} \sim 1.1 - 1.3$ develops in the current sheet just before reconnection onset, which is consistent with previous studies [36].

The third part of the thesis embeds the AMR-PIC method into the MHD-EPIC model to reproduce the results of the uniform grid PIC simulations and show that localized resolution of electron scale physics can capture similar physics as uniform grid PIC simulations. This shows the potential of the AMR-PIC method to be used in future global magnetospheric simulations to enable us to resolve all scales, ranging from the global scales to the electron scales, while keeping the computational cost manageable.

CHAPTER 1

Introduction

1.1 Solar Wind

The sun is the primary source of energy for Earth and the entire solar system. One major medium through which the sun and Earth interact is the solar wind. The solar wind is a stream of charged particles (mostly hydrogen ions and electrons) emitted from the sun's corona. The large temperature gradient between the corona and interplanetary space causes the solar atmosphere to expand and escape the sun's gravity, creating the solar wind. Initially, the solar wind was considered to be in hydrostatic equilibrium. However, in 1951, Biermann [5] suggested that the solar wind has a velocity between 500 km/s and 1500 km/s by observing comet tails. Eugene Parker [43, 42] analyzed the solar wind and showed that the solar wind must be supersonic due to acceleration by the pressure gradient. Parker also predicted that the interplanetary magnetic field (IMF) carried by the solar wind would be spiral-shaped (Figure 1.1) due to the sun's rotation. This spiral-shaped IMF is called the Parker spiral.

The first continuous solar wind observations were made by the Mariner-2 spacecraft and were reported in 1965 by Neugebauer and Snyder [52]. According to their observations, the solar wind velocity varied from 300 km/s to 700 km/s, and the density varied from 1 to 80 particles per cubic centimeter. The average density was around 5 particles per cubic centimeter.

The solar wind is generally categorized into two types:

- **Fast Solar Wind:** The fast solar wind has a velocity of around 750 km/s and originates from coronal holes. Coronal holes have open magnetic field lines and, therefore, solar wind plasma escapes easily. The composition of the fast solar wind is similar to the Sun's photosphere. Fast solar wind is less dense and has a lower electron temperature compared to the slow solar wind.

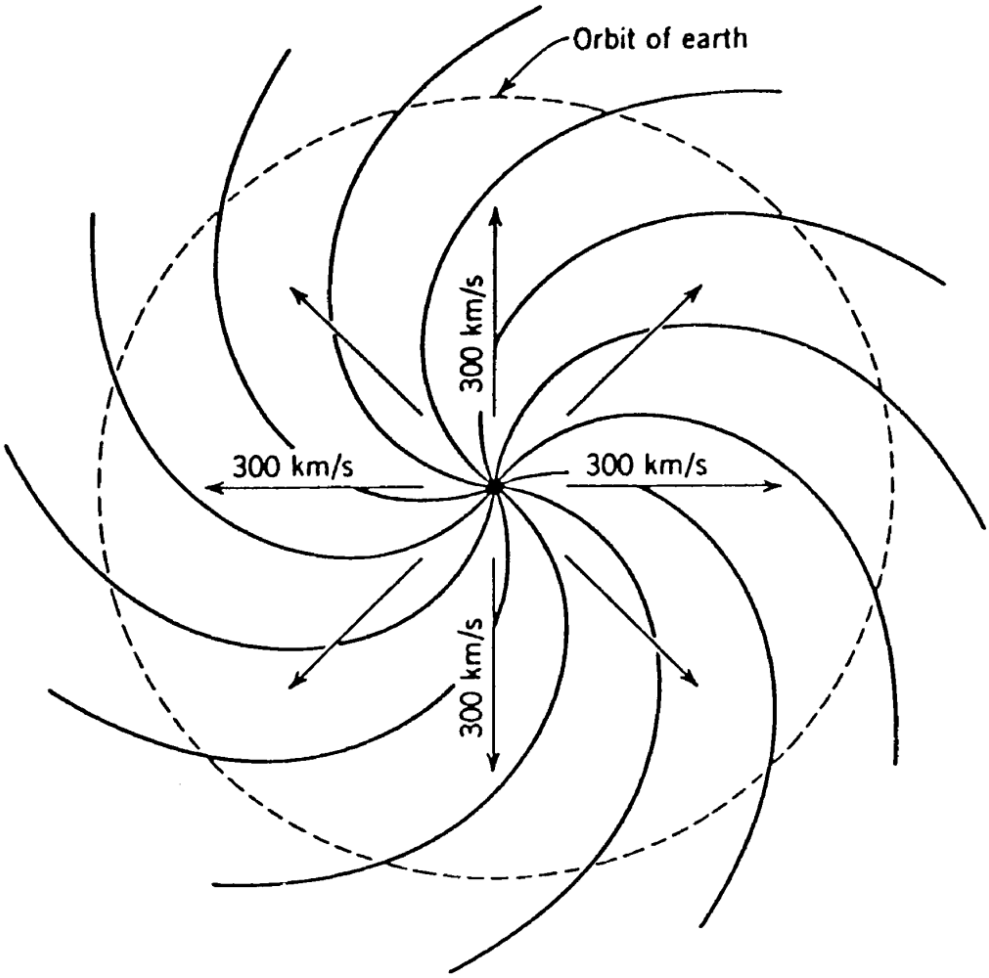


Figure 1.1: Schematic of the solar wind interplanetary magnetic field (IMF) lines according to the Parker spiral model (from Hundhausen, 1972) [28].

- **Slow Solar Wind:** The slow solar wind has a velocity of around 400 km/s and typically originates from coronal streamers. Coronal streamers are regions of closed magnetic field lines, which makes it harder for solar wind plasma to escape. The composition of slow solar wind is similar to the Sun's corona. Slow solar wind is roughly twice as dense as fast solar wind and has a higher electron temperature.

1.2 Earth's Magnetosphere

The Earth has a magnetic field that is generated by the motion of molten iron in the core. This magnetic field can be approximated as a dipole of strength 31,000 nT at Earth's surface. When this magnetic field interacts with the solar wind, it is stretched and deformed to form Earth's magnetosphere, as shown in Figure 1.2.

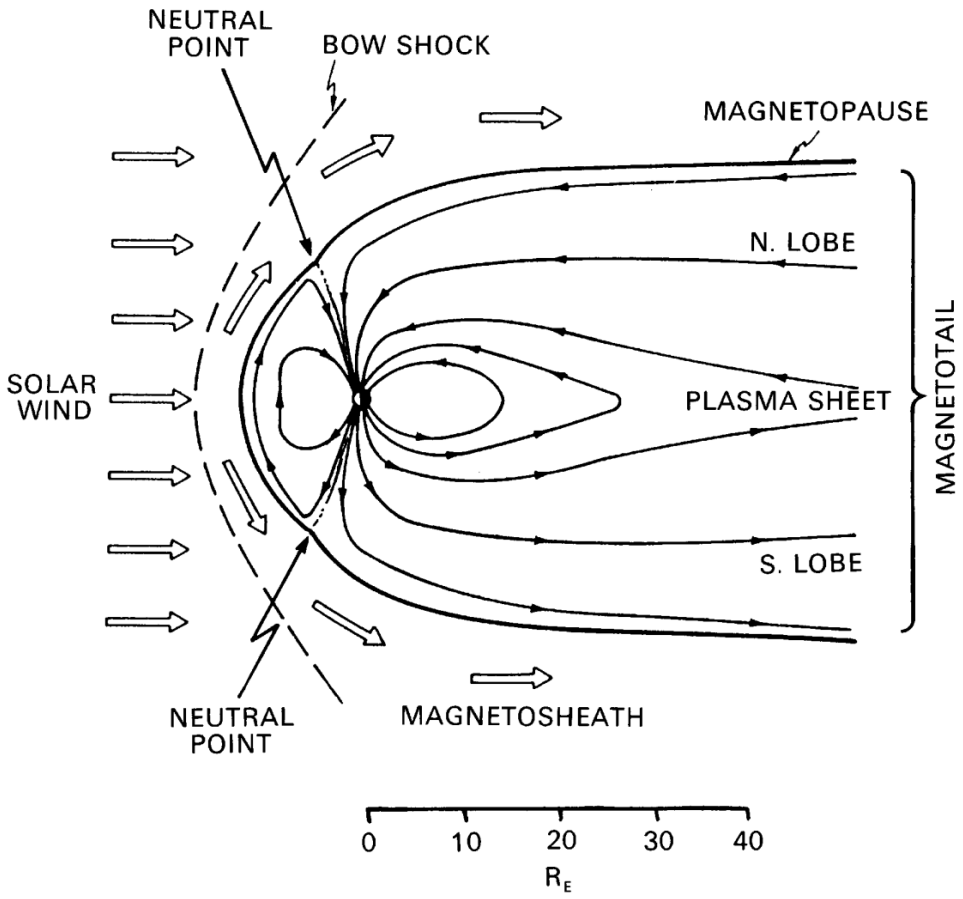


Figure 1.2: Schematic showing the meridional cross-section of Earth's magnetosphere. The dotted line represents the bow shock. The magnetopause, lobes, and current sheet are also shown (from Hunsucker, 2002) [29].

The magnetosphere is the space around Earth where Earth's magnetic field dominates and governs the motion of particles. The magnetopause is the boundary between the solar wind and the magnetosphere. There is a bow shock (dashed line) in front of the magnetopause on the dayside where the solar wind is decelerated to subsonic conditions. The magnetotail is the region on the nightside where magnetic field lines are stretched. The north and south lobes of the magnetotail are regions of low density and high magnetic field strength. The region between these lobes is the current sheet, where the magnetic field strength becomes low, and the density becomes high.

1.3 Scale Separation in Space Plasma Physics

The magnetosphere involves processes that span a very large range of spatial and temporal scales. These scales can vary from global scales down to the ion and electron scales. For the magnetosphere, the global scale (d_g) is usually characterized by the dayside magnetopause standoff distance ($\sim 10R_E$). Ion scales are typically characterized by the ion inertial length (d_i), and electron scales are characterized by the electron skin depth (d_e).

$$d_g \sim 10R_E \tag{1.1}$$

$$d_i = \sqrt{\frac{m_i}{q_i^2 \mu_0 n_i}} = \frac{m_i}{q_i} \frac{1}{\sqrt{\mu_0 \rho_i}} \tag{1.2}$$

$$d_e = \sqrt{\frac{m_e}{q_e^2 \mu_0 n_e}} = \frac{m_e}{q_e} \frac{1}{\sqrt{\mu_0 \rho_e}} \tag{1.3}$$

The ion inertial length (d_i) is the scale at which the ions decouple from the magnetic field. Similarly, the electron skin depth (d_e) is the scale at which electrons decouple from the magnetic field. d_i and d_e are also the characteristic length scales of the ion and electron diffusion regions in magnetic reconnection (discussed in section 1.4.2). m_i and m_e are the ion and electron masses respectively, and q_i and q_e are the ion and electron charges respectively, μ_0 is the permeability of free space and ρ_i and ρ_e are the ion and electron mass densities respectively.

Typical values of these scales in Earth's magnetotail are as follows:

$$d_g \sim 10R_E \sim 6.4 \times 10^7 m \tag{1.4}$$

$$d_i \sim 500km \sim 10^6 m \tag{1.5}$$

$$d_e \sim 10km \sim 10^4 m \tag{1.6}$$

These three scales are the most relevant scales for understanding the global magnetospheric dynamics and processes like magnetic reconnection. The large-scale separation between these scales makes it very difficult to model the magnetosphere using a single method (discussed more in section 1.8). Some other scales relevant to kinetic plasma physics are the Debye length (λ_D) and the electron plasma frequency (ω_{pe}), which are given by:

$$\lambda_D = \sqrt{\frac{\epsilon_0 k_B T_e}{n_e q_e^2}} \tag{1.7}$$

$$\omega_{pe} = \sqrt{\frac{n_e q_e^2}{\epsilon_0 m_e}} \tag{1.8}$$

The Debye length is the length scale at which the plasma can shield out electric fields, and the electron plasma frequency is the frequency at which electrons oscillate in response to an electric field. The Debye length and the inverse of the electron plasma frequency are much smaller than the ion scales and global scales. Typically, the Debye length in Earth's magnetotail is around 500 m, and the electron plasma frequency is around 10 kHz. These scales are not relevant for understanding the global magnetospheric dynamics and processes like magnetic reconnection, but they need to be resolved in explicit Particle-in-Cell (PIC) simulations (discussed in section 1.7.1).

1.4 Interaction of Solar Wind with Earth's Magnetosphere

The interaction of the solar wind with Earth's magnetosphere is a dynamic and multi-scale plasma phenomenon. The solar wind and the interplanetary magnetic field (IMF) carried by the solar wind interact with Earth's magnetic field and lead to a global circulation pattern known as the Dungey cycle.

1.4.1 Dungey Cycle

The Dungey cycle [17] is a global transport pattern of plasma and magnetic flux in the magnetosphere. A cartoon showing the different stages of the Dungey cycle is shown in Figure 1.3.

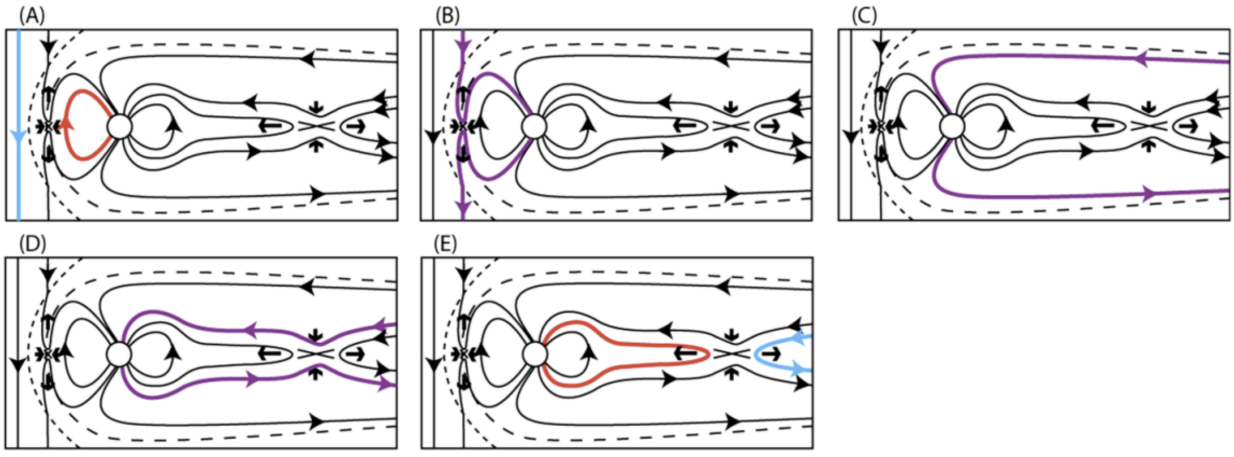


Figure 1.3: Cartoon showing the different stages of the Dungey cycle (from Eastwood et al., 2015) [18].

The Dungey cycle is heavily dependent on magnetic reconnection. The details of magnetic reconnection are discussed in section 1.4.2. The main stages of the Dungey cycle are as follows:
(A) The closed field lines (red) on the dayside magnetopause reconnect with the IMF field lines (blue).
(B) Magnetic reconnection (discussed in section 1.4.2) opens the closed field lines that are now connected to the solar wind on one end and to Earth on the other end (purple).
(C) These open field lines are dragged by the solar wind towards the magnetotail (purple).
(D) The magnetotail stretches and thins as more open field lines are added to the tail.
(E) Eventually, the tail becomes thin enough for reconnection to occur in the tail, and the open field lines reconnect to form closed field lines connected to Earth (red).

The Dungey cycle is a continuous process and leads to the conservation of overall magnetic flux in the magnetosphere over long timescales. The Dungey cycle is the fundamental mechanism through which energy and momentum from the solar wind are transferred into the magnetosphere. How much energy and momentum is transferred depends on the rate of reconnection at the dayside magnetopause. During periods of southward IMF, the reconnection rate is high and the magnetic flux transport through the magnetosphere increases. The Dungey cycle is the main driver for many space weather phenomena, such as geomagnetic storms, auroras, ring current, etc.

1.4.2 Magnetic Reconnection

Magnetic reconnection is a fundamental kinetic plasma process that leads to the explosive conversion of energy stored in the magnetic field into ion and electron kinetic energy [7, 61]. Magnetic reconnection breaks the frozen-in condition and changes the magnetic field topology by letting particles cross magnetic field lines [1]. A simplified schematic of magnetic reconnection is shown in Figure 1.4. The ion diffusion region is the region where the ions decouple from the magnetic field and no longer follow the frozen-in condition. Similarly, electrons break the frozen-in condition in the electron diffusion region, which is much smaller than the ion diffusion region. The inflow region is the region where plasma flows towards the reconnection site, and the outflow region is the region where plasma flows away from the reconnection site.

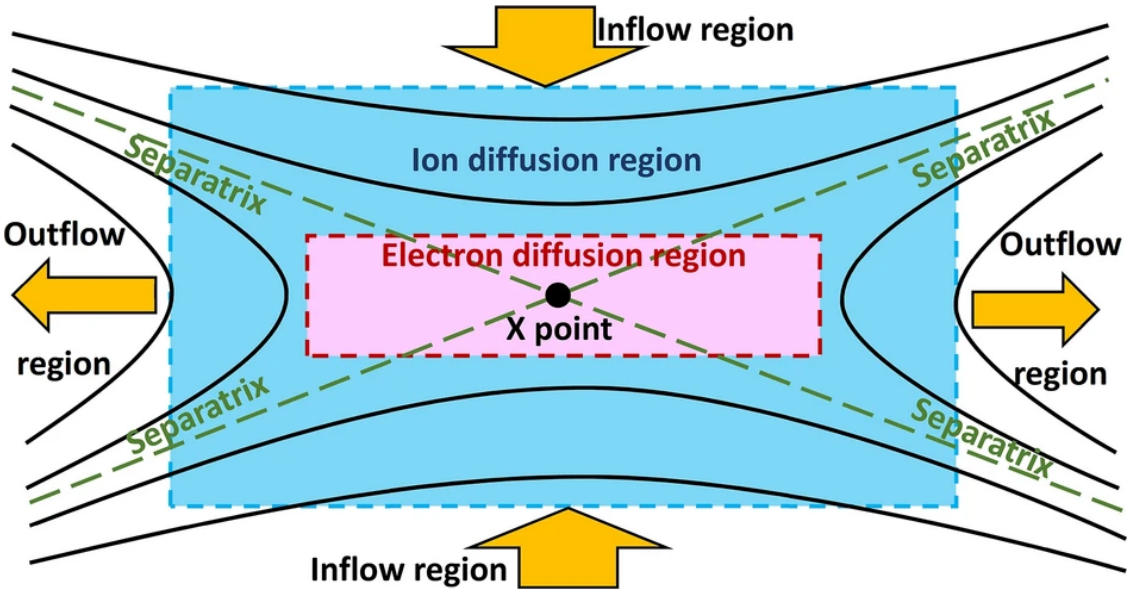


Figure 1.4: Schematic that shows different regions around a magnetic reconnection site (from Lee et al., 2020) [35].

1.4.3 Onset of Tail Reconnection

The onset of tail reconnection is a critical step in the Dungey cycle and leads to the release of stored magnetic energy in the tail. The exact mechanism that leads to the onset of tail reconnection is still an open question in space plasma physics. Reconnection has been extensively studied via modeling and has been observed not only in the planetary magnetospheres but also in the solar corona and other astrophysical systems. The onset of reconnection is difficult to study via observations because it is a transient process that occurs in a localized region in space, and usually, a spacecraft is not in the right place at the right time to capture the onset of reconnection. The majority of reconnection observations show clear signatures of ongoing reconnection, like ion/electron jets and Hall magnetic fields. On the other hand, the modeling efforts to understand reconnection onset [38, 36] have been performed in idealized setups with artificially imposed initial and boundary conditions. These idealized setups have played a critical role in understanding the physics of reconnection, but they lack the effect of the global magnetospheric dynamics and therefore may not capture the complete picture of the mechanisms that lead to the onset. In this thesis, we use a global magnetospheric model with a localized PIC region in the tail to study the onset of tail reconnection (Chapter 3). This allows us to study the onset in a self-consistent way while also capturing the effect of the global magnetospheric dynamics without artificially imposing any conditions.

1.5 Global Dynamics and the Magnetohydrodynamics (MHD) model

The interaction of the solar wind with Earth's magnetosphere is a complex plasma phenomenon. The majority of the magnetospheric plasma is Maxwellian and therefore can be well described by fluid models like Magnetohydrodynamics (MHD). MHD models have proven to be very successful in simulating the global magnetospheric dynamics, such as the bow shock stand-off distance, the magnetopause location, and the overall structure of the magnetosphere. The two most widely used MHD models for simulating the magnetosphere are ideal MHD and Hall-MHD. The generalized Ohm's law is given by:

$$\mathbf{E} = -\mathbf{u} \times \mathbf{B} + \frac{1}{n_e e}\mathbf{j} \times \mathbf{B} - \frac{1}{n_e e}\nabla p_e + \eta \mathbf{j} \tag{1.9}$$

where n_e is the electron number density, $\mathbf{j}$ is the current density, p_e is the electron pressure, and η is the resistivity. The first term is the convection term. This convection term does not allow the ions and electrons to decouple from the magnetic field. The second term is the Hall term. The ions are allowed to decouple from the magnetic field through the Hall term, while the electrons remain frozen-in. The third term is the electron pressure gradient term (also called the Biermann battery term), and the last term is the resistive term. Ideal MHD assumes that the plasma is a perfectly conducting fluid and only includes the convection term $\mathbf{E} = -\mathbf{u} \times \mathbf{B}$. This asserts that the magnetic field lines are frozen into the plasma [1], hence the plasma and magnetic field lines always move together. The ideal MHD equations are given by:

$$\frac{\partial \rho}{\partial t} + \nabla \cdot (\rho \mathbf{u}) = 0 \tag{1.10}$$

$$\frac{\partial (\rho \mathbf{u})}{\partial t} + \nabla \cdot \left(\rho \mathbf{u}\mathbf{u} + \left(p + \frac{B^2}{2\mu_0} \right) \mathbf{I} - \frac{\mathbf{B}\mathbf{B}}{\mu_0} \right) = 0 \tag{1.11}$$

$$\frac{\partial \mathbf{B}}{\partial t} + \nabla \cdot (\mathbf{u}\mathbf{B} - \mathbf{B}\mathbf{u}) = 0 \tag{1.12}$$

$$\frac{\partial e}{\partial t} + \nabla \cdot \left((e + p + \frac{B^2}{2\mu_0})\mathbf{u} - \frac{\mathbf{u} \cdot \mathbf{B}\mathbf{B}}{\mu_0} \right) = 0 \tag{1.13}$$

where ρ is the mass density, $\mathbf{u}$ is the plasma velocity, $\mathbf{B}$ is the magnetic field, B is the magnetic field magnitude, p is the plasma pressure and μ_0 is the permeability of free space. Total energy density e is given by:

$$e = e_h + \frac{B^2}{2\mu_0} \tag{1.14}$$

where e_h is the hydrodynamic energy density given by:

$$e_h = \frac{p}{\gamma - 1} + \frac{1}{2}\rho u^2 \tag{1.15}$$

γ is the adiabatic constant. In addition to the convection term, Hall-MHD also includes the Hall term as well as the Biermann battery term in Ohm's law:

$$\mathbf{E} = -\mathbf{u} \times \mathbf{B} + \frac{1}{n_e e}\mathbf{j} \times \mathbf{B} - \frac{1}{n_e e}\nabla p_e \tag{1.16}$$

The Hall MHD equations are given by:

$$\frac{\partial \rho}{\partial t} = -\nabla \cdot (\rho \mathbf{u}) \tag{1.17}$$

$$\frac{\partial (\rho \mathbf{u})}{\partial t} = -\nabla \cdot \left[\rho \mathbf{u}\mathbf{u} + (p + p_e)\,\bar{I} + \frac{B^2}{2\mu_0}\bar{I} - \frac{\mathbf{B}\mathbf{B}}{\mu_0}\right] \tag{1.18}$$

$$\frac{\partial e}{\partial t} = -\nabla \cdot \left[(e_h + p)\,\mathbf{u} + p_e \mathbf{u}_e + \mathbf{u}_e \cdot \left(\frac{\mathbf{B}^2}{\mu_0}\bar{I} - \frac{\mathbf{B}\mathbf{B}}{\mu_0}\right)\right] + p_e \nabla \cdot \mathbf{u}_e \tag{1.19}$$

$$\frac{\partial \mathbf{B}}{\partial t} = -\nabla \times \left[-\mathbf{u}_e \times \mathbf{B} - \frac{\nabla p_e}{n_e e}\right] \tag{1.20}$$

$$\frac{\partial p_e}{\partial t} = -\nabla \cdot (p_e \mathbf{u}_e) - (\gamma - 1) p_e \nabla \cdot \mathbf{u}_e \tag{1.21}$$

where $\bar{I}$ is the identity matrix, p is the ion pressure, p_e is the electron pressure.

1.6 Kinetic Effects and the Particle-In-Cell (PIC) method

Magnetohydrodynamics is a fluid model and ignores all kinetic plasma effects, such as the existence of non-Maxwellian velocity distributions and collisionless magnetic reconnection. The importance of magnetic reconnection is discussed in section 1.4.2. Understanding and modeling magnetic reconnection is extremely important for predicting space weather and understanding the global magnetospheric picture.

While MHD models cannot capture true kinetic effects, other methods like Vlasov solvers and the Particle-In-Cell (PIC) method do solve the kinetic equations and can be used to model magnetic reconnection. Vlasov solvers solve the Maxwell-Vlasov equations directly on a grid in 6D phase space. They do not suffer from statistical noise, but they are computationally extremely expensive, especially for domains as large as Earth's magnetosphere. The Particle-In-Cell (PIC) method solves Maxwell's equations of electromagnetism on an Eulerian grid while the particle motion is solved in a Lagrangian fashion. PIC methods are

much more computationally efficient than Vlasov solvers but suffer from statistical noise due to the use of a finite number of particles.

1.7 Particle-In-Cell method

Particle-in-cell methods involve tracking particles in continuous phase space in a Lagrangian frame while the moments (such as density and pressure) and fields (such as electric and magnetic fields) are computed simultaneously on Eulerian mesh points. The Vlasov equation for a species 's' can be written as:

$$\frac{\partial f_s}{\partial t} + \mathbf{v} \cdot \frac{\partial f_s}{\partial \mathbf{x}} + \frac{q_s}{m_s}(\mathbf{E} + \mathbf{v} \times \mathbf{B}) \cdot \frac{\partial f_s}{\partial \mathbf{v}} = 0 \tag{1.22}$$

The defining idea of the Particle-In-Cell (PIC) method is to split the phase space distribution function f_s into multiple distribution functions of collections of particles (called macroparticles):

$$f_s(\mathbf{x}, \mathbf{v}, t) = \sum_p f_p(\mathbf{x}, \mathbf{v}, t) \tag{1.23}$$

The functional form of f_p is chosen as:

$$f_p(\mathbf{x}, \mathbf{v}, t) = N_p S_{\mathbf{x}} \left(\mathbf{x} - \mathbf{x}_p(t)\right) S_{\mathbf{v}} \left(\mathbf{v} - \mathbf{v}_p(t)\right) \tag{1.24}$$

where N_p is the number of real particles per computational particle (macroparticle), and S_x and S_v are shape functions in space and velocity coordinates. The shape function in velocity space is chosen as:

$$S_{\mathbf{v}} \left(\mathbf{v} - \mathbf{v}_p\right) = \delta \left(v_x - v_{xp}\right) \delta \left(v_y - v_{yp}\right) \delta \left(v_z - v_{zp}\right) \tag{1.25}$$

which means that all particles inside a macroparticle move with the same velocity. The spatial shape function is chosen as:

$$S_{\mathbf{x}} \left(\mathbf{x} - \mathbf{x}_p\right) = \frac{1}{\Delta x_p \Delta y_p \Delta z_p} b_1 \left(\frac{x - x_p}{\Delta x_p}\right) b_1 \left(\frac{y - y_p}{\Delta y_p}\right) b_1 \left(\frac{z - z_p}{\Delta z_p}\right) \tag{1.26}$$

where $\Delta x_p, \Delta y_p, \Delta z_p$ are the grid resolutions in x, y and z directions respectively and b_1 is the first order spline function (Figure 2.2) which has a maximum value at $x = x_p$ and scales down linearly to zero at $x - x_p = \Delta x_p$. The same holds true for the b_1 function in the y and z directions. The Vlasov equation can be solved for each macroparticle:

$$\frac{\partial f_p}{\partial t} + \mathbf{v} \cdot \frac{\partial f_p}{\partial \mathbf{x}} + \frac{q_s}{m_s}(\mathbf{E} + \mathbf{v} \times \mathbf{B}) \cdot \frac{\partial f_p}{\partial \mathbf{v}} = 0 \tag{1.27}$$

Taking the first moment of this equation:

$$\frac{\partial \langle f_p \rangle}{\partial t} + \left\langle \mathbf{v} \cdot \frac{\partial f_p}{\partial \mathbf{x}} \right\rangle + \left\langle \frac{q_s}{m_s}(\mathbf{E} + \mathbf{v} \times \mathbf{B}) \cdot \frac{\partial f_p}{\partial \mathbf{v}} \right\rangle = 0 \tag{1.28}$$

and applying the finite condition (f_p is zero at infinity in space and velocity coordinates) results in:

$$\frac{dN_p}{dt} = 0 \tag{1.29}$$

where $\langle f_p \rangle = N_p$ represents the number of real particles per computational particle (macroparticle). This means that the number of real particles per computational particle must be conserved. Similarly, three first order spatial moments are applied to equation 1.27:

$$\frac{\partial \langle f_p \mathbf{x} \rangle}{\partial t} + \left\langle \mathbf{x}\mathbf{v} \cdot \frac{\partial f_p}{\partial \mathbf{x}} \right\rangle + \left\langle \mathbf{x}\frac{q_s}{m_s}(\mathbf{E} + \mathbf{v} \times \mathbf{B}) \cdot \frac{\partial f_p}{\partial \mathbf{v}} \right\rangle = 0 \tag{1.30}$$

Applying the finite condition results in:

$$\frac{d\mathbf{x}_p}{dt} = \mathbf{v}_p \tag{1.31}$$

Equation 1.31 only serves to relate the spatial and velocity coordinates and tells us that the velocity components are time derivatives of the spatial coordinates of macroparticles. Lastly, applying the first-order velocity moments to equation 1.27 yields:

$$\frac{\partial \langle f_p \mathbf{v} \rangle}{\partial t} + \left\langle \mathbf{v}\mathbf{v}\frac{\partial f_p}{\partial \mathbf{x}} \right\rangle + \left\langle \mathbf{v}\frac{q_s}{m_s}(\mathbf{E} + \mathbf{v} \times \mathbf{B}) \cdot \frac{\partial f_p}{\partial \mathbf{v}} \right\rangle = 0 \tag{1.32}$$

The application of the finite particle condition gives:

$$\frac{d\mathbf{v}_p}{dt} = \frac{q_s}{m_s}(\mathbf{E}_p + \mathbf{v}_p \times \mathbf{B}_p) \tag{1.33}$$

Equation 1.33 provides us with the definition of force for the macroparticles. Particle equations can be summarized as:

$$\frac{dN_p}{dt} = 0$$
$$\frac{d\mathbf{x}_p}{dt} = \mathbf{v}_p$$
$$\frac{d\mathbf{v}_p}{dt} = \frac{q_s}{m_s}\left(\mathbf{E}_p + \mathbf{v}_p \times \mathbf{B}_p\right)$$

where N_p is the number of particles in each macroparticle, $\mathbf{x}_p$ and $\mathbf{v}_p$ are spatial coordinates and velocity components of the macroparticle and $\mathbf{E}_p, \mathbf{B}_p$ represent the electric and magnetic fields at the macroparticle's spatial coordinates. $\frac{q_s}{m_s}$ is the charge to mass ratio for macroparticles of species 's'. These equations form the "Particle mover" of the PIC solver. Given a certain distribution of electric and magnetic fields, the particle location and velocity can be evolved in time. As the particles move, the electric and magnetic fields also evolve. The evolution is given by:

$$\frac{\partial \mathbf{B}}{\partial t} = -\nabla \times \mathbf{E}$$
$$\frac{\partial \mathbf{E}}{\partial t} = \frac{\nabla \times \mathbf{B}}{\mu_0 \epsilon_0} - \frac{\mathbf{J}}{\epsilon_0}$$

The coupling between field and particles comes from the current density $\mathbf{J}$, which depends on particle locations and velocities.

1.7.1 Explicit PIC

Explicit PIC is the most widely used PIC method [59, 20, 15, 56, 21, 58, 32] and is also the simplest in terms of algorithm complexity. In explicit PIC, the particle velocities and locations are updated explicitly using the electric and magnetic fields at the current time step. The electric and magnetic fields are then updated using the current density computed from the particle locations and velocities. While explicit PIC is simple, it suffers from very stringent stability criteria. The grid resolution must be smaller than the Debye length, and the time step must be smaller than the inverse of the electron plasma frequency [57].

$$\Delta t < \frac{2}{\omega_{pe}} \tag{1.34}$$
$$\Delta x \lesssim \lambda_D \tag{1.35}$$

As discussed in section 1.3, the Debye length is much smaller than the electron iner-

tial length. The inverse of the plasma frequency is also extremely small compared to the timescales of interest. These constraints make explicit PIC prohibitively expensive for large domains like Earth's magnetosphere, as well as for systems where the global scales are much larger than the kinetic scales. Therefore, explicit PIC is not a feasible method for simulating the global magnetospheric dynamics and processes like magnetic reconnection.

1.7.2 Fully Implicit PIC

Implicit schemes are a class of numerical methods that evolve the system of equations in time based on the state of the system at the current time step as well as the state of the system at the next time step. This generates a large system of equations since particle velocities and locations are variables as well. This also means that the number of variables increases as the number of particles increases, which makes implicit PIC not only computationally expensive but also very difficult to implement. Fully implicit PIC methods [10, 54] were developed to overcome the strict stability constraints of explicit PIC methods. In implicit PIC, the particles and fields are updated simultaneously. This often involves solving a large nonlinear system of equations. This allows the implicit PIC method to use a much coarser grid and a larger time step. This removes the need to resolve smaller wavelength oscillations to maintain stability. The implicit PIC method, however, is much more complex than explicit PIC and is computationally more expensive per time step. The non-linear system of equations that needs to be solved at each time step can become very large for 3D simulations. Therefore, implicit PIC is also not a feasible method for large global magnetospheric simulations.

1.7.3 Semi-Implicit PIC

Semi-implicit PIC bridges the gap between explicit and implicit PIC methods by avoiding stability constraints while maintaining a relatively simple algorithm [8, 47, 40, 33, 34, 22, 23, 4, 9]. In semi-implicit PIC, the particle velocities and locations are updated explicitly, while the electric and magnetic fields are updated implicitly, which results in a much smaller system of linear equations to solve. This allows the semi-implicit PIC method to use a grid that is much coarser than the Debye length and a time step that is much larger than the inverse of the electron plasma frequency while keeping the non-linear implicit solve limited to only the field update. Semi-implicit PIC is therefore most suitable for large-scale simulations like Earth's magnetosphere, where the global scales are much larger than kinetic scales.

1.7.3.1 Energy Conserving Semi-Implicit PIC

While there are many different semi-implicit PIC algorithms, the one most widely used in space plasma physics is the Energy Conserving Semi-Implicit Method (ECSIM) introduced by Lapenta [33, 34]. ECSIM conserves energy exactly and is unconditionally stable. ECSIM, due to its energy-conserving nature, is not prone to unphysical numerical instabilities growing uncontrollably over time, which keeps the solution stable. The particle update equations for ECSIM are given by:

$$\mathbf{x}_p^{n+1/2} = \mathbf{x}_p^{n-1/2} + \Delta t\, \mathbf{v}_p^n \tag{1.36}$$

$$\mathbf{v}_p^{n+1} = \mathbf{v}_p^n + \frac{q_p \Delta t}{m_p}\left[\mathbf{E}^{n+\theta} + \frac{\mathbf{v}_p^n + \mathbf{v}_p^{n+1}}{2} \times \mathbf{B}^n\right] \tag{1.37}$$

where $\mathbf{x}_p$ is the particle position, $\mathbf{v}_p$ is the particle velocity, $\mathbf{E}$ and $\mathbf{B}$ are the electric and magnetic fields at the particle position. $n+\theta$ is a time level between n and $n+1$ where the electric field is evaluated. In CGS units, the electric and magnetic fields are updated using the current density computed from particle locations and velocities at time level $n+\theta$ as follows:

$$\frac{\mathbf{B}^{n+1} - \mathbf{B}^n}{\Delta t} = -c\nabla \times \mathbf{E}^{n+\theta} \tag{1.38}$$

$$\frac{\mathbf{E}^{n+1} - \mathbf{E}^n}{\Delta t} = -c\nabla \times \mathbf{B}^{n+\theta} - 4\pi\overline{\mathbf{J}} \tag{1.39}$$

where $\overline{\mathbf{J}}$ is the current density computed from particle locations and velocities at time level $n+\theta$. c is the speed of light. Lapenta proved that this method conserves energy exactly if $\theta = 1/2$. While ECSIM conserves energy exactly, it does not conserve Gauss's law. Gauss's law error can accumulate over long time integrations and lead to unphysical solutions.

1.7.3.2 Gauss's Law Satisfying Energy Conserving Semi-Implicit PIC

The Gauss's Law Satisfying Energy Conserving Semi-Implicit PIC (GL-ECSIM) was introduced by Chen et al. [14]. They added a Gauss's law correction step to the ECSIM algorithm to ensure that Gauss's law error is minimized at the end of each time step. This method is also unconditionally stable and conserves energy perfectly like ECSIM while also satisfying Gauss's law (approximately). This additional step involves solving a linear system of equations to move the particles such that the charge density computed at the cell centers satisfies Gauss's law. This step is discussed in more detail in section 2.2.10.

1.8 Multi-scale Modeling and Coupling MHD with PIC

As mentioned in section 1.3, d_g, d_i, and d_e are separated from each other by several orders of magnitude. Resolving all these scales across large domains like the entire solar system or even in relatively smaller domains like Earth's magnetosphere is a daunting task. Traditionally, this has led to the use of fluid (MHD or advanced models like Hall-MHD) to simulate the bulk of the domain while kinetic models like PIC are used only in small regions. This is very helpful if the kinetic effects are significant only in localized regions while the fluid description is sufficient everywhere else. One such model is the Magnetohydrodynamics with Embedded Particle-in-Cell (MHD-EPIC) model introduced by Daldorff et al. [16] which combines a global MHD simulation with a localized Particle-In-Cell (PIC) model to capture kinetic physics. Shou et al. [50] improved on this and introduced MHD with Adaptively Embedded PIC (MHD-AEPIC), which allows the active PIC region to be any shape and adapt to the region of interest instead of a rectangular static box used in MHD-EPIC. Full adaptation to the regions of interest is provided by the Flexible Exascale Kinetic Simulator (FLEKS) code introduced by Chen et al. [13].

Both MHD-EPIC and MHD-AEPIC use the Gauss's Law Satisfying Energy Conserving Semi-Implicit PIC (GL-ECSIM) algorithm described above. Even with a localized PIC region, the computational cost of resolving the electron-scale physics is extremely high, and hence, traditionally, MHD-AEPIC simulations only resolve ion-scale physics while electron scales are underresolved. This is because the electron skin depth (d_e) is much smaller than the ion inertial length (d_i), and resolving d_e requires a much finer grid and smaller time step.

1.9 Need for Adaptive Mesh Refinement (AMR) in Semi-Implicit PIC

The need for an adaptive mesh refinement (AMR) capability in semi-implicit PIC simulations of the magnetosphere is driven by several key factors:

- **Resolution of Electron-Scale Physics:** Many important kinetic processes, such as magnetic reconnection, involve physics at the electron scale and therefore require resolving d_e. However, fully resolving d_e across the entire magnetosphere or even in localized embedded PIC regions is computationally prohibitive. An AMR capability allows us to refine the grid only in regions where electron-scale physics is important, while keeping a coarser grid elsewhere, thus making it feasible to resolve electron scales in small regions of the PIC domain.

- **Limitations of Explicit AMR-PIC:** Explicit PIC methods require resolving the Debye length and electron plasma frequency for stability. The Debye length is typically much smaller than the electron skin depth. This makes explicit PIC methods very accurate as soon as they achieve stability. This also means that explicit AMR-PIC methods don't necessarily benefit from AMR, and their utility is limited.
- **Preservation of the Velocity Distribution Function:** Previous attempts at localized high-resolution PIC simulations with semi-implicit PIC methods include the Multi-level Multi-domain (MLMD) method [30, 31], where the PIC domain is split into multiple levels of refinement, but each level has its own set of particles. This can lead to different levels not sharing the same velocity distribution functions. The AMR-PIC method we developed in this thesis allows for a single set of particles to be shared across all levels of refinement, which ensures that the velocity distribution function is preserved across all levels of refinement.

1.10 Overview of the Thesis

This thesis is organized as follows. In Chapter 2, I describe the development of a semi-implicit PIC method with adaptive mesh refinement (AMR) based on the Gauss's Law Satisfying Energy Conserving Semi-Implicit PIC (GL-ECSIM) algorithm. This AMR-PIC method is tested with a variety of numerical tests to verify its accuracy and stability. In Chapter 3, I use the MHD-AEPIC model to study the onset of tail reconnection in Earth's magnetotail. In Chapter 4, I use the AMR-PIC method developed in Chapter 2 to study and reproduce the results similar to the uniform grid simulations in Chapter 3. Chapter 5 concludes the thesis and discusses future work.

CHAPTER 2

Adaptive Mesh Refinement in Semi-Implicit Particle-in-Cell Method

2.1 Introduction

Plasma physics in space and the laboratory often involves processes that span a large range of spatial and temporal scales, ranging from the electron scale to the global scale. Resolving all these scales across large domains like the entire solar system or even in relatively smaller domains like Earth's magnetosphere is daunting. This challenging problem has led to the use of coupled models, i.e., using magnetohydrodynamic (ideal MHD or Hall MHD) models to simulate the bulk of the domain, while kinetic models, for example, Particle-in-Cell (PIC) codes, are used only in small regions. This is very helpful if the kinetic effects are significant only in localized regions while the MHD description is sufficient everywhere else. One such model is the Magnetohydrodynamics with Embedded Particle-in-Cell (MHD-EPIC) model introduced by Daldorff+ [16], which combines a global MHD simulation with a localized particle-in-cell (PIC) model to capture kinetic physics. Shou+ [50] improved on this and introduced MHD with Adaptively Embedded PIC (MHD-AEPIC), which allows the active PIC region to be any shape and adapt to the region of interest instead of a rectangular static box used in MHD-EPIC. Full adaptation to the regions of interest is provided by the Flexible Exa-scale Kinetic Simulator (FLEKS) code [13], which is implemented based on the AMReX library [62].

A further step in improving computational efficiency is to introduce an adaptive grid for the PIC model. Explicit PIC is the most commonly used particle-in-cell method, but it has very stringent spatial and temporal stability criteria, requiring the resolution of the Debye length and the electron plasma frequency. Although there are several examples of explicit AMR PIC methods [59, 20, 15, 56, 21, 58, 32], the achievable speed-up is somewhat restricted by the stability criteria.

[1]This chapter was published in *Computer Physics Communications* in 2025 [2]

The semi-implicit particle-in-cell method [8, 47, 40, 33, 34, 22, 23, 4, 9] has much more relaxed stability restrictions. The spatial resolution is only limited by accuracy considerations, while the time step is limited by the CFL condition based on the particle velocities. With the MHD-AEPIC model, we can apply the PIC code to localized regions where kinetic physics is important. However, due to the large separation between the ion and electron scales, it is still computationally expensive to fully resolve the electron-scale physics. The development of the semi-implicit PIC with AMR aims to efficiently capture localized electron-scale processes, such as resolving the electron diffusion region in a magnetic reconnection simulation. Innocenti+ [31, 30] developed a multi-level multi-domain (MLMD) method for semi-implicit PIC. MLMD differs from AMR because each level of refinement has its own set of particles and hence the complete velocity distribution function is not shared by different refinement levels. A hybrid particle-in-cell method with AMR based on the MLMD approach has recently been developed [3].

Our PIC solver is based on the Gauss's Law satisfying Energy Conserving Semi-Implicit Method (GL-ECSIM) [14], which has superior accuracy and stability compared to the semi-implicit PIC method employed in MLMD [31]. The AMR method developed here has a single set of particles shared by all levels and hence the velocity distribution function is shared among all refinement levels. We maintain the number of particles per cell within prescribed bounds by employing particle splitting and merging [13, 12]. The electromagnetic field solution obtained on the fine level is used to overwrite the fields on the underlying coarser levels without any interpolation between fine and coarse field solutions, which is different from the MLMD approach.

We describe the new algorithm in section 2.2. Numerical tests and their results are discussed in section 2.3, while section 2.4 describes theoretical speed-up expectations and comparison with actual speed-up. We conclude with section 2.5.

2.2 AMR semi-implicit particle in cell method

The semi-implicit particle-in-cell algorithm with adaptive mesh refinement developed here is based on the Gauss's Law satisfying Energy-Conserving Semi-Implicit Particle-in-Cell method (GL-ECSIM) [14], which itself is based on the Energy Conserving Semi-Implicit method (ECSIM) [33, 34] with an additional Gauss's law enforcing step.

GL-ECSIM uses a staggered grid, where the electric field is defined at cell nodes and the magnetic field is defined at cell centers. The basic equation used in GL-ECSIM to update

the electric field is:

$$\mathbf{E}^{n+\theta} + \delta^2 \left[\nabla\left(\nabla \cdot \mathbf{E}^{n+\theta}\right) - \nabla^2 \mathbf{E}^{n+\theta}\right] = \mathbf{E}^n + \delta\left(\nabla \times \mathbf{B}^n - \frac{4\pi}{c}\overline{\mathbf{J}}\right) \tag{2.1}$$

where $\delta = c\theta\Delta t$, c is the speed of light, and Δt is the time-step. $\overline{\mathbf{J}}$ is the predicted node current at $n+1/2$ time stage and it depends on $\mathbf{E}^{n+\theta}$, which is an intermediate electric field state between $\mathbf{E}^n$ and $\mathbf{E}^{n+1}$:

$$\mathbf{E}^{n+\theta} = (1-\theta)\mathbf{E}^n + \theta\mathbf{E}^{n+1} \tag{2.2}$$

The energy conservation can be satisfied exactly if $\theta = 1/2$ as shown in [33], but in practice slightly larger values (e.g. $\theta = 0.51$) provide more stable numerical solutions [14]. The current density $\overline{\mathbf{J}}$ at grid node g is defined as

$$\overline{\mathbf{J}}_g = \sum_s \left[\widehat{\mathbf{J}}_{s,g} + \frac{\beta_s}{V_L}\sum_{g'} \mathbf{M}_{s,gg'} \cdot \mathbf{E}_{g'}^{n+\theta}\right] \tag{2.3}$$

where s indexes the different species (for example electrons and protons), $\beta_s = (\Delta t/2)(q_s/m_s)$, and q_s/m_s is the charge per mass of species s. $\widehat{\mathbf{J}}_{s,g}$ is the node current calculated by rotating the velocities of particles by the magnetic field [33]. V_L is the cell volume at grid level L. $\mathbf{M}_{s,gg'}$ is called the mass matrix and relates the change of the current density $\overline{\mathbf{J}}_g$ at node g at time level $n+1/2$ to the particle acceleration due to the electric field $\mathbf{E}_{g'}^{n+\theta}$ at neighboring nodes g'. It is important to note that nodes g' also contain node g itself. $\widehat{\mathbf{J}}_{s,g}$ is defined as:

$$\widehat{\mathbf{J}}_{s,g} = \sum_{p \in P_s} q_p \boldsymbol{\alpha}_p \mathbf{v}_p W_{pg} \tag{2.4}$$

while $\mathbf{M}_{s,gg'}$ is defined as:

$$\mathbf{M}_{s,gg'} = \sum_{p \in P_s} q_p \boldsymbol{\alpha}_p W_{pg'} W_{pg} \tag{2.5}$$

Set P_s contains all particles of species s, q_p is the charge of the particle that depends on the particle's weight, $\mathbf{v}_p$ is the velocity of the particle and $W_{pg} = W(\mathbf{x}_p^{n+1/2} - \mathbf{x}_g)$ represents the interpolation function between node g and particle p (see section 2.2.3). The effect of the magnetic field on the velocity of particle p is given by the rotation matrix:

$$\boldsymbol{\alpha}_p = \frac{\mathbf{I} - \beta_s \mathbf{I} \times \mathbf{B}_p^n + \beta_s^2 \mathbf{B}_p^n \mathbf{B}_p^n}{1 + \left(\beta_s B_p^n\right)^2} \tag{2.6}$$

where $\mathbf{I}$ is the identity matrix and $\mathbf{B}_p^n$ is the magnetic field vector interpolated at the location

of particle p.

The spatial discretization of eq. (2.1) can be found in [14]. In particular, the $\nabla \cdot \mathbf{E}^{n+1/2}$ term is implemented as a linear combination of the most compact discretization and an extended stencil discretization. This linear interpolation coefficient can be represented by γ such that $\gamma = 0$ uses the compact stencil only, while $\gamma = 1$ uses the extended stencil only. Perfect energy conservation in GL-ECSIM is achieved with $\gamma = 0$, but a small value of γ (e.g. $\gamma = 0.1$) is needed to reduce spurious oscillations in the solution [14]. When $\gamma > 0$, the extended stencil needs two layers of ghost cells around the refined regions. For a refinement ratio of 2 or more, this is fully covered by a single layer of coarse cells surrounding the fine grid, which is sufficient for the simple second-order (bi/tri)linear interpolation.

2.2.1 Grid Structure

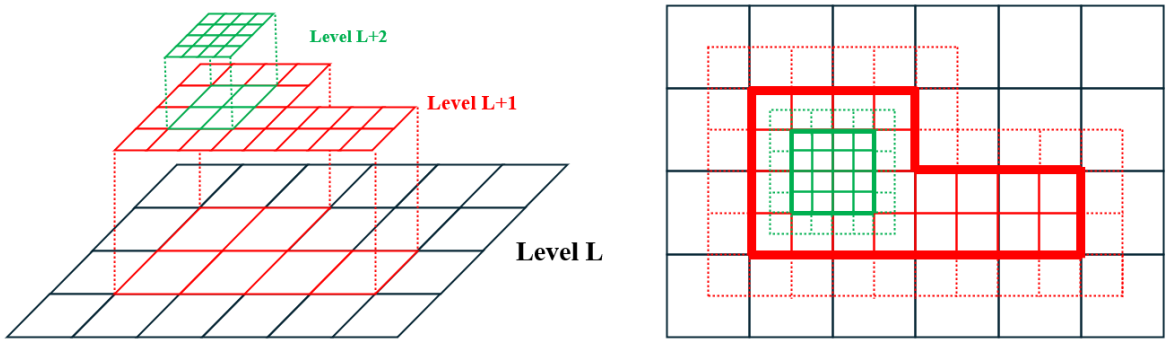


Figure 2.1: Schematics of the AMR grid structure. Left: Three refinement levels are shown in black, red and green. Right: Refinement levels with surrounding ghost cells shown by dotted lines.

The base grid, referred to as level $L = 0$, fills the full computational domain. The refined grid level $L+1$ always overlays the grid level L, including one (or two) layers of ghost nodes surrounding the level $L+1$ grid. The nodes of the grids are aligned so that every node level L has a collocated node at level $L+1$. The refined levels $L > 0$ can consist of multiple disconnected regions. Figure 2.1 illustrates an AMR grid with the base grid at level 0 and refinements at levels 1 and 2.

2.2.2 Refinement Initialization

A refined region can be initialized based on any refinement criteria of choice. If a cell satisfies some refinement criteria, R^D cells are generated in the finer level with $1/R$ the size as the parent coarse cell. D is the number of spatial dimensions and R is the refinement ratio. In general, R can be any integer larger than 1 but we typically use powers of 2, such as 2, 4, or 8. The cell size at grid level L is given by

$$\Delta x_L = R^{-L} \Delta x_0 \tag{2.7}$$

where Δx_0 is the grid resolution at the base level.

The node-centered electric and cell-centered magnetic fields are then interpolated from the coarse grid using simple bilinear or trilinear interpolation. We have also implemented using third- and fourth-order interpolation formulas, which seem to have insignificant effects, but require a larger stencil, which means that we need to surround the refined region with at least two layers of coarse cells.

2.2.3 Particles

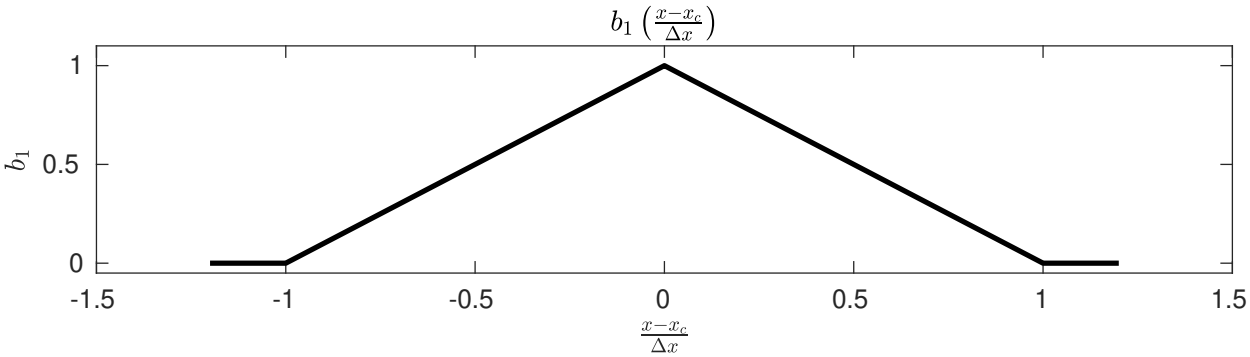


Figure 2.2: The interpolation function W^L used to interpolate between grid level L and particles is based on the b_1 spline function.

Particle properties in GL-ECSIM are staggered in time. Particle velocities are stored at integer time stages, while particle locations are stored at half-integer time stages. Particles are assigned to the highest grid level available at the particle's location. As the particles move, they may get assigned to a different grid level based on the new location. This is contrary to the Multi-Level Multi-Domain (MLMD) method [31], which has separate sets of particles at each grid level. This means that our method, unlike MLMD, propagates the

complete velocity distribution information between grid levels. The interpolation function for grid level L is

$$W^L\left(\mathbf{x}_p - \mathbf{x}_c\right) = b_1\left(\frac{x_p - x_c}{\Delta x_L}\right) b_1\left(\frac{y_p - y_c}{\Delta y_L}\right) b_1\left(\frac{z_p - z_c}{\Delta z_L}\right) \tag{2.8}$$

where b_1 represents b-spline of order one as shown in Figure 2.2. $\mathbf{x}_p$ is the location of the particle and $\mathbf{x}_c$ can be the location of any node or cell center that we are interpolating to/from. Δx_L, Δy_L and Δz_L represent the cell size in three respective dimensions. We use $\Delta x_L = \Delta y_L = \Delta z_L$ for all the simulations presented here, but this is not a strict requirement.

2.2.4 Updating Electric Field

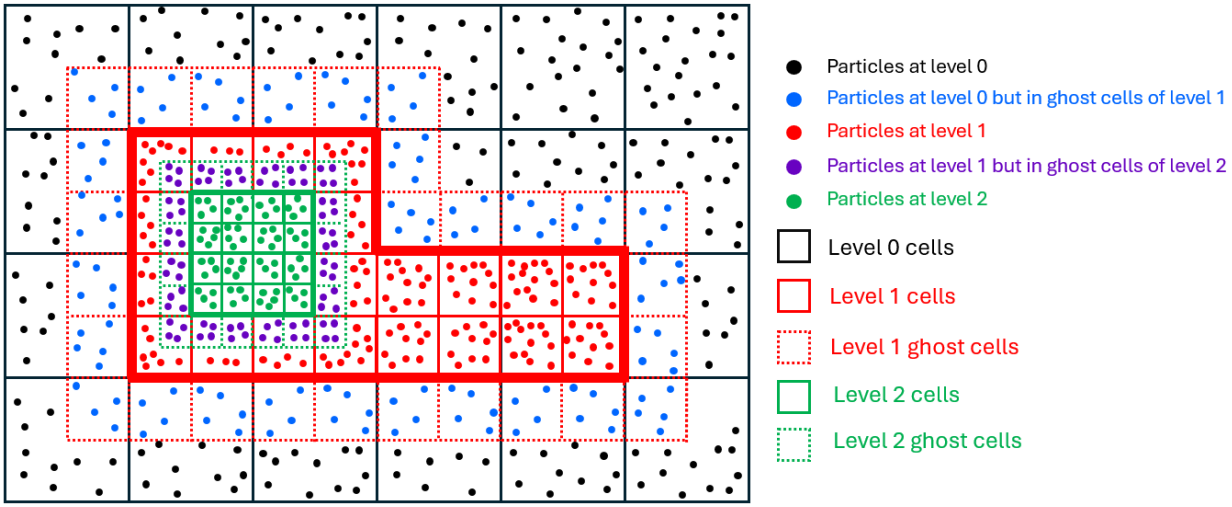


Figure 2.3: Particles belonging to three different refinement levels are shown in black, blue, red, purple and green. The ghost cells of the grid levels are indicated by dotted lines. Black particles belong to level 0, blue particles belong to level 0 but are inside the ghost cells of level 1, red particles belong to level 1, purple particles belong to level 1 but are inside the ghost cells of level 2 and green particles belong to level 2.

To update the electric field in GL-ECSIM, the current $\widehat{\mathbf{J}}^L_{s,g}$ and the mass matrix $M^L_{s,gg'}$ need to be calculated at each level L. Each particle at level L contributes to $\widehat{\mathbf{J}}^{L'}_{s,g}$ and $M^{L'}_{s,gg'}$ at all levels $L' \leq L$. Particles at level L that are in the ghost cells of level $L+1$ also contribute to level $L+1$. In Figure 2.3 all particles are used to calculate $\widehat{\mathbf{J}}^0_{s,g}$ and $M^0_{s,gg'}$ at level 0. The blue, red, purple and green particles contribute to level 1, while only the purple and green particles contribute to level 2. It is important to note here that $\widehat{\mathbf{J}}^L_{s,g}$ and $M^L_{s,gg'}$ are calculated using

the interpolation function W^L, regardless of the level to which the contributing particles belong. Once $\widehat{\mathbf{J}}^L_{s,g}$ and $M^L_{s,gg'}$ are calculated for each level, the electric field of the coarsest level is updated with the implicit solver to obtain both $\mathbf{E}^{0,n+\theta}$ and $\mathbf{E}^{0,n+1}$ at the coarsest level. The value of $\mathbf{E}^{0,n+\theta}$ at the coarsest level is interpolated to the ghost nodes of level 1 and used as a boundary condition for calculating both $\mathbf{E}^{1,n+\theta}$ and $\mathbf{E}^{1,n+1}$ with the implicit solver at level 1. This serves as a boundary condition for any subsequent refinement levels, and the procedure is continued until the electric field is updated at all grid levels.

2.2.5 Moving Particles

Once updated electric fields are obtained, particles at each refinement level are moved according to the ECSIM algorithm [33] using $\mathbf{E}^{L,n+\theta}$ and $\mathbf{B}^{L,n}$ on that level:

$$\begin{aligned} \mathbf{x}_p^{n+1/2} &= \mathbf{x}_p^{n-1/2} + \Delta t \mathbf{v}_p^n \\ \mathbf{v}_p^{n+1} &= \mathbf{v}_p^n + \Delta t \frac{q_p}{m_p} \left(\mathbf{E}^{L,n+\theta}(\mathbf{x}_p^{n+1/2}) + \overline{\mathbf{v}}_p \times \mathbf{B}^{L,n}(\mathbf{x}_p^{n+1/2}) \right) \end{aligned} \tag{2.9}$$

If a particle crosses a refinement level boundary, it is moved over to the new refinement level. While the AMR ECSIM is no longer exactly energy-conserving, our numerical tests show it still maintains the stability and accuracy properties of ECSIM on uniform grids.

2.2.6 Updating Magnetic Field

The magnetic field on all levels can then be updated to $\mathbf{B}^{L,n+1}$ from the discrete form of the induction equation:

$$\frac{\mathbf{B}^{L,n+1} - \mathbf{B}^{L,n}}{\Delta t} = -c \nabla \times \mathbf{E}^{L,n+\theta} \tag{2.10}$$

where $\mathbf{B}_c$ at the cell centers is obtained from a compact second-order centered discretization of the curl operator for the node centered electric field $\mathbf{E}_g$.

2.2.7 Synchronizing Fields

The magnetic field is simply averaged down from the finer cell centers to the coarser cell centers. Assume that the coarse node $[i', j', k']$ is covered by the fine node $[i, j, k]$. Either we can directly overwrite the electric field at the coarse node with the electric field at the fine node as:

$$\mathbf{E}^L_{i',j',k'} = \mathbf{E}^{L+1}_{i,j,k} \tag{2.11}$$

or we can average the electric field at the fine level to the coarse level as:

$$\mathbf{E}^{L}_{i',j',k'} = \frac{1}{12}\left(\sum_{x=\pm1}\mathbf{E}^{L+1}_{i+x,j,k} + \sum_{y=\pm1}\mathbf{E}^{L+1}_{i,j+y,k} + \sum_{z=\pm1}\mathbf{E}^{L+1}_{i,j,k+z}\right) + \frac{1}{2}\mathbf{E}^{L+1}_{i,j,k} \tag{2.12}$$

In 2D, this reduces to:

$$\mathbf{E}^{L}_{i',j'} = \frac{1}{8}\left(\sum_{x=\pm1}\mathbf{E}^{L+1}_{i+x,j} + \sum_{y=\pm1}\mathbf{E}^{L+1}_{i,j+y}\right) + \frac{1}{2}\mathbf{E}^{L+1}_{i,j} \tag{2.13}$$

In our testing, we found that both methods produce similar results, but the electric field at the coarse level overwritten with the averaging method has similar noise as the rest of the electric field at the coarse level, while the electric field overwritten directly is more noisy and it may impact the implicit electric field solver on the coarse level. Hence, we use the averaging method.

2.2.8 Particle Merging and Splitting

We try to maintain a near-constant particles-per-cell (PPC) number across all refinement levels. Since the finer levels have smaller Δx, the particles-per-volume number is higher in higher levels. This also helps better resolve kinetic physics at higher levels. To maintain near-constant PPC, we split/merge particles. Particles in cells with less PPC are split from one to two as described in [13]. Particles in cells with higher PPC are merged from ten to eight particles while conserving mass, momentum and energy as well as minimizing the change in phase space distribution as described in [12]. In addition to merging and splitting based on PPC, we also split particles if they get heavier than a threshold. First, we sum the mass of all the particles of a species in a cell and divide the total mass by the target PPC number of that cell to get the ideal particle weight. Any particle larger than twice this value is split irrespective of the PPC number of the cell.

2.2.9 Pre-splitting

Particles in the vicinity of a refinement level are split such that the particle-per-volume (PPV) number in these cells matches the PPV number of the higher refinement level. We call this pre-splitting. This is achieved simply by setting a higher target PPC number for these cells. If particles are not pre-split, the velocity distribution function in the refined region deviates slightly from high-resolution uniform grid solutions. In our testing, pre-splitting in two cells around a refinement level seems to be sufficient to achieve the desired accuracy.

2.2.10 Gauss's Law Correction

As discussed in [14], the original ECSIM method introduces small errors in Gauss's law that accumulate over time and can lead to unphysical solutions for longer time integration. GL-ECSIM corrects this by introducing a slight displacement to particle positions such that Gauss's law error is removed or minimized. This method involves solving the following linear system of equations:

$$\sum_{c'} M_{cc'}\lambda_{c'} = S_c \tag{2.14}$$

for the Lagrange multipliers $\lambda_{c'}$ defined at cell center c'. Here S_c is the error in Gauss's law at cell center c and $M_{cc'}$ is a mass matrix describing the interaction of neighboring grid cells through the displacement of particles (see [14] for details).

$$M_{cc'} = \sum_p |q_p| \nabla W\left(\mathbf{x}_p^{n+\frac{1}{2}} - \mathbf{x}_c\right) \cdot \nabla W\left(\mathbf{x}_p^{n+\frac{1}{2}} - \mathbf{x}_{c'}\right) \tag{2.15}$$

where q_p is the charge of particle p and ∇W is the gradient of the interpolation function. The error in Gauss's law is discretized as:

$$S_c = \frac{1}{4\pi}\nabla \cdot \mathbf{E}^n - \left[\gamma q_c^{n+\frac{1}{2}} + (1-\gamma) q_c^{n-\frac{1}{2}}\right] \tag{2.16}$$

Since particle locations exist at half-integer time stage, the cell-centered net electric charge q_c^n at time level n is interpolated from $q_c^{n-\frac{1}{2}}$ and:

$$q_c^{n+\frac{1}{2}} = \sum_p q_p W(\mathbf{x}_p^{n+\frac{1}{2}} - \mathbf{x}_c) \tag{2.17}$$

where $\mathbf{x}_c$ is the coordinate of cell center c. Using $\gamma = 1/2$ results in perfect time centering, but $\gamma = 0.51$ gives a better solution [14].

This method was designed for uniform PIC grids and it needs some extension to perfectly correct Gauss's law error for an AMR grid. Unlike the electric field solver that solves levels from bottom (level 0) to top, the Gauss's law error is corrected from top to bottom, i.e. we start with the finest level (assume L) and solve

$$\sum_{c'} M^L_{cc'}\lambda^L_{c'} = S^L_c \tag{2.18}$$

All particles at the finest level L as well as particles at level $L-1$ that are located in the ghost cells of level L are used to calculate the net charge q_c that contributes to the error S_c^L at the cell centers c at level L. Charge calculation is performed using the shape function

associated with level L. While calculating $M^L_{cc'}$ for the finest level, the particles in the ghost cells are ignored and only the particles actually located at level L are used. This forces the solver to generate a solution that eliminates/reduces Gauss's law error without moving the particles in the ghost cells of level L. After the solution is obtained, the particle positions at time level $n + 1/2$ and grid level L are updated as:

$$\mathbf{x}_p^{\prime L} = \mathbf{x}_p^L + \Delta\mathbf{x}_p^L \tag{2.19}$$

where $\Delta\mathbf{x}_p^L$ is a function of λ_c^L. We apply a limiter to ensure that the displacement does not exceed some fraction of the cell size at level L, in particular, we limit $|\Delta x_p^L| \leq \Delta x_L/10$.

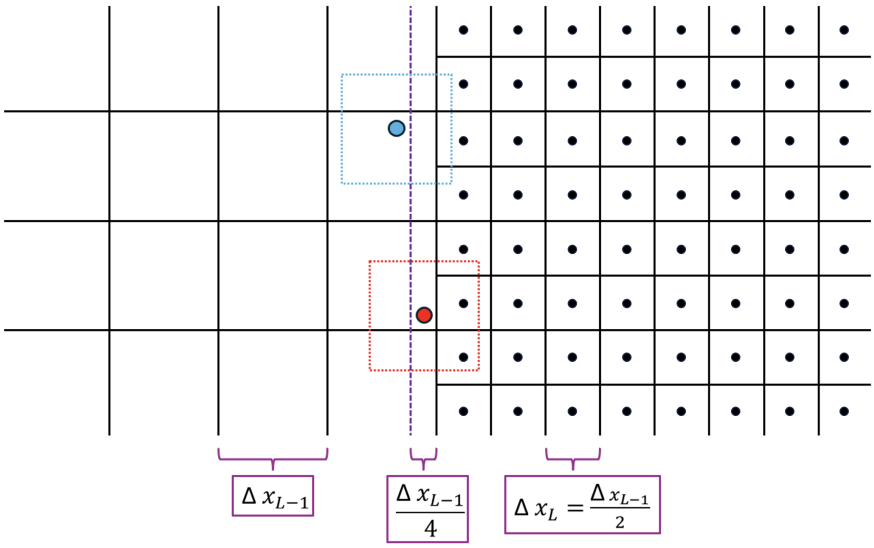


Figure 2.4: Gauss's Law enforcement at a grid resolution change. The extent of the fine interpolation function W^L is shown by the blue dotted square around the blue particle on the left side of the dashed purple line. It does not reach any fine cell centers (black dots), so this particle can be moved without changing the net charge in the fine grid. The fine interpolation function (red dotted square) of the red particle on the right of the dashed purple line does reach the fine cell centers, therefore these particles are not moved when the Gauss Law error is eliminated on the coarse grid.

For level $L-1$, we have to calculate the net charge at cell centers using the particles at both levels $L-1$ and L and also level $L-2$ particles in the ghost cells of level $L-1$. Note that the new locations $\mathbf{x}_p^{\prime L}$ are used for the level L particles. All particles are taken into account with the level $L-1$ shape function. This charge is then used to calculate S_c^{L-1}, but we set $S_c^{L-1} = 0$ at all cells c that are covered by level L. This forces the solver to generate a solution that does not attempt to minimize the error in the cells covered by level L. Only

particles at level $L-1$ are used to calculate $M_{cc'}^{L-1}$, but particles that can influence charge calculation at level L are excluded. This forces the solver to generate a solution without moving particles that can reintroduce Gauss's law error at level L. With a refinement ratio of 2, this exclusion applies to particles that are at a distance $\leq \Delta x_{L-1}/4$ from any level L cell because the interpolation function W^L with respect to level L of any particle within this distance is non-zero at least one level L cell center as depicted in Figure 2.4. Similar to S_c^{L-1}, at all cells c that are covered by level L we set $M_{cc'}^{L-1} = 0$.

The same procedure is repeated for all levels $L-2$ to 0. The particles that move across grid resolution changes are assigned to the appropriate grid level. Similarly to the original uniform-grid algorithm, the whole cycle from level L to 0 is repeated three times to reduce the Gauss's law errors to a negligible magnitude in the full domain.

2.2.11 Dynamic AMR

Dynamic AMR refers to changing refinement levels during a simulation. To remove a refinement level from a particular spatial location, we simply delete the fine grid from that location and assign particles to the coarser level. Since fields had already been synced to the underlying coarser grid, no syncing is required at this stage.

If a refinement level is added, we interpolate the electric and magnetic fields to the new level from the coarser level. The particles covered by the new fine level are assigned to it. The underlying coarse grids may need to be enlarged to ensure that each fine grid is surrounded by at least one layer of coarse cells. For coarsening and refinement, particle splitting and merging performed during the time steps adjust the number of particles per cell. We note that in our implementation the grid adaptation is performed after the Gauss's law cleaning step, so there could be a non-negligible Gauss's law error in the newly created grid cells, but this error is quickly removed by the Gauss's law correction in the next time step.

2.2.12 Time step

In our current implementation, all grid cells take the same time step Δt, i.e., there is no subcycling. This choice simplifies the algorithm substantially, but it also means that the cells on the finest level effectively determine the time step. Following [11], we calculate the root-mean-square of the particle velocities:

$$V_{s,g}^2 = \frac{1}{N_{s,g}} \sum_{p \in P_{s,g}} v_p^2 \tag{2.20}$$

where $N_{s,g}$ and $P_{s,g}$ are the number and set of particles of species s (electrons or ions) in grid cell g, respectively. The time step is then set as

$$\Delta t = C \min_{s,g} \frac{\Delta x_g}{V_{s,g}} \tag{2.21}$$

where the minimum is taken for all species s and all grid cells g. The cell size Δx_g varies with the grid level L. For non-cubic cells, Δx_g should be replaced with $\min(\Delta x_g, \Delta y_g, \Delta z_g)$. The coefficient $C < 1$ is, in effect, the CFL number with respect to the typical particle speed. A usual setting is $C = 0.4$.

2.3 Numerical tests

We perform a series of tests in two spatial dimensions on double-periodic domains. The electromagnetic field and the particle velocities have three components. We choose to do 2D tests for the sake of clarity and easier reproducibility. The AMR PIC algorithm is implemented for both 2 and 3 spatial dimensions. In all tests, the grid cells are squares with $\Delta x = \Delta y$. The charges of protons and electrons are $+1$ and -1, respectively, in all tests involving particles. The ion mass is 1. The time step is set by eq. (2.21) using $C = 0.4$ in all tests involving particles. The speed of light is $c = 1$ in normalized (CGS) units.

2.3.1 Light wave test

The test involves a light wave propagating at an angle relative to the 2D grid without any particles. This test checks the accuracy of the field solver on an AMR grid. The analytic solution is:

$$\begin{aligned}
E_x(x,y,t) &= -0.8 \sin\left(k(0.6x + 0.8y - ct)\right) && (2.22)\\
E_y(x,y,t) &= +0.6 \sin\left(k(0.6x + 0.8y - ct)\right) && (2.23)\\
E_z(x,y,t) &= -1.0 \cos\left(k(0.6x + 0.8y - ct)\right) && (2.24)\\
B_x(x,y,t) &= -0.8 \cos\left(k(0.6x + 0.8y - ct)\right) && (2.25)\\
B_y(x,y,t) &= +0.6 \cos\left(k(0.6x + 0.8y - ct)\right) && (2.26)\\
B_z(x,y,t) &= +1.0 \sin\left(k(0.6x + 0.8y - ct)\right) && (2.27)
\end{aligned}$$

where $k = 2\pi/48$ is the wave number, and the initial condition is obtained by setting $t = 0$. The periodic simulation domain is $-40 < x < 40$ and $-30 < y < 30$. The grid resolution of the base grid is $\Delta x_0 = 1$. The grid is refined at $-20 < x < 20$ and $-15 < y < 15$ to

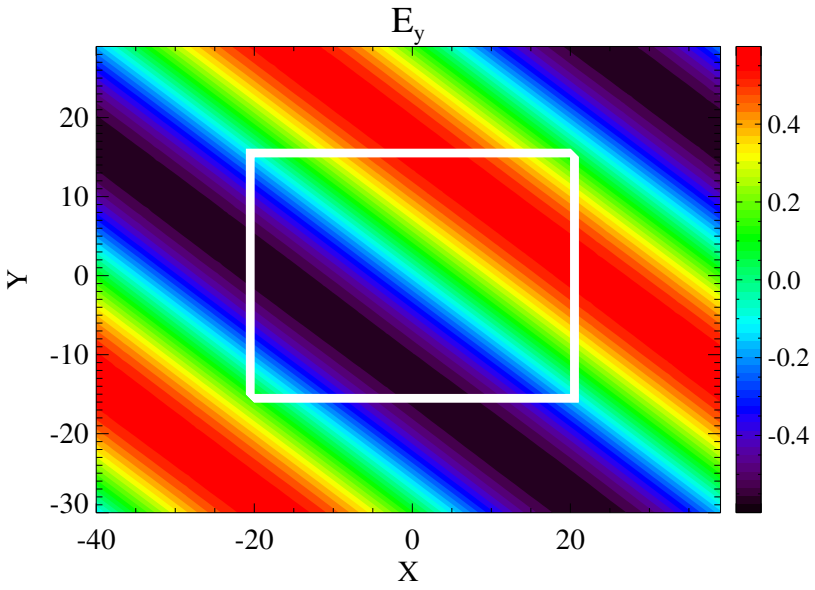


Figure 2.5: Light wave test solution at $t = 384$. The E_y component of the electric field is shown. The base grid resolution is $\Delta x_0 = 1$. The white rectangle surrounds the refined region with $\Delta x_1 = 1/2$.

$\Delta x_1 = 1/2$. The time step is $\Delta t = 0.4$ so that the light wave moves less than one grid cell per time step even in the refined region. Figure 2.5 shows the E_y field component at $t = 384$ after the light wave traveled for 8 wave periods ($T = \lambda/c = 48$). The integrity and amplitude of the light wave are well-preserved.

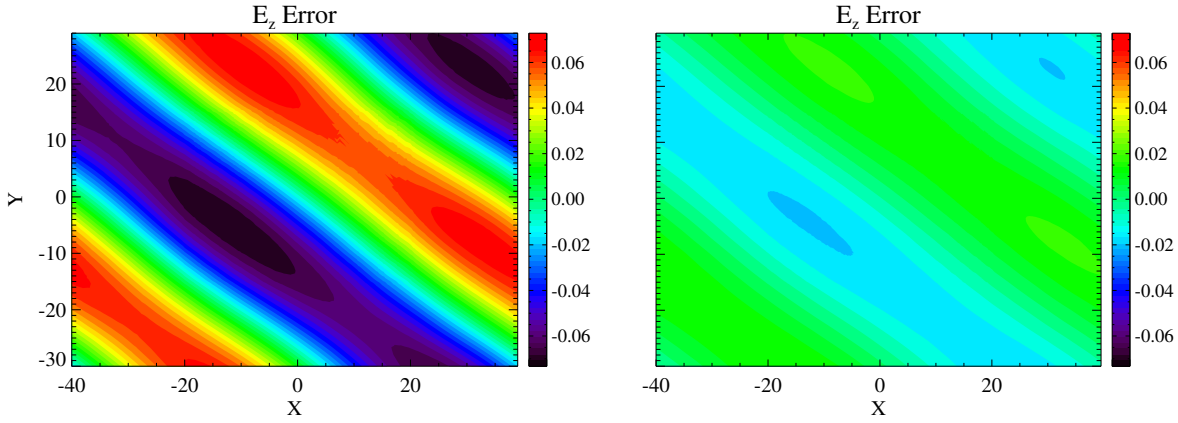


Figure 2.6: Light wave test. E_z error at $t = 384$. Left: Base grid resolution $\Delta x_0 = 1$. Right: Base grid resolution $\Delta x_0 = 1/2$.

We perform a grid convergence study to check the order of accuracy of the field solver. Figure 2.6 shows the error in E_z relative to the analytic solution (2.24) at the end of the simulation. The figure on the left has a base grid resolution $\Delta x_0 = 1$ and a refined resolution $\Delta x_1 = 1/2$, while the figure on the right has $\Delta x_0 = 1/2$ and $\Delta x_1 = 1/4$. The corresponding average errors in the L_1 norm are 0.0431 and 0.0108, which shows second-order convergence. All electric and magnetic field component errors have similar magnitudes and convergence rates. Note that the errors are not smaller in the refined region because the wave has already propagated through the domain several times and the errors are dominated by the contribution from the coarse grid. At the very beginning of the simulation, the errors are 4 times smaller inside the refined region than outside as expected.

2.3.2 Fast wave test

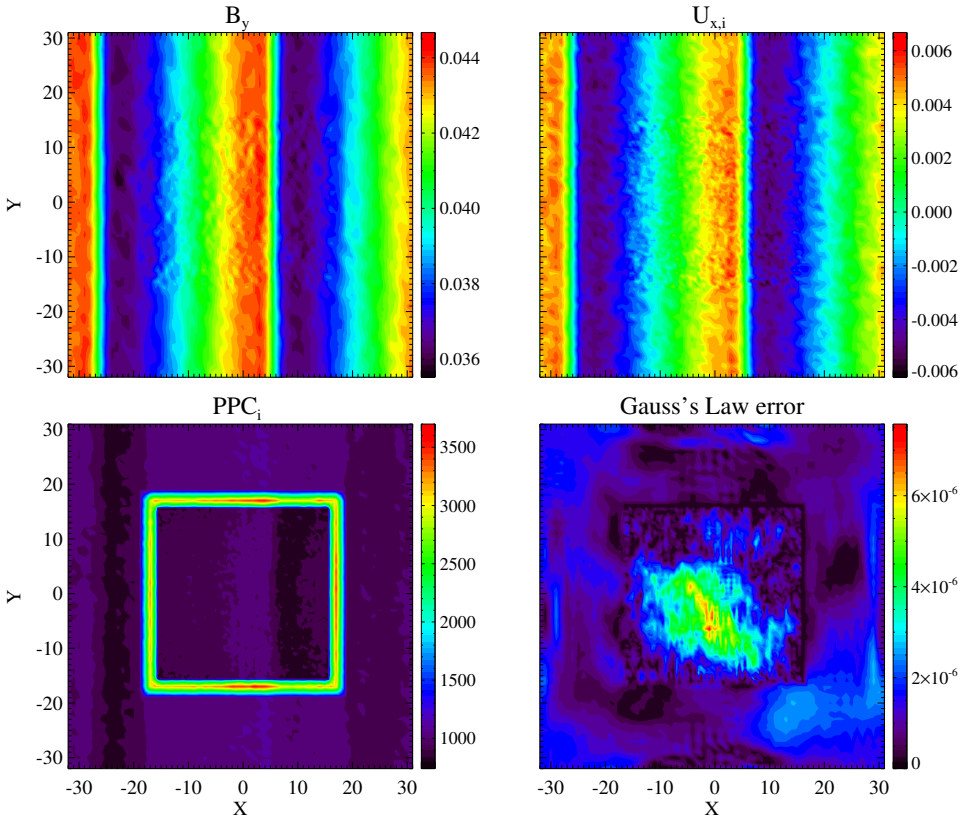


Figure 2.7: Fast wave test solution at $t = 600$. Top left: Magnetic field B_y. Top right: X component of the ion velocity $U_{x,i}$. Bottom left: Number of ion particles per cell PPC_i. Bottom right: Magnitude of Gauss's Law error $|\nabla \cdot \mathbf{E} - 4\pi q_c|$.

We test the accuracy of the AMR PIC algorithm by modeling the propagation of a fast magnetosonic wave on an AMR grid. The initial condition is the same as described in [16] except for leaving the wave aligned with the X axis. The linearized analytic solution of the fast wave is:

$$\rho = \rho_0[1 + \delta \sin(kx - \omega t)] \tag{2.28}$$
$$u_x = c_f \delta \sin(kx - \omega t) \tag{2.29}$$
$$p = p_0[1 + \gamma\delta \sin(kx - \omega t)] \tag{2.30}$$
$$p_{\parallel} = p_0[1 + \delta \sin(kx - \omega t)] \tag{2.31}$$
$$B_y = B_0[1 + \delta \sin(kx - \omega t)] \tag{2.32}$$

where the wave amplitude is $\delta = 0.1$, the background has $\rho_0 = 1$, $p_0 = 1$, $B_0 = 0.04$, $B_x = B_z = 0$ and $u_y = u_z = 0$. The fast magnetosonic speed $c_f = \sqrt{\frac{B_0^2 + 2p_0}{\rho_0}} = 0.05$. The wavelength is set to $\lambda = 32$, which makes the wave number $k = 2\pi/32$. The simulation domain is $-32 < x, y < 32$ with $\Delta x_0 = 1$ and periodic in both directions. There is a refinement at $-16 < x, y < 16$ with $\Delta x_1 = 1/2$. The speed of light $c = 1$ is much larger than $c_f = 0.05$. The pressure is split equally between electrons and ions [16]. The ion-to-electron mass ratio is $m_i/m_e = 25$. The resulting Debye length is 0.0015, which is much smaller than the wavelength, and also much smaller than the grid cell size, thanks to the stability properties of the semi-implicit PIC. We use $\theta = 0.5$ and $\gamma = 0.0$ to show how well the AMR algorithm conserves energy under perfect energy-conserving conditions. The initial number of ion and electron particles per cell is 900 each. The simulation is run till $t = 600$ when the wave just starts to steepen into shocks.

Figure 2.7 shows B_y, the x component of the ion velocity ($U_{x,i}$), the number of ion particles per cell (PPC_i) and the Gauss's Law error $|\nabla \cdot \mathbf{E} - 4\pi q_c|$ at the final time. At this point, the fast wave has steepened into a shock, shown by the sharp jumps in B_y and the electron velocity near $x = -27$ and $x = 5$. Throughout the simulation, the waves pass through the refinement interface smoothly, and no obvious artifacts are observed. The number of particles per cell is kept fairly close to the initial value of $900 \pm 20\%$. Since we pre-split particles in the near vicinity of the refinement level, the PPC number is higher around the refinement interface. These particles are also advected into the coarse grid, where they are rapidly merged to maintain the target PPC ($900 \pm 20\%$). The mean Gauss's Law error without the correction step is 1×10^{-3}, while the mean error with the three-stage correction as described in section 2.2.10 is 1.47×10^{-6}, which is about 0.15% of the uncorrected error.

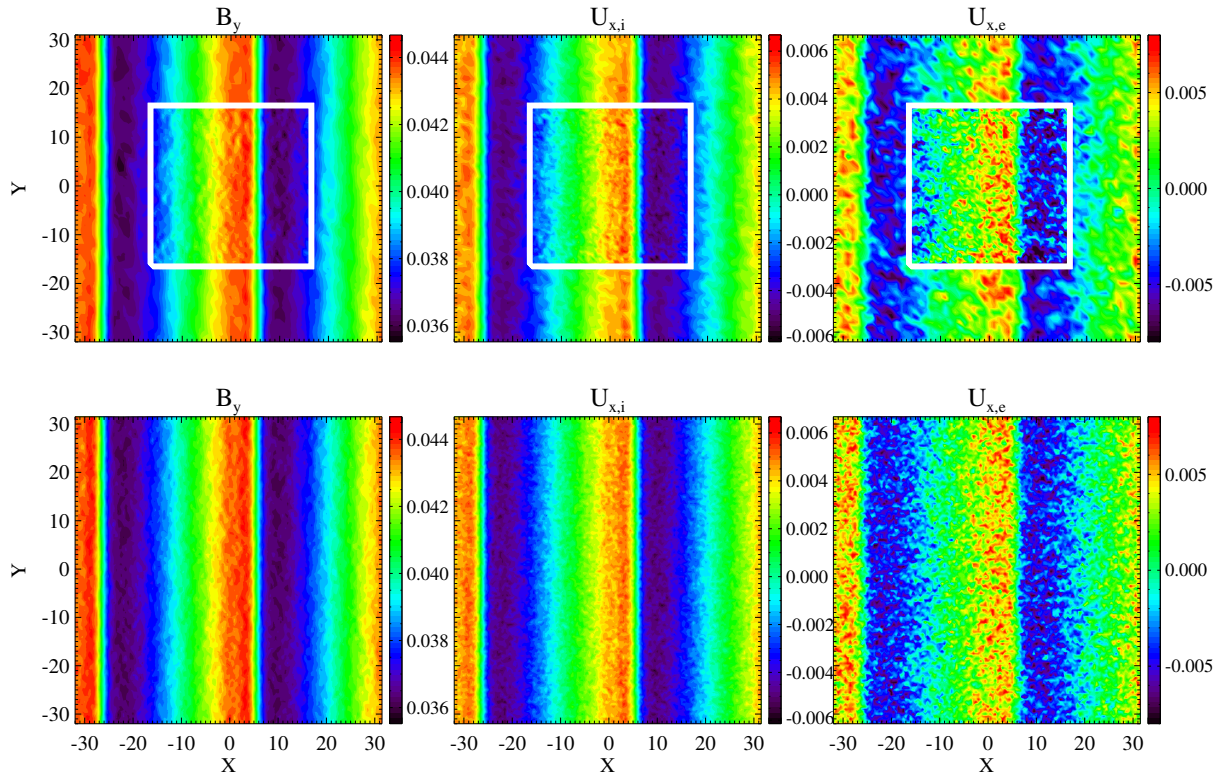


Figure 2.8: Comparison between AMR and high resolution uniform grid fast wave test. B_y, ion velocity $U_{x,i}$ and electron velocity $U_{x,e}$ are shown at $t = 600$ for the AMR simulation (top row) and uniform grid simulation (bottom row). The white box shows the refined region in the AMR simulation.

Figure 2.8 compares B_y, ion velocity in the x direction $U_{x,i}$ and electron velocity in the x direction $U_{x,e}$ between the AMR simulation and the high-resolution uniform grid simulation at $t = 600$. The simulations are in excellent agreement in terms of wave amplitudes and location of the shocks.

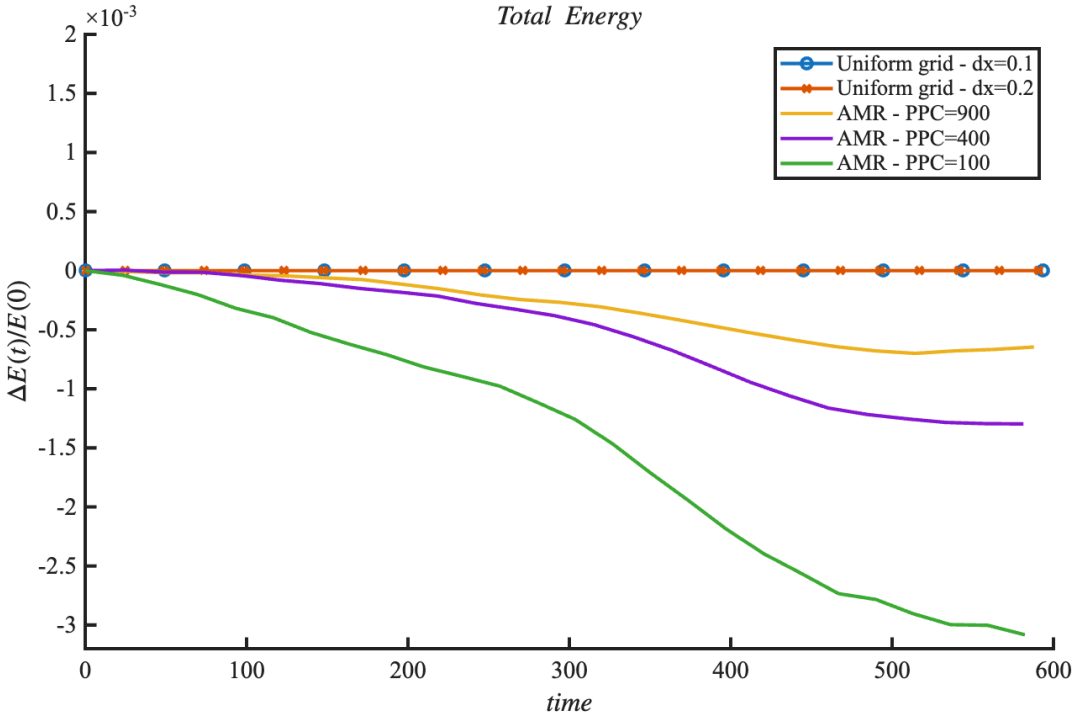


Figure 2.9: Energy conservation plot for the fast wave test. The x-axis represents time, while the y-axis represents the change in total energy of the system normalized to the initial energy. Uniform grid energy plot with two different resolutions as well as AMR energy plot with varying target particles-per-cell number, are shown.

Figure 2.9 shows the total energy conservation for the fast wave test. As expected, the total energy is perfectly conserved in the uniform grid simulations with $\theta = 0.5$ and $\gamma = 0$. The AMR simulation shows a small $\approx 0.06\%$ energy decrease at the end of the simulation for the PPC=900 case. This suggests that the energy error introduced by the AMR algorithm is negligible.

2.3.3 Magnetic reconnection tests

A 2D magnetic reconnection test is performed in a periodic domain ranging from -12.8 to 12.8 in the x-direction and -6.4 to 6.4 in the y-direction, using normalized CGS units. The speed of light is set to $c = 1$. The ion density is uniform throughout the domain and set to $n_i = 0.0975$. Using a proton mass $m_i = 1$ and charge $q_i = 1$, this results in an ion plasma frequency $\omega_{pi} = \sqrt{4\pi n_i e^2/m_i} = 1.107$ and an ion inertial length $d_i = c/\omega_{pi} = 0.903$. The electron mass is reduced such that $m_i/m_e = 25$, giving an electron skin depth $d_e = d_i/5 = 0.18$. The system is initially charge neutral with $n_e = n_i$ and the electric field is zero. The

background magnetic field B_x is defined by two current sheets centered at $y = \pm 3.2$, each with thickness $\delta = 0.5$, as

$$B_x = B_0 \left[-1 + \tanh\left(\frac{y - y_B}{\delta}\right) + \tanh\left(\frac{y_T - y}{\delta}\right) \right] \tag{2.33}$$

where $B_0 = 0.07$, $y_B = -3.2$, $y_T = 3.2$. The initial ions bulk velocity is 0, while the electrons have a bulk velocity in the z-direction such that $J_z = -\partial B_x/\partial y = n_e q_e u_{e,z}$. The ion pressure is constant across the domain, and the ion plasma beta is 1 far from the current sheets. The electron pressure is initially 1/5 of the ion pressure, but is increased locally near the current sheets to maintain total pressure balance.

To initiate reconnection, a localized perturbation is added through the out-of-plane magnetic vector potential A_z, defined as

$$\begin{aligned} A_z = A_0 B_0 \Bigg[&- \exp\left(-\frac{(x - x_T)^2}{G_x^2} - \frac{(y - y_T)^2}{G_y^2}\right) \cos\left(k_x(x - x_T)\right) \cos\left(k_y(y - y_T)\right) \\ &+ \exp\left(-\frac{(x - x_B)^2}{G_x^2} - \frac{(y - y_B)^2}{G_y^2}\right) \cos\left(k_x(x - x_B)\right) \cos\left(k_y(y - y_B)\right) \Bigg] \end{aligned} \tag{2.34}$$

where $A_0 = 0.1$, $G_x = G_y = 0.5$, $k_x = \frac{2\pi}{25.6}$, $k_y = \frac{2\pi}{12.8}$, and the perturbation centers are located at $(x_T, y_T) = (6.4, 3.2)$ and $(x_B, y_B) = (-6.4, -3.2)$. This generates two identical reconnection sites. We perform several tests with different refinement ratios R as well as moving/stationary refinement regions to test various aspects of the method. The magnetic reconnection tests are performed with $\theta = 0.51$ and $\gamma = 0.1$ that were found to be optimal in [14]. Energy conservation will be compared against uniform grid simulations with the same parameters. All the reconnection tests are run till $t = 400$ when the reconnection sites are fully developed. The target PPC per species for these runs is $900 \pm 20\%$.

2.3.3.1 Multi-level refinement with $R = 2$

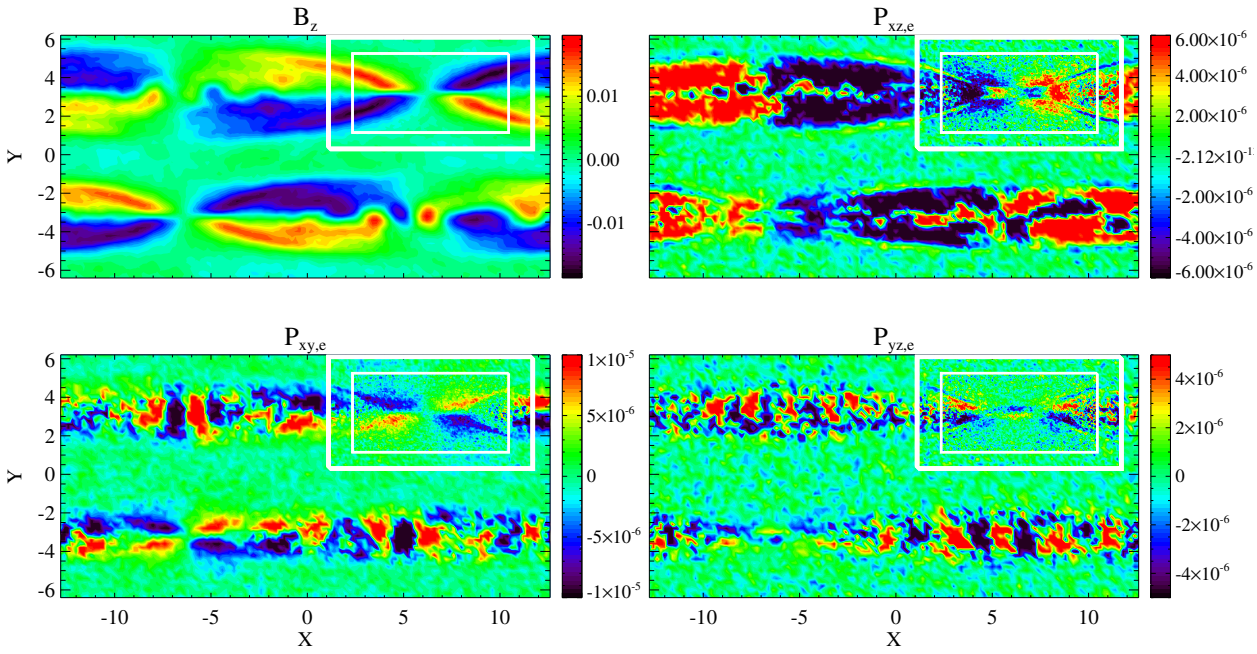


Figure 2.10: 2D double current sheet reconnection test with two levels of refinement at time $t = 400$. Each white rectangle shows a factor of 2 refinement change. Top left: Out-of-plane Hall field B_z. The other three panels show the three off-diagonal elements of the electron pressure tensor.

The base grid resolution is set to $\Delta x_0 = 0.2$ and there is a refinement at $1.2 < x < 11.6$ and $0.4 < y < 6.0$ with $\Delta x_1 = 0.1$ and another refinement at $2.4 < x < 10.2$ and $1.2 < y < 5.2$ with $\Delta x_2 = 0.05$ ($R = 2$). We also set $U_x = 0$ so the reconnection sites do not move. Figure 2.10 shows the out-of-plane Hall field B_z and off-diagonal elements of the electron pressure tensor at $t = 400$. Although the out-of-plane Hall field B_z looks comparable around the refined and coarse reconnection sites, the electron pressure tensor elements are much better resolved in the refined region.

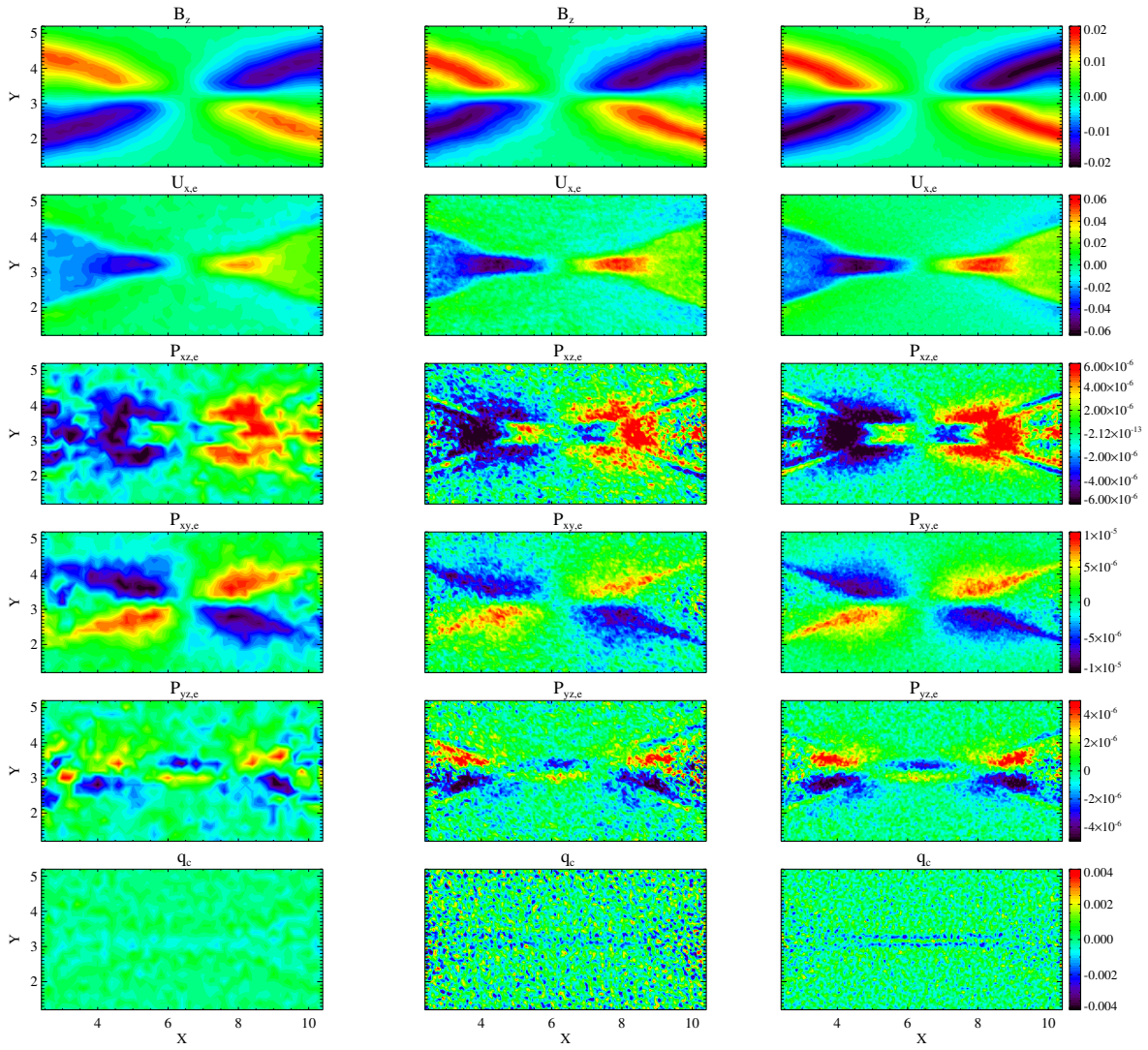


Figure 2.11: Comparison of various quantities near the reconnection site at $t = 400$ for three simulations. The left and right columns show the solution obtained on uniform grids with $\Delta x = 0.2$ and $\Delta x = 0.05$, respectively. The middle column shows the refined grid level $L = 2$ with $\Delta x_2 = 0.05$ of the AMR simulation shown in Figure 2.10. The six rows show the out-of-plane magnetic field B_z, electron velocity component $U_{x,e}$, three off-diagonal pressure tensor elements $P_{xz,e}$, $P_{xy,e}$, $P_{yz,e}$ and the net charge q_c.

Figure 2.11 compares two uniform grid simulations with $\Delta x = 0.2$ and $\Delta x = 0.05$, respectively, and the $L = 2$ grid level of the AMR simulation with $\Delta x_2 = 0.05$. Compared to the coarse grid solution, the AMR solution is much better resolved and resembles the uniform grid solution with $\Delta x = 0.05$, although it is somewhat noisier.

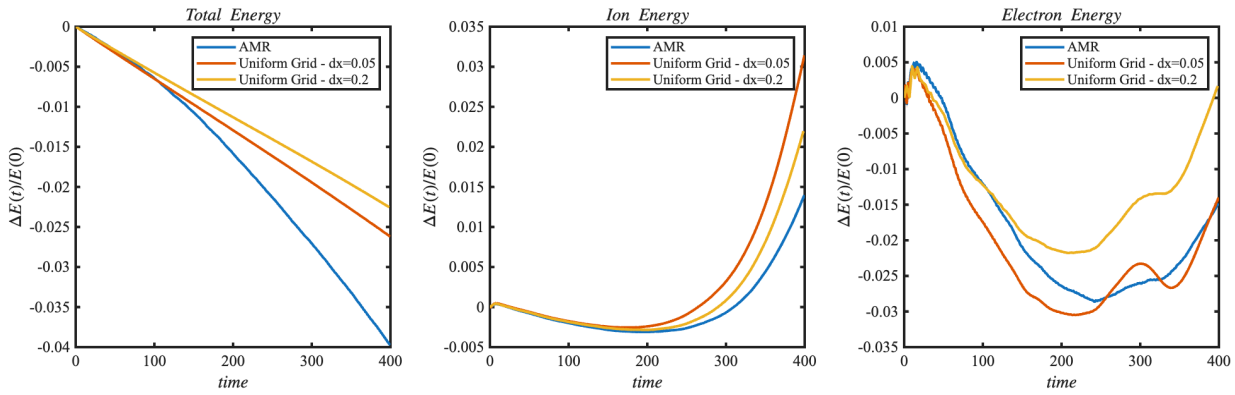


Figure 2.12: Change in energy plot for the multi-level AMR reconnection test. The left figure shows the change in total energy normalized to the initial energy. The middle figure shows the normalized change of energy for ions, while the right figure shows the same for electrons. The results for uniform grid solutions as well as AMR results are shown.

Figure 2.12 shows that the AMR simulation loses a little more energy than the uniform grid solution with $\theta = 0.51$ and $\gamma = 0.1$, which is expected. In the context of MHD-AEPIC, this is negligible as plasma is continuously entering and exiting the PIC domain, so the energy loss is not cumulative. The energy loss is about 4% for the AMR simulation compared to about 2% for the uniform grid simulations. The trend of ion energization is similar to the uniform grid simulations, and the electron energization agrees well with the high-resolution uniform grid simulation.

Figure 2.13 shows the electron and ion velocity distribution functions at $t = 400$ for the AMR case as well as the uniform grid cases. Only particles in the region between $6.8 < x < 7.4$ and $3.0 < y < 3.4$ are considered for all cases. This region is also marked in Figure 2.13. The AMR simulation and the high-resolution uniform grid simulation ($\Delta x = 0.05$) show the same patterns and similar noise levels. In contrast, the coarse uniform grid simulation shows more noise.

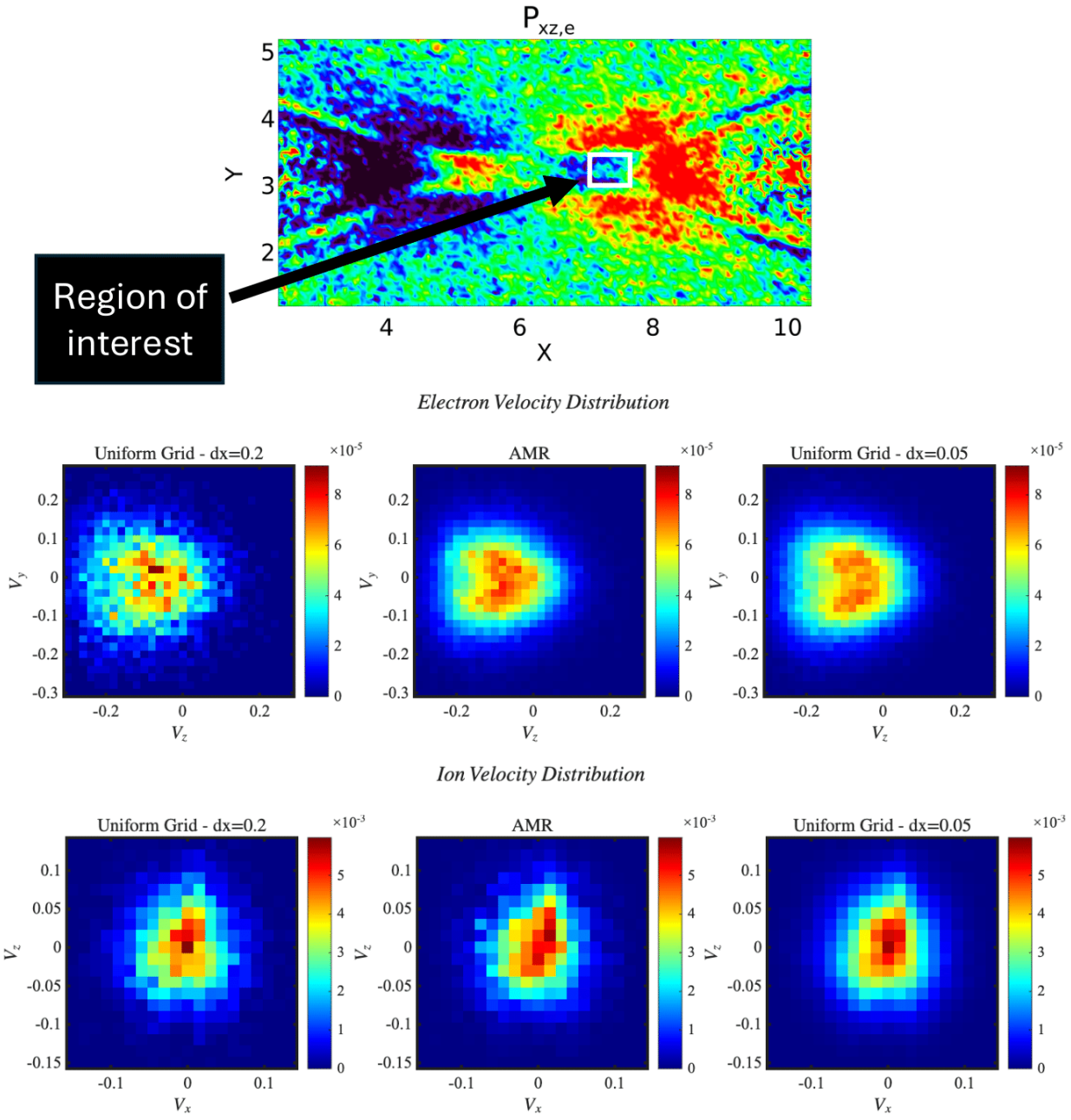


Figure 2.13: The region of interest to study particle velocity distribution functions is shown at the top. Electron and ion velocity space distributions at $t = 400$ for the multi-level AMR simulation and uniform grid simulations are shown below.

2.3.3.2 One level refinement with $R = 4$

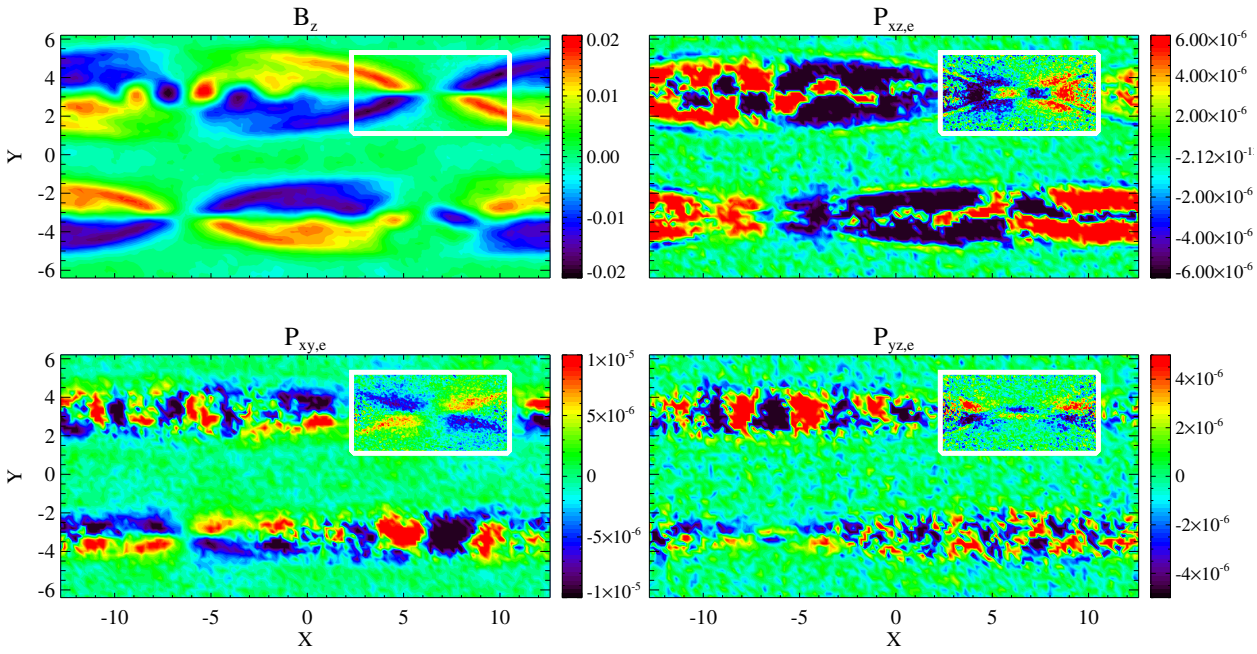


Figure 2.14: Reconnection test results at $t = 400$ with a single AMR level with refinement ratio $R = 4$. The out-of-plane Hall field B_z and the off-diagonal elements of the electron pressure tensor are shown. The white rectangle shows a factor of 4 refinement change ($R = 4$)

The base grid resolution is set to $\Delta x_0 = 0.2$ and there is a single refined level at $2.4 < x < 10.2$ and $1.2 < y < 5.2$ with $\Delta x_1 = 0.05$, which corresponds to $R = 4$. Figure 2.14 shows the out-of-plane Hall field B_z and the three off-diagonal elements of the electron pressure tensor at $t = 400$. The results resemble the multi-level simulation in section 2.3.3.1, which shows that a direct refinement with $R = 4$ and two refinements of $R = 2$ produce similar results. The simulation with a single $R = 4$ grid refinement is less expensive than using two grid levels with $R = 2$ (see section 2.4), but also somewhat more noisy. We attribute this to the more aggressive splitting and merging required for higher values of R. A future improvement can be prescribing enhanced target PPC values in the coarse cells surrounding the refined region.

2.3.3.3 Adaptive refinement with $R = 4$

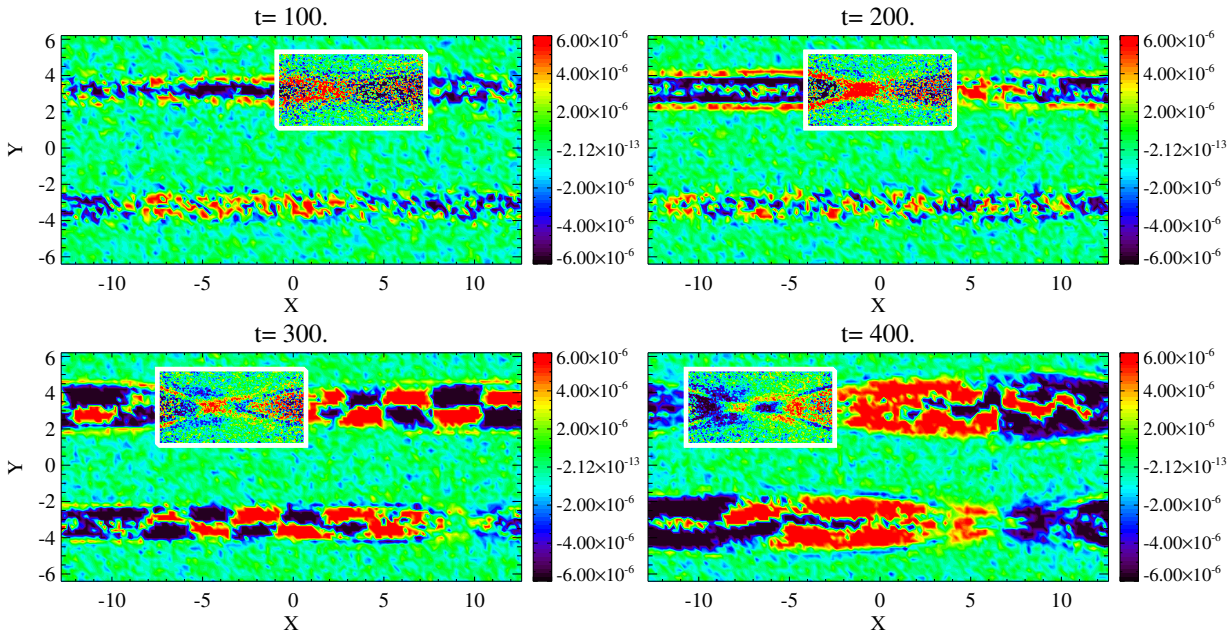


Figure 2.15: Reconnection test results with a single AMR level with refinement ratio $R = 4$ that is moving together with the reconnection site in the $-x$ direction. The $P_{xz,e}$ element of the electron pressure tensor is shown at four different times. The white rectangle shows the dynamically adapted refined region.

We repeat the test in the previous subsection but change the plasma velocity by adding a constant speed $U_x = -0.0325$ in the $-x$ direction so that both reconnection sites move towards the left. The refinement region is also moved left with the same constant velocity by performing a regrid every 20 time steps. Regridding too often can make the simulation slow, while regridding too infrequently can cause the reconnection site to drift out of the refinement region. Regridding every 20 time steps seems to be a good trade-off in this case. It is not too often, and the reconnection site stays inside the refinement region. Figure 2.15 shows the $P_{xz,e}$ element of the electron pressure tensor at multiple time steps. $P_{xz,e}$ at the reconnection site inside the refinement is well resolved, while the unrefined reconnection site is poorly resolved. No visible artifacts are observed.

2.3.3.4 Moving reconnection sites with static mesh refinement

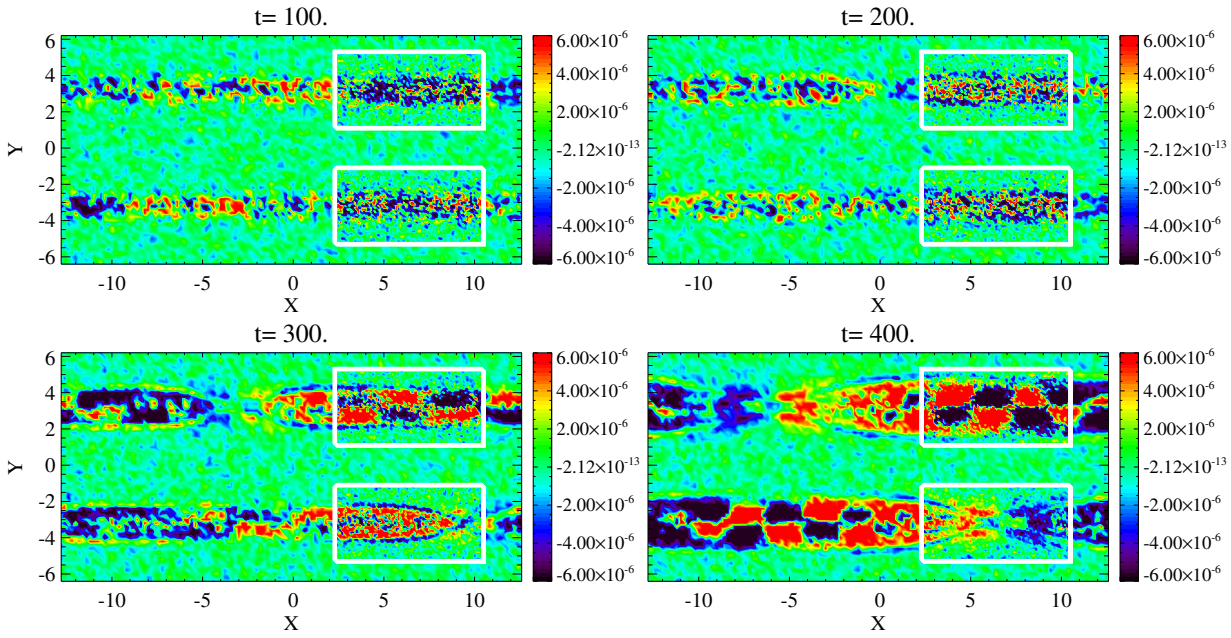


Figure 2.16: Reconnection test with moving reconnection sites. The white rectangles show two disconnected stationary single-level refinements with refinement ratio $R = 2$. The $P_{xz,e}$ element of the electron pressure tensor is shown at four different times. The white rectangles show the refined regions.

The purpose of this test is to check if there are any artifacts at the resolution change when the reconnection site passes through the coarse-fine interface. In practical applications, it is best to follow the motion of the reconnection site as done in subsection 2.3.3.3, but it is important to check if the resolution change induces and/or alters the reconnection process. This test also demonstrates the ability to have multiple disconnected refinement regions. The initial setup is the same as the last test, with both reconnection sites slowly moving towards the left. The base grid has $\Delta x_0 = 0.2$. There are two stationary refinement regions at $2.4 < x < 10.2$, $1.2 < y < 5.2$ and $2.4 < x < 10.2$, $-1.2 < y < -5.2$, respectively, both with $\Delta x_1 = 0.1$ ($R = 2$). The refined region at the top ($1.2 < y < 5.2$) initially contains a reconnection site, and the site slowly moves out of the refinement region towards the left, while the refined grid at the bottom initially does not contain a reconnection site, but a reconnection site slowly drifts into this region. Figure 2.16 shows the $P_{xz,e}$ element of the electron pressure tensor at four different times.

The reconnection site that moved into the bottom refinement is still well resolved, while the reconnection site at the top becomes poorly resolved as it leaves the refined grid. No artifacts are observed as reconnection sites cross the resolution change interface.

2.4 Speed-up analysis of AMR PIC

We can estimate the expected speed-up due to AMR by taking the ratio of the total computational work done on a uniform grid and the work done on the AMR grid. For simplicity, let us consider only one refinement level that occupies a fraction f of the computational domain. Also, we only consider the ECSIM solver, as Gauss's law correction is expected to be less expensive and have a similar speed-up ratio.

The total computational work:

$$W_t = W_m + W_p + W_g \tag{2.35}$$

consists of the particle mover W_m and the field solver that itself involves work W_p that is proportional to the number of particles (depositing the current to the grid and calculating the mass matrix) and W_g that is proportional to the number of grid cells (solving the implicit equation for the electric field). We assume that the number of iterations is similar on all grids, although this may be a rather crude approximation. We also assume that the number of particles per cell is constant, thanks to the particle splitting and merging algorithm.

The particle mover is performed for all particles on a given grid level. The work for the AMR grid W_m^a can be written as a function of the work on a uniform fine grid W_m^u:

$$W_m^a = fW_m^u + (1-f)rW_m^u = (r + f - rf)W_m^u \tag{2.36}$$

where the first term is the work done on the refined level, and the second term is the reduced work on the coarse level, excluding the refined part. The reduction factor is $r = 1/R^D$, where R is the refinement ratio and D is the number of spatial dimensions.

The current and mass matrix calculations are proportional to the number of particles, but, unlike the particle mover, they are performed on all underlying grid levels. Consequently, the work on the AMR grid is

$$W_p^a = 2fW_p^u + (1-f)rW_p^u = (r + 2f - rf)W_p^u \tag{2.37}$$

where the factor of 2 is due to having two grid levels in the refined region.

Finally, the field solver is done on the full base-level grid, including the part that is covered

by the refinement. The work on the AMR grid can be approximated as

$$W_g^a = fW_g^u + rW_g^u = (r+f)W_g^u \tag{2.38}$$

Using the previous formulas, the speed-up can be written as:

$$S = \frac{W_t^u}{W_t^a} = \frac{W_m^u + W_p^u + W_g^u}{(r+f-rf)W_m^u + (r+2f-rf)W_p^u + (r+f)W_g^u} \tag{2.39}$$

Introducing the fractions of time spent on the various tasks on the uniform grid, $M := W_m^u/W_t^u$ and $P := W_p^u/W_t^u$, the formula simplifies to

$$S = \frac{1}{r + f(1+P-rM-rP)} \approx \frac{1}{r+f(1+P)} \tag{2.40}$$

where in the approximation $rM + rP < r = R^{-D} \ll 1 + P$ was neglected. In the limit of $f \to 0$, the speed-up is $S = 1/r$ as expected. For a finite f, the speed-up is reduced due to the extra calculations in the refined region and the particle-related W_p work done on multiple grid levels in the refined region.

The approximate formula can be easily generalized to multiple grid levels. Let f_L be the fraction of the full computational domain occupied by level L grids, with $L = 0 \ldots L_{\max}$ and $f_0 = 1$ for the base grid. The work performed on level L is reduced by a factor of $r^{L_{\max}-L}$ compared to the uniform fine grid with the same resolution as level $L_{\max}$. In addition, W_p has to be performed on all L underlying grid levels, so the approximate formula becomes:

$$S \approx \frac{1}{\sum_{L=0}^{L_{\max}} f_L r^{L_{\max}-L}(1+LP)} \tag{2.41}$$

For $L_{\max} = 1$, this is the same as the approximate formula in (2.40). In the limit of $f_L \to 0$ for all levels $L > 0$, we get the expected $S = 1/r^{L_{\max}}$ relation.

In the sections below, we compare the theoretical speed-ups with the observed speed-ups of AMR simulations versus uniform grid runs with resolution set to the highest AMR resolution. Both AMR and uniform grid simulations are run for 100 steps in serial without the Gauss's law correction step, as it is still not optimized for speed. We expect a similar speed-up with the Gauss's law correction step when it is optimized.

Since we are pre-splitting particles in two coarse cells surrounding the refinement region, for simplicity, we also include this pre-splitting region in the calculation of the refinement fraction f.

2.4.1 Fast wave test speed-up

The fast wave test in subsection 2.3.2 has $L_{max} = 1$ refinement level with refinement ratio $R = 2$ that occupies $f_1 = 0.25$ fraction of the domain. The maximum work reduction is $r = 1/R^D = 1/4$. From the uniform grid run, we get that $P = 0.24$ part of the workload is spent on particle-related tasks in the semi-implicit solver. The expected speed-up from eq. (2.41) is $S_{exp} = 1.79$. The actual speed-up we observed was $S_{act} = 1.85$, which is very close to the expected value.

2.4.2 Multi-level (R=2) static reconnection test speed-up

The reconnection test with multi-level refinement in subsection 2.3.3.1 has two refinements with $f_1 = 0.20$ and $f_2 = 0.12$, respectively, both with $R = 2$ so that $r = 1/R^D = 1/4$. From the uniform grid run, we get $P = 0.26$. Using $L_{max} = 2$, eq. (2.41) gives $S_{exp} = 3.41$. Actual speed-up is $S_{act} = 3.29$, which is very close to the expected value.

2.4.3 Single (R=4) static refinement reconnection test speed-up

The reconnection test with a single $R = 4$ refinement in subsection 2.3.3.2 has $f_1 = 0.13$. We have $r = 1/R^D = 1/16$ and $P = 0.26$ from the uniform grid run. Using $L_{max} = 1$, eq. (2.41) gives $S_{exp} = 4.41$. The actual value is $S_{act} = 3.90$, which is a bit slower but still very close.

2.4.4 Single (R=4) adaptive refinement reconnection test speed-up

The reconnection test with a single $R = 4$ adaptive refinement in subsection 2.3.3.3 has $f_1 = 0.13$. We have $r = 1/R^D = 1/16$ and $P = 0.26$ from the uniform grid run. Using $L_{max} = 1$, eq. (2.41) gives $S_{exp} = 4.41$. The actual value is $S_{act} = 3.87$, which shows that the computational overhead of the adaptive refinement is small and the speed-up is still very close to the stationary refinement case.

2.5 Conclusions

We have developed a new algorithm for a semi-implicit particle-in-cell method with adaptive mesh refinement. Semi-implicit PIC allows using different grid resolutions because it does not have any spatial stability restrictions. Our method fully couples the fields and uses a single set

of particles so that the complete velocity distribution function is shared between refinement levels. Gauss's Law is satisfied across all refinement levels, which helps to maintain an accurate and stable solution for long time integration. The algorithm does not need a buffer zone at refinement interfaces, unlike other AMR explicit PIC methods. Merging and splitting of particles keep the code efficient. The AMR speed-up is well in line with the expected speed-up in all cases. A possible improvement in efficiency would involve using different time steps at different grid levels (subcycling). This option will be explored in the future. We plan to implement subcycling and electric field smoothing based on [34].

While the AMR-PIC implementation is parallelized, the load balancing is not yet optimized. The criteria for choosing regions of refinement still need to be designed and implemented. In the future, we will use the new AMR-PIC scheme as part of the MHD-AEPIC framework [50, 13] to model the global magnetosphere while still resolving electron-scale physics close to the reconnection sites. Since the uniform grid PIC coupling is already in place, we can easily extend it to the AMR PIC model.

CHAPTER 3

Modeling Kinetic Reconnection Onset in Global Magnetospheric Simulations

3.1 Introduction

Magnetic reconnection in Earth's magnetotail is the fundamental mechanism that enables the explosive conversion of magnetic energy into plasma kinetic energy during substorms [7, 61]. Despite being studied for many years, the precise physical processes that lead to the onset of reconnection in the magnetotail remain a topic of active research and debate [19, 24, 25, 37]. It is well understood that reconnection in the magnetotail requires the formation of a thin current sheet [51, 41, 39]. Many studies [45, 46, 6] show that this current sheet thinning leads to electron tearing mode instability, which in turn triggers reconnection. [36] used fully kinetic particle-in-cell (PIC) simulations to show that in near-Earth tail reconnection, the electron tearing mode instability and reconnection onset are preceded by an enhancement of electron pressure anisotropy $T_\perp/T_\parallel \approx 1.1 - 1.3$ where $T_\perp$ and $T_\parallel$ are the perpendicular and parallel temperatures with respect to the magnetic field direction, respectively.

Recent MMS observations [26, 27, 60] suggest that reconnection onset may be a multistage process, starting with an electron-only reconnection stage. [38] used 2.5D kinetic simulations to demonstrate that a quiet current sheet can transition into "electron-only" reconnection [44], characterized by fast electron outflows without immediate coupling of ion dynamics or significant ion heating. This transitional phase suggests hierarchical coupling, where electron-scale dynamics precede full-scale, ion-coupled reconnection. Furthermore, [53] used PIC simulations to identify specific signatures in electron phase-space distributions like pressure non-gyrotropy and "lemon-shaped" distributions that occur before the formation of an X-line.

Although standalone PIC studies have provided critical insights into onset microphysics,

[1]This chapter was adapted from a manuscript that is currently under review in *Journal of Geophysical Research: Space Physics*. Yuxi Chen and Gabor Toth are coauthors.

they are typically performed in isolated domains with artificially imposed boundary conditions and externally prescribed drivers. In such configurations, the macroscopic evolution of the magnetotail is effectively decoupled from the global magnetosphere, leaving open the question of how global magnetospheric dynamics self-consistently trigger and respond to these intrinsic kinetic instabilities. Moreover, traditional magnetohydrodynamic (MHD) models, while useful for global dynamics, are inadequate for capturing the kinetic physics essential for the onset. In MHD, reconnection is often driven by numerical resistivity, and current sheet thickness is typically determined by grid resolution rather than physical scales.

In this study, we address these limitations using a coupled MHD–PIC framework in which a fully kinetic PIC region is self-consistently embedded within a global magnetotail MHD simulation. In contrast to previous standalone PIC studies, the boundary conditions of the PIC domain are not artificially imposed but are supplied dynamically by the surrounding MHD solution. The large-scale model captures magnetotail stretching, plasma sheet convection, and current sheet thinning driven by global magnetospheric dynamics, while the embedded PIC region resolves ion and electron kinetic scales within the near-tail region where reconnection develops. We use a spatially 2-dimensional (2D) model to make the simulations more affordable and make systematic parameter studies feasible. The 2D model captures most of the essential physics and provides a pathway to future 3D studies of reconnection onset. The two parameters that are varied in this study are the ion-electron mass ratio (m_i/m_e) and the kinetic scaling factor (f). The kinetic scaling factor is used to artificially increase the ion and electron scales [55, 48] in the PIC model and the ion scales in the Hall region, which allows us to save significant computational resources while still capturing the essential physics of reconnection onset.

Section 3.2 describes the simulation setup and the coupled MHD-PIC model. Section 3.3 presents a systematic convergence study to determine the optimal PIC parameters for accurately capturing reconnection onset while keeping computational costs manageable. This section also establishes a grid convergence criterion for different parameter sets. It also discusses the current sheet thickness at reconnection onset for different values of these scaling parameters, as well as how ideal and Hall MHD models are insufficient for capturing the physics of reconnection onset. A detailed discussion of the physics of reconnection onset in the magnetotail as revealed by our simulations and a chronological description of the different stages of reconnection onset as the system evolves from a quiet current sheet to a fully developed reconnection site is also provided in this section. We summarize our findings in Section 3.4.

3.2 Model Description

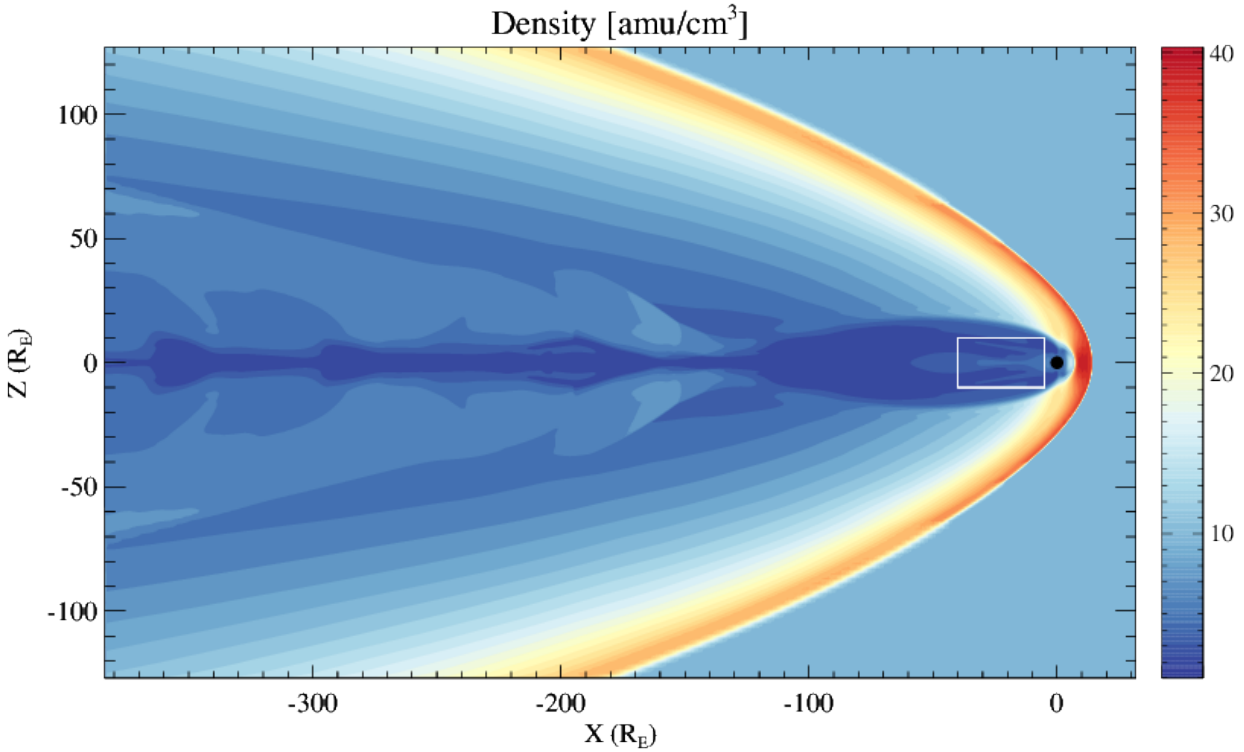


Figure 3.1: Overview of the simulation setup. The MHD domain spans across the entire figure while the PIC domain is represented by the white rectangle.

To study the onset of reconnection in the magnetotail, we use a magnetohydrodynamics with embedded particle-in-cell (MHD-EPIC) model [16, 50, 13]. MHD-EPIC uses MHD to describe the bulk of the magnetospheric plasma, while a localized PIC region is used to study kinetic physics. The MHD and PIC models are two-way coupled. The MHD domain extends from $32R_E > x > -384R_E$ and $128R_E > y > -128R_E$, where R_E is the radius of Earth. The PIC domain is a rectangular box extending from $-5R_E > x > -40R_E$ and $10R_E > y > -10R_E$. The entire MHD domain is shown in Figure 3.1 along with the PIC domain highlighted in white.

The inner boundary is at $2.5R_E$, where we set the number density to $5\,\mathrm{cm}^{-3}$. The pressure boundary condition has zero gradient (floating). The internal magnetic field is a 2D dipole aligned with the Y axis, with a strength 3110 nT that is 10 times weaker than the 3D dipole strength, so that the magnetopause stand-off distance is roughly $10\,R_E$. At the inner boundary, the radial component of the magnetic field is fixed to the dipole value, while the tangential component is floating. The radial velocity is set to zero, while the tangential

velocity has zero gradient.

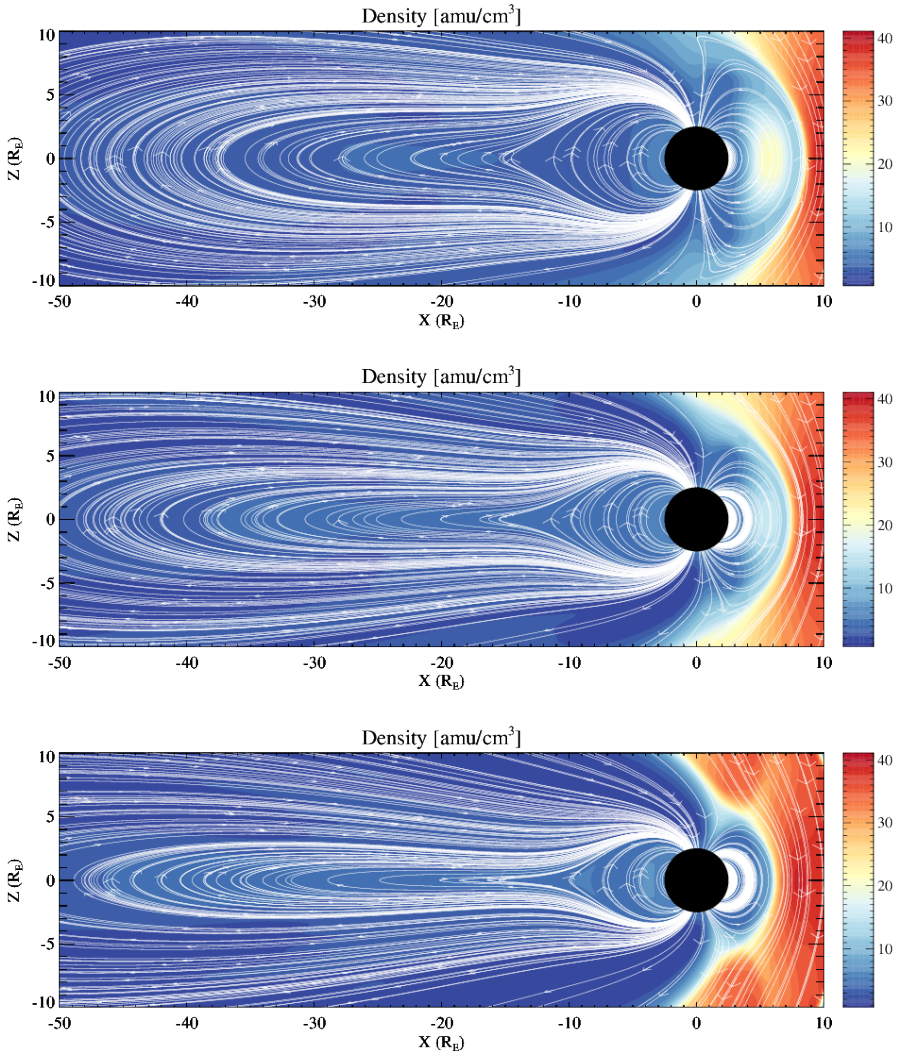


Figure 3.2: Density and magnetic field lines as the magnetotail elongates. The top panel is at t = 50 minutes, the middle panel is at t = 60 minutes, and the bottom panel is at t = 70 minutes.

We solve Hall MHD around the PIC region extending from $-50R_E > x > -30R_E$ and $22R_E > y > -22R_E$ to ensure that the Hall physics is captured in the region where reconnection occurs. The rest of the MHD domain solves ideal MHD. The PIC model uses the Gauss-law Satisfying Energy Conserving Semi-Implicit scheme [33, 14] that allows changing the grid cell size and time step based on accuracy considerations rather than stability requirements. Initially, there are 400 electron and 400 ion macro-particles in each PIC cell. We use particle merging and splitting [14] to keep the total number of particles in each cell within $400 \times (1 \pm 20\%)$.

The setup is initialized in a steady-state configuration with solar wind having density $10\,\mathrm{cm}^{-3}$, temperature 10^5 K, x-direction velocity $-600\,\mathrm{km/s}$, and a northward interplanetary magnetic field (IMF) with $B_z = 0.5\,\mathrm{nT}$. There is no PIC region during this initialization phase. The IMF magnetic field is then linearly turned southward over a period of 1 hour from $B_z = 0.5\,\mathrm{nT}$ to $B_z = -4\,\mathrm{nT}$. The system is allowed to evolve for 1 hour, which allows the magnetotail to elongate. After 1 hour, the PIC region is turned on, and the system is allowed to evolve. The tail elongates further, as can be seen in Figure 3.2, and the reconnection site forms self-consistently. Since this study involves simulations with different grid resolutions, the MHD grid resolution around the PIC region is also refined to match the PIC grid resolution.

3.3 Simulation Results

3.3.1 Resolving the electrons scale

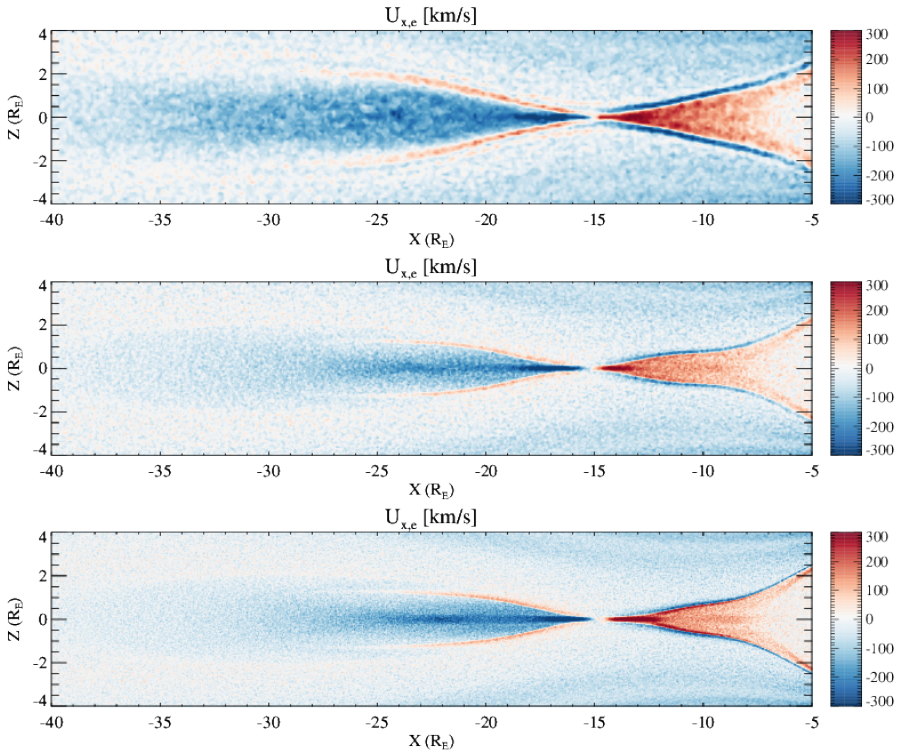


Figure 3.3: Electron velocity in the x-direction with $f = 16$, $m_i/m_e = 25$ for three runs with PIC grid resolutions $\Delta x = 1/8$, $1/16$, and $1/32\,R_E$ (top to bottom) at $t = 95\,\mathrm{m}$. The reconnection occurs at about the same location $x \approx -15.4\,R_E$ and at the same time for the $\Delta x = 1/16$ and $1/32\,R_E$ runs, while the reconnection occurs earlier and closer to Earth for the $\Delta x = 1/8\,R_E$ run.

We want to ensure that the grid is fine enough to resolve electron-scale physics. In particular, the resolution must resolve the electron inertial length to accurately model reconnection. Three runs with grid resolutions $\Delta x = 1/8, 1/16$ and $1/32\, R_E$ are performed. A kinetic scaling factor $f = 16$ and ion-electron mass ratio $m_i/m_e = 25$ is used for these runs. Figure 3.3 shows the electron velocity in the x-direction at t = 95 minutes, a few minutes after reconnection onset, for all three runs. The figure is zoomed in on the PIC region in the near-Earth magnetotail. The electron jet in the simulation with $\Delta x = 1/8\, R_E$ looks very different from the other two runs, which suggests that it is not grid converged. The simulations with $1/16\, R_E$ and $1/32\, R_E$ agree with each other very well. The true ion inertial length in the reconnection inflow region is $d_{i,real} \approx 0.03 R_E$. Since we are using a kinetic scaling factor $f = 16$, the scaled ion inertial length is $d_i \approx 0.48 R_E$, and with $m_i/m_e = 25$, the scaled electron inertial length is $d_e = d_i/\sqrt{m_i/m_e} \approx 0.1 R_E$. With a grid resolution of $\Delta x = 1/16\, R_E$, we have roughly 1.5 cells per electron inertial length. While we only show the convergence study for one set of parameters, we have performed the same convergence study for other sets of parameters, and we found that convergence is always achieved when we have roughly 1.5 cells per electron inertial length. For the system in this paper, a simple relation can be derived to determine the grid resolution required to resolve the electron inertial length:

$$\Delta x_c := \frac{d_e}{1.5} = \frac{d_{i,real}}{1.5} \frac{f}{\sqrt{m_i/m_e}} \tag{3.1}$$

Table 3.1: Timing and location of reconnection onset for different PIC grid resolutions.

PIC grid resolution $[R_E]$	Onset time [min]	Onset location $[R_E]$	Thickness $[R_E]$
1/8	78 and 79	-18.5 and -15.2	0.50
1/16	81	-15.4	0.33
1/32	81	-15.4	0.31

The timings and locations of reconnection onset for all three simulations are shown in Table 3.1. The $\Delta x = 1/8 R_E$ run reconnects at $-18.5 R_E$ at $t = 78$ mins and $-15.2 R_E$ at $t = 79$ mins. The $\Delta x = 1/16 R_E$ and $\Delta x = 1/32 R_E$ both reconnect at similar times and locations. This suggests that we achieve grid convergence at $\Delta x = 1/16\, R_E$ and any further increase in grid resolution does not significantly change the timing and location of reconnection onset. This further confirms that a grid resolution of roughly 1.5 cells per electron inertial length is sufficient to capture the physics of reconnection onset in the magnetotail.

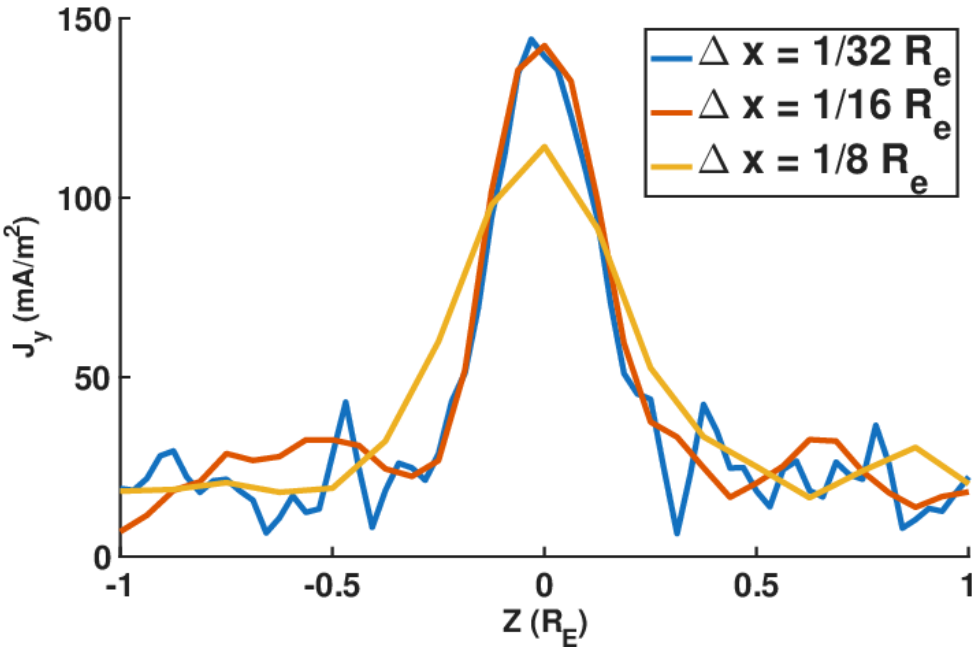


Figure 3.4: Out-of-plane current density, J_y, at the onset of reconnection for three simulations with grid resolutions $\Delta x = 1/8\,R_E$, $1/16\,R_E$, and $1/32\,R_E$, using $f = 16$ and $m_i/m_e = 25$. The profiles for the $\Delta x = 1/16\,R_E$ and $1/32\,R_E$ cases closely overlap, indicating convergence at these resolutions. In contrast, the $\Delta x = 1/8\,R_E$ case exhibits a broader profile, implying a thicker current sheet and a lack of grid convergence at this coarser resolution.

Current sheet thickness (δ) can be determined by plotting the out-of-plane component of the current density J_y along the z direction at the reconnection site, as shown in Figure 3.4. δ is defined as the full width at half maximum (FWHM) of the current density profile. Unlike ideal and Hall MHD, where the current sheet thickness at the reconnection site is determined by the grid resolution, PIC simulations can capture the true physics of reconnection, and therefore, the current sheet thickness must converge to a physical value as the grid resolution is increased. Any further increase in grid resolution beyond the converged grid resolution should not change the current sheet thickness at the reconnection site. Figure 3.4 shows J_y along the z direction at the reconnection site at the time of reconnection onset for all three simulations. The J_y profiles are very similar for the $\Delta x = 1/16\,R_E$ and $1/32\,R_E$ runs, while the current sheet is wider for $\Delta x = 1/8\,R_E$, suggesting that the electron scale physics is not fully resolved at this grid resolution. Quantitatively, $\delta = 0.5, 0.33$ and $0.31\,R_E$ for the $\Delta x = 1/8, 1/16$ and $1/32\,R_E$ resolutions, respectively. Therefore, we can conclude that for this set of parameters ($f = 16$, $m_i/m_e = 25$), we achieve grid convergence at 1.5 cells per electron inertial length.

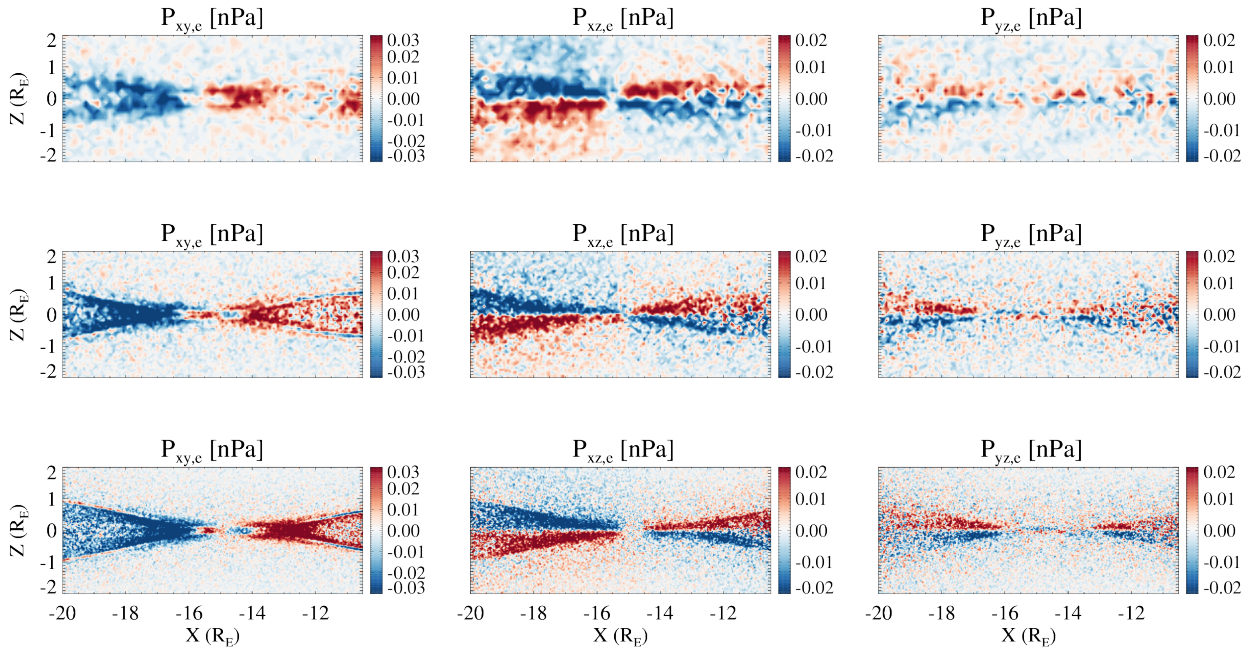


Figure 3.5: Off-diagonal electron pressure tensor components $P_{xz,e}$, $P_{xy,e}$, and $P_{yz,e}$ after the reconnection site has fully formed for the $\Delta x = 1/8\,R_E$, $\Delta x = 1/16\,R_E$, $\Delta x = 1/32\,R_E$ (top to bottom) runs with $f = 16$ and $m_i/m_e = 25$.

Figure 3.5 shows the off-diagonal electron pressure tensor components $P_{xz,e}$, $P_{xy,e}$, and $P_{yz,e}$ after the reconnection site has fully formed for the three runs with different grid resolutions. The simulation with $\Delta x = 1/8\,R_E$ is under-resolved and does not capture all the structures in the electron pressure tensor, while the runs with $\Delta x = 1/16\,R_E$ and $1/32\,R_E$ are very similar and capture the same structures in the electron pressure tensor. If the purpose of the simulation is to study the detailed physics of reconnection, then a grid resolution of 3 cells per electron inertial length might prove beneficial to better capture the structures in the electron pressure tensor, but for the purpose of studying the global reconnection onset dynamics, a grid resolution of 1.5 cells per electron inertial length is sufficient and offers significant computational savings. Moving forward, the grid resolution will be set to $\Delta x = \Delta x_c$ so that this convergence criterion is satisfied.

3.3.2 Effect of ion-electron mass ratio

This section discusses the effect of the ion-electron mass ratio (m_i/m_e) on the physics of reconnection. We compare the results for $m_i/m_e = 25$ and $m_i/m_e = 100$ while keeping the kinetic scaling factor fixed at $f = 16$. The grid resolutions are $\Delta x_c = 1/16\,R_E$ and $1/32\,R_E$ for $m_i/m_e = 25$ and 100, respectively, to satisfy the convergence criteria in equation 3.1.

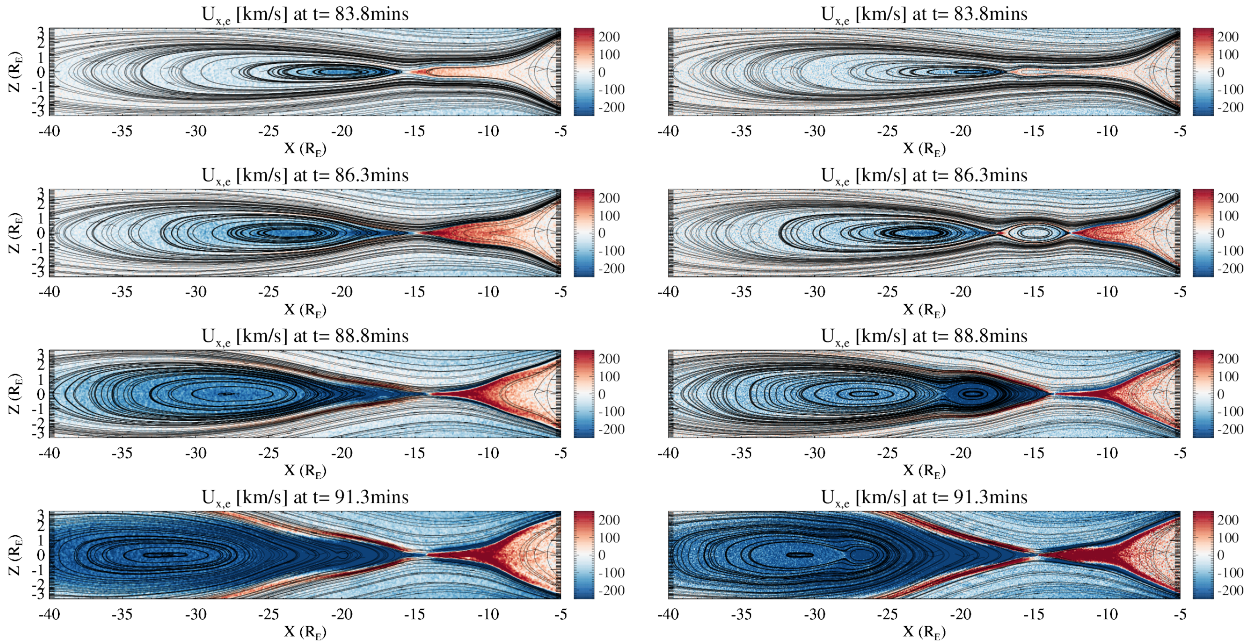


Figure 3.6: Electron velocity in the x-direction at $t = 84, 86.5, 89, 91.5$ minutes for f=16 with mass ratio $m_i/m_e = 25$ (left) and $m_i/m_e = 100$ (right). The reconnection starts at roughly the same time and location for both runs, but the $m_i/m_e = 100$ case has extra flux ropes and reconnection sites that develop in the tail.

Figure 3.6 shows the electron velocity in the x-direction for $m_i/m_e = 25$ and 100 at $t = 84, 86.5, 89, 91.5$ minutes. The reconnection starts at roughly the same time and location for both runs. For the $m_i/m_e = 100$ case, another reconnection site appears at around $x = -13\,R_E$. The secondary reconnection site then becomes dominant, while the original reconnection site slowly dissolves and is pushed further away tailward. The secondary reconnection sites do not change the global picture of reconnection onset drastically, but this process appears to be sensitive to various parameters, including the electron-ion mass ratio. The development of multiple reconnection sites is discussed in more detail in section 3.3.7.

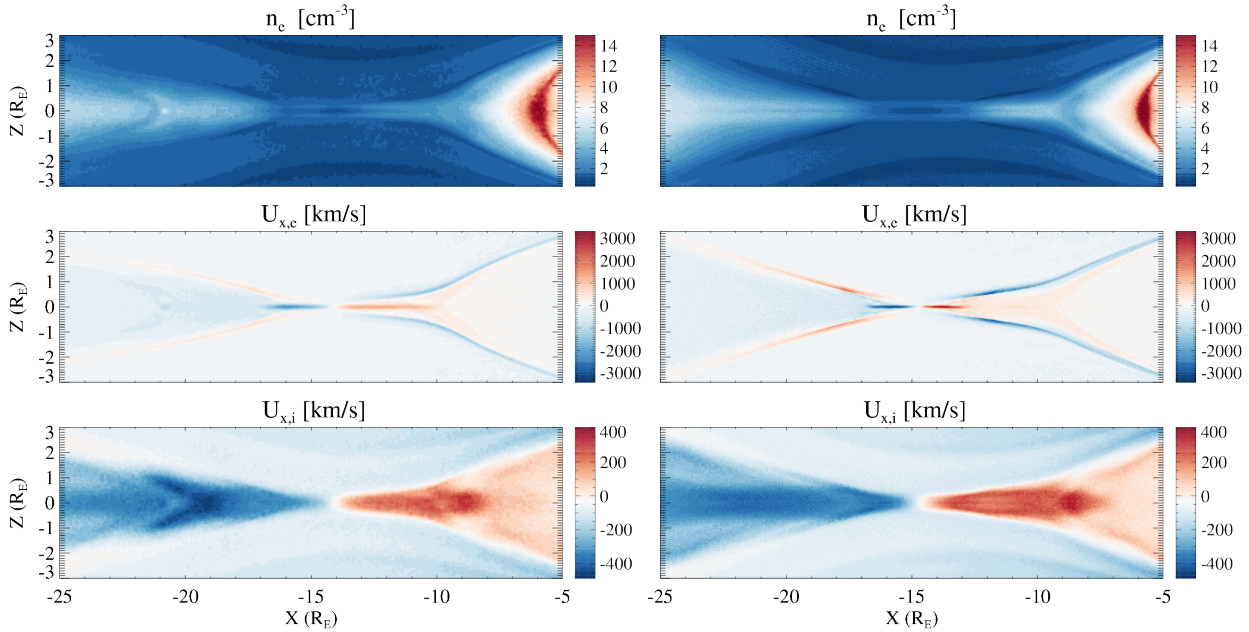


Figure 3.7: Electron number density, electron velocity in the x-direction, and ion velocity in the x-direction for $m_i/m_e = 25$ (left) and $m_i/m_e = 100$ (right) at t = 92 minutes. Both simulations show similar electron number densities and ion velocities, while the electron velocity is higher for the $m_i/m_e = 100$ case. The electron jet in the $m_i/m_e = 100$ case is also narrower and shorter than the $m_i/m_e = 25$ case.

Figure 3.7 shows the electron number density, and the electron and ion velocities in the x-direction for $m_i/m_e = 25$ and 100 at $t = 92$ minutes, which is after reconnection onset. The electron number densities and ion velocities are very similar for both runs, indicating that the macroscopic evolution is robustly captured by both mass ratios. While the overall dynamics are consistent, the electron velocity in the x-direction is higher for the $m_i/m_e = 100$ case, and the jet is also narrower. This is expected, as the electrons are lighter and consequently the electron Alfvén speed is twice larger, while the electron inertial length, d_e, is twice smaller for the higher mass ratio. One important difference is that in the $m_i/m_e = 100$ case, the electron jet appears a few seconds before the ion jet [38], while this delay is less apparent in the $m_i/m_e = 25$ case. This suggests that a more realistic mass ratio is important to capture the precise temporal decoupling of ion and electron dynamics in the electron diffusion region.

3.3.3 Effect of kinetic scaling

This section discusses the effect of the kinetic scaling factor f on the physics of reconnection. We compare the results for $f = 32$, 16, and 8 while keeping the ion-electron mass ratio fixed at $m_i/m_e = 25$. The grid resolution for all runs is determined by the convergence criteria in equation 3.1.

Table 3.2: Timing and location of reconnection onset for different kinetic scaling factors.

Kinetic scaling factor f	Onset time [min]	Onset location [R_E]
32	75	-17.5
16	81	-15.4
8	87	-15.5

Table 3.2 shows the timing and location of reconnection onset for different values of f. The reconnection onset timing does not converge because a lower kinetic scaling factor requires a thinner current sheet for reconnection onset. It takes more time for the current sheet to reach the required thickness for smaller kinetic scaling factors. The location of the reconnection site, however, converges to around $x = -15.5R_E$ for $f = 16$ and $f = 8$. For $f = 32$, the reconnection site is further away from Earth at around $x = -17.5R_E$. Therefore, we can conclude that kinetic scaling convergence is achieved at $f = 16$. This choice will lead to an onset time that is slightly earlier but will help save significant computational resources.

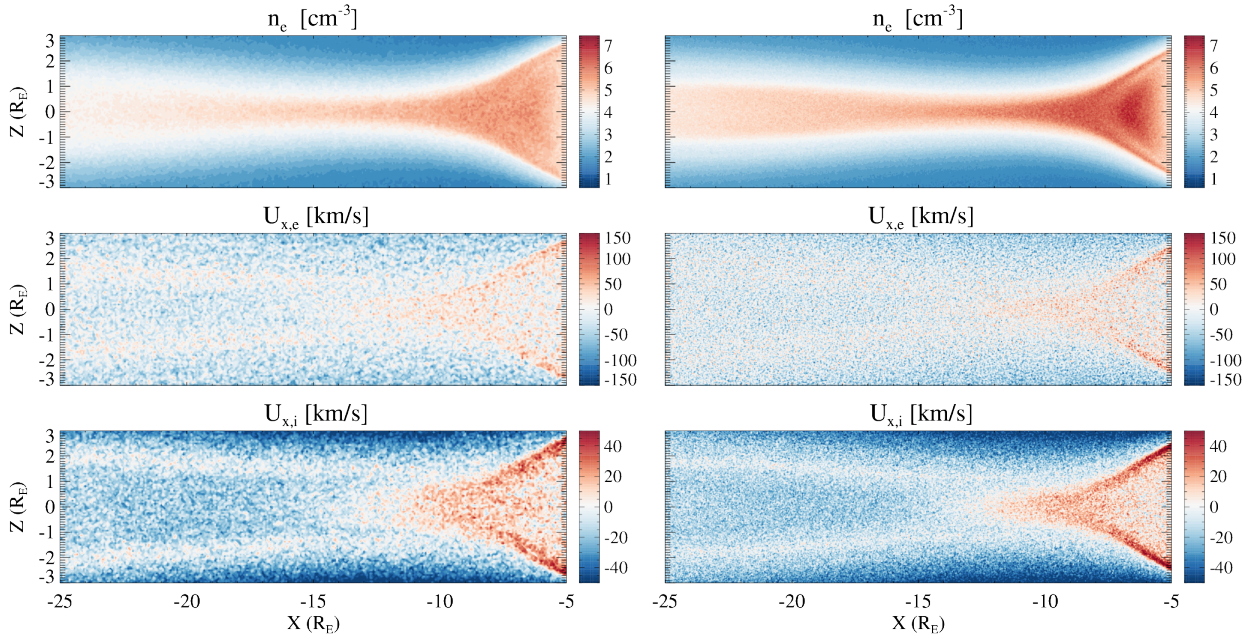


Figure 3.8: Electron number density, electron velocity in the x-direction, and ion velocity in the x-direction for $f = 16$ (left) at t = 76 minutes and $f = 8$ (right) at t = 82 minutes.

Figure 3.8 shows the electron number density, and the electron and ion velocities in the x-direction for $f = 16$ and $f = 8$ at t = 76 and 82 minutes, respectively. These times are chosen since the reconnection onset time is 5 minutes apart so both runs are in a similar "pre-reconnection" state. The ion and electron velocities are very similar for both simulations. The electron number density is slightly higher for the $f = 8$ case, which is expected since the

current sheet is thinner for the $f = 8$ case. These results also show convergence at $f = 16$.

3.3.4 Optimal PIC parameters

Based on sections 3.3.1, 3.3.2, and 3.3.3, the optimal PIC simulation parameters are identified as $f = 16$ for the kinetic scaling factor and $m_i/m_e = 100$ for the ion-to-electron mass ratio. To ensure convergence, a grid resolution of $\Delta x_c = 1.5 d_e = 1/32\, R_E$ is recommended. It is important to note that while we chose $m_i/m_e = 100$ for this study, $m_i/m_e = 25$ can also be used without significantly affecting the global reconnection onset dynamics.

3.3.5 Current Sheet Thickness

Table 3.3: Current sheet thickness δ at reconnection onset for different scaling factors f and mass ratios m_i/m_e using the converged grid resolution Δx_c. For all runs, $\delta \approx 3 d_e$.

f	m_i/m_e	Δx_c $[R_E]$	δ $[R_E]$	δ $[d_i]$	δ $[d_e]$
32	25	1/8	0.59	0.61	3.1
16	25	1/16	0.33	0.70	3.3
16	100	1/32	0.15	0.31	3.1
8	25	1/32	0.14	0.58	2.9

Table 3.3 shows the current sheet thickness (δ) at reconnection onset for different parameter sets. The first and second columns show the kinetic scaling factor and the ion-electron mass ratio, respectively. The third column shows the grid resolution that satisfies the convergence criteria. The fourth column shows the current sheet thickness in R_E, the fifth column shows the current sheet thickness in terms of the ion inertial length d_i, and the sixth column shows the current sheet thickness in terms of the electron inertial length d_e. For all sets of parameters, the current sheet thickness is of around $3\, d_e$. Since the current sheet thickness is of the order of a few electron inertial lengths, irrespective of f and m_i/m_e, this shows the reconnection onset is determined by physics at the electron scales.

3.3.6 Comparison with Ideal and Hall MHD

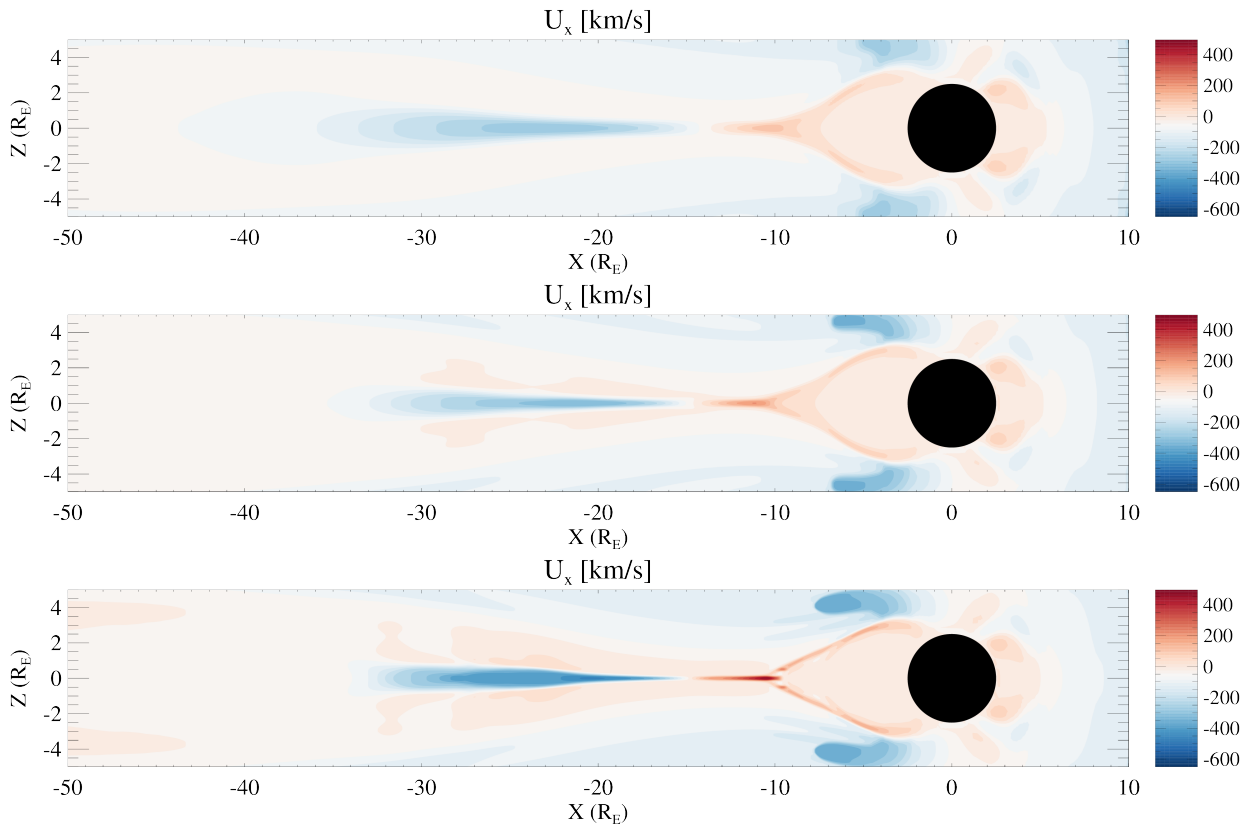


Figure 3.9: Velocity in the x-direction for three ideal MHD simulations with different grid resolutions Δ x = 1/8, 1/16, 1/32 R_E (top to bottom). While the reconnection happens at similar locations, the jet speeds vary significantly.

Figure 3.9 shows the velocity in the x-direction for ideal MHD simulations with different grid resolutions at similar stages of reconnection onset. The reconnection jet velocity increases with increasing grid resolution, which shows that the reconnection in ideal MHD is not converged and is determined by the grid resolution.

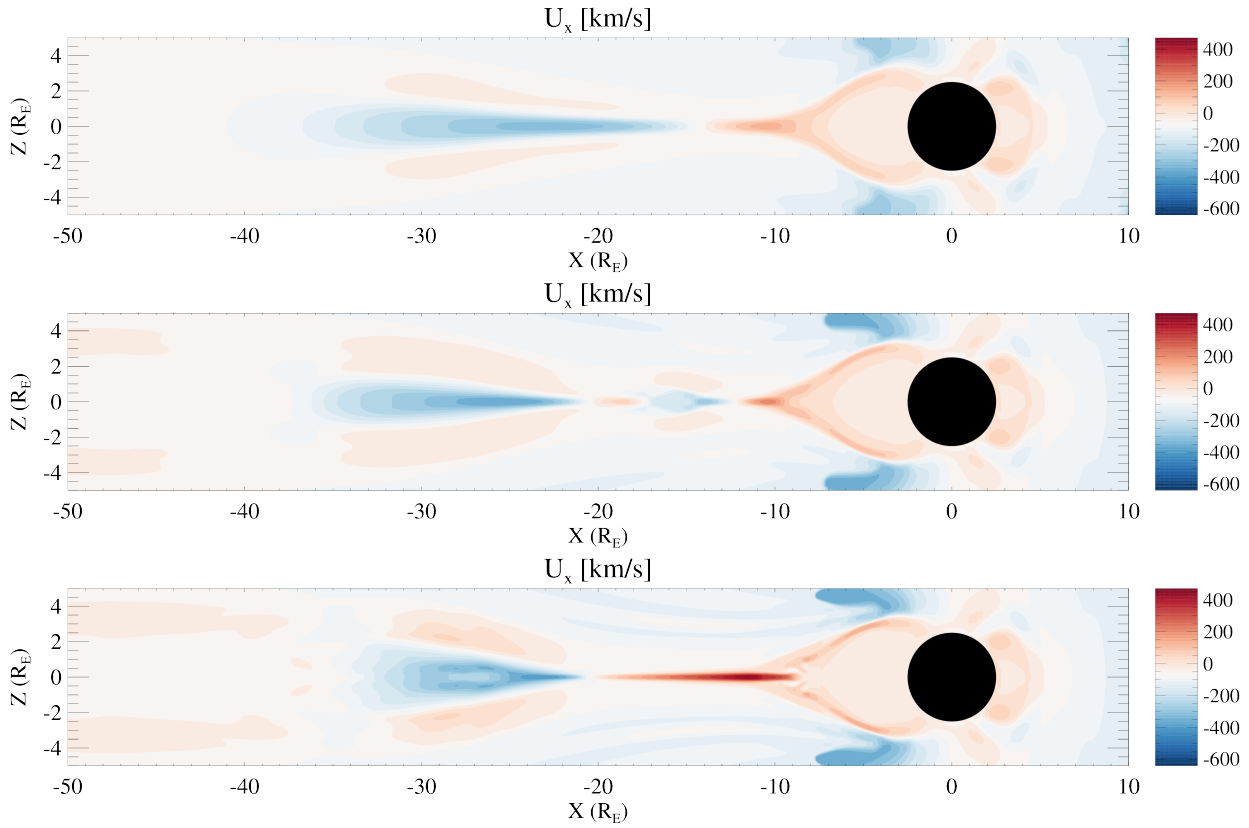


Figure 3.10: Velocity in the x-direction for Hall MHD simulation with different grid resolutions $\Delta x = 1/8, 1/16, 1/32\, R_E$ from top to bottom. Note the variation of the locations of the X-line and the jet speeds.

Similarly, Figure 3.10 shows the velocity in the x-direction for Hall MHD simulations with different grid resolutions at similar stages of reconnection onset. As with ideal MHD, the reconnection jet velocity increases with increasing grid resolution. Additionally, the reconnection location is different for different grid resolutions, which shows that the reconnection in Hall MHD is also not converged and is determined by the grid resolution. This shows that neither ideal MHD nor Hall MHD captures the true physics of reconnection, and the reconnection in these models is grid dependent.

3.3.7 Kinetic Reconnection onset

In this section, we discuss the physics of reconnection onset in the magnetotail using the optimal PIC parameters identified in section 3.3.4. Each stage of reconnection onset is discussed chronologically as the system evolves from a quiet current sheet to a fully developed reconnection site.

Current sheet thinning. When the IMF turns southward, the magnetotail starts to stretch and the current sheet starts to thin as shown in Figure 3.2. The current sheet thinning is driven by the global magnetospheric dynamics and magnetic flux transport.

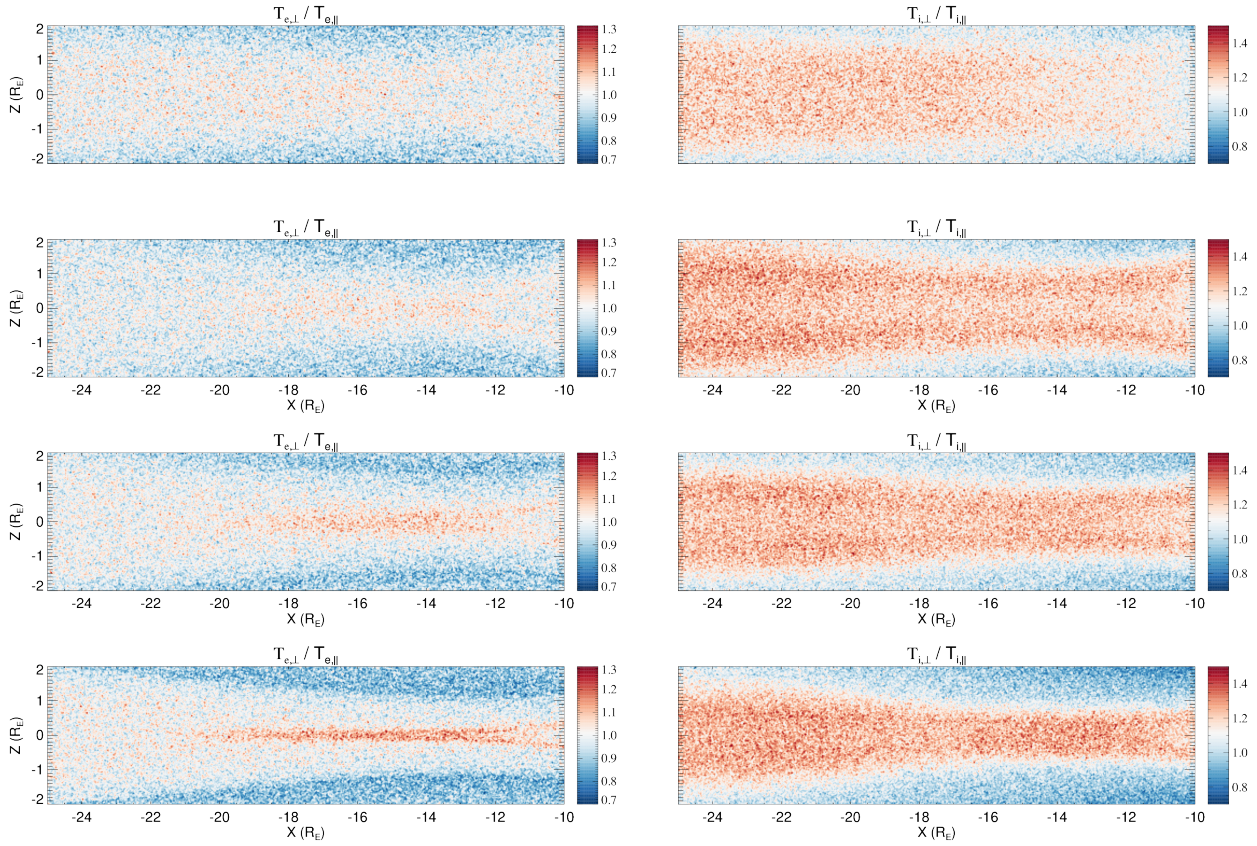


Figure 3.11: Electron temperature anisotropy $T_{e\perp}/T_{e\|}$ (left) and ion temperature anisotropy $T_{i\perp}/T_{i\|}$ (right) at t = 67, 72, 77, and 82 minutes (top to bottom). An electron temperature anisotropy of $T_{e\perp}/T_{e\|} \approx 1.1 - 1.3$ develops in the current sheet just before reconnection onset.

Ion/Electron temperature anisotropy. As the current sheet thins, an ion temperature anisotropy starts to develop. This anisotropy is characterized by $T_{i\perp}/T_{i\|}$, where $T_{i\perp}$ and $T_{i\|}$ are the ion temperatures perpendicular and parallel to the magnetic field, respectively. The ion temperature anistropy slowly grows from $T_{i\perp}/T_{i\|} \approx 1$ at $t = 0$ minutes to $T_{i\perp}/T_{i\|} \approx 1.3 - 1.5$. at $t = 72$ minutes. After $t = 72$ minutes, the ion temperature anisotropy remains roughly constant up until reconnection onset. At $t = 67$ minutes the electrons are isotropic with $T_{e\perp}/T_{e\|} \approx 1$. This anisotropy increases to roughly $T_{e\perp}/T_{e\|} \approx 1.1 - 1.3$ at $t = 82$ minutes Figure 3.11 shows the electron temperature anisotropy $T_{e\perp}/T_{e\|}$ (left) and ion temperature anisotropy $T_{i\perp}/T_{i\|}$ (right) at $t = 67, 72, 77$ and 82 minutes. An electron temperature anisotropy of $T_{e\perp}/T_{e\|} \approx 1.1 - 1.3$ is consistent with previous PIC studies [36].

The electron temperature anisotropy is highest near the neutral line ($y = 0$) and decreases as we move away from the neutral line. The results show that the current sheet thinning first non-iostropizes the ion temperature, and then the electron temperature.

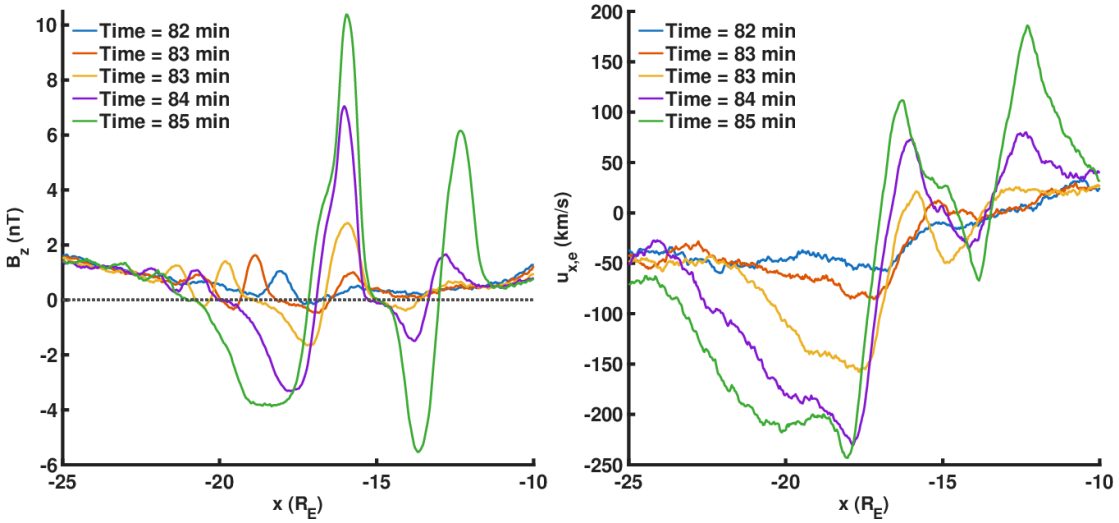


Figure 3.12: B_z and electron velocity in the x-direction ($U_{x,e}$) along $z = 0$ at different times. Every $B_z = 0$ crossing acts as a seed for a reconnection site to develop.

Formation of electron and ion jets. Figure 3.12 shows the B_z component of the magnetic field along the $z = 0$ line at different times. The magnetic field starts to develop small perturbations around $t = 82$ minutes. These perturbations grow and B_z changes sign. Each $B_z = 0$ crossing acts as a seed for a reconnection site to develop. Similar magnetic field perturbations have been found in previous studies [36].

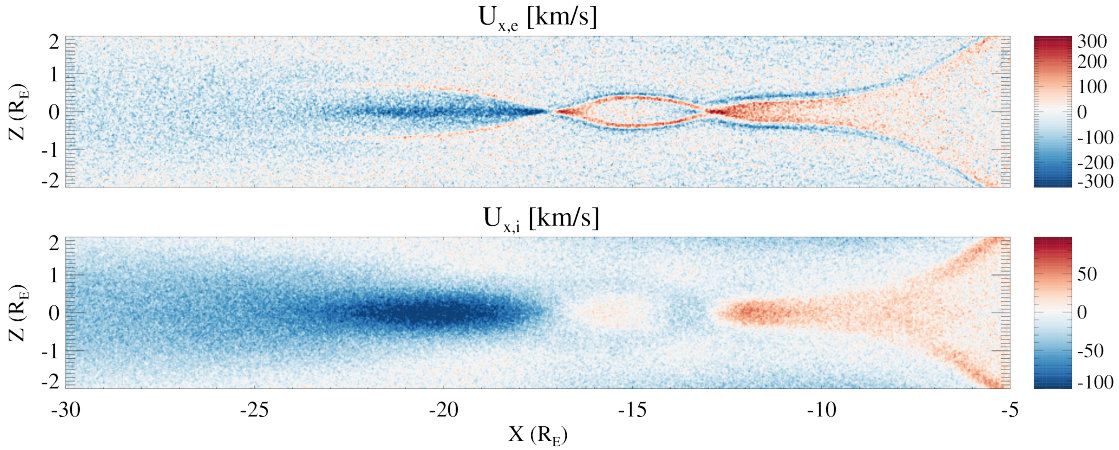


Figure 3.13: Electron and ion velocities in the x-direction at t = 85 minutes.

The first major reconnection site forms at around $x = -16.5R_E$ at around $t = 83$ minutes.

Two minutes later, we see another $B_z = 0$ crossing, at around $x = -13.4R_E$, which leads to the onset of another reconnection site as shown in Figure 3.13.

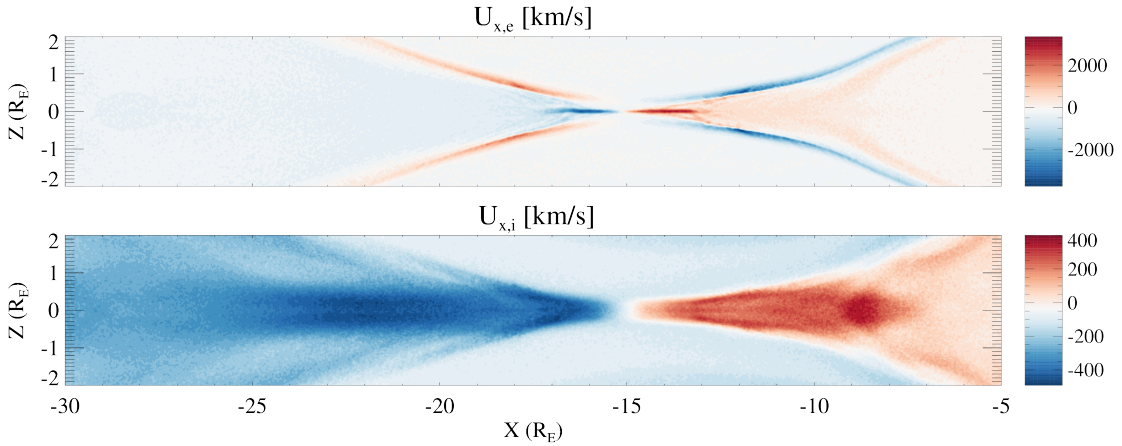


Figure 3.14: Electron and ion velocities in the x-direction at t = 92 minutes.

The second reconnection site eventually dominates, and the first reconnection site slowly dies down and is pushed further away from the Earth, as shown in Figure 3.14. The electron jet speed is roughly 4000 km/s, which is ten times higher than the ion jet speed and is consistent with $v_{e,jet}/v_{i,jet} = \sqrt{m_i/m_e} = \sqrt{100} = 10$ The maximum ion jet velocity achieved in the simulation is around 750 km/s minutes while the Alfvén speed in the inflow region is roughly $800 - 900$ km/s. This shows that the ions in the outflow region move with speeds very close to the inflow Alfvén speed. The development of multiple reconnection sites is a common feature in our simulations and appears to be sensitive to various parameters, including the electron-ion mass ratio as discussed in section 3.3.2. In general, the thinner the current sheet, the more $B_z = 0$ crossings we see, and more possible reconnection sites can develop.

Electron and ion heating. Figure 3.15 shows the total, parallel, and perpendicular electron and ion temperatures at $t = 92$ minutes. The total electron temperature shows uniform heating in the outflow region, while the parallel and perpendicular electron temperatures reveal that very close to the neutral line ($y = 0$), the electrons are heated preferentially in the field perpendicular direction, while the parallel electron temperature is lower near the neutral line.

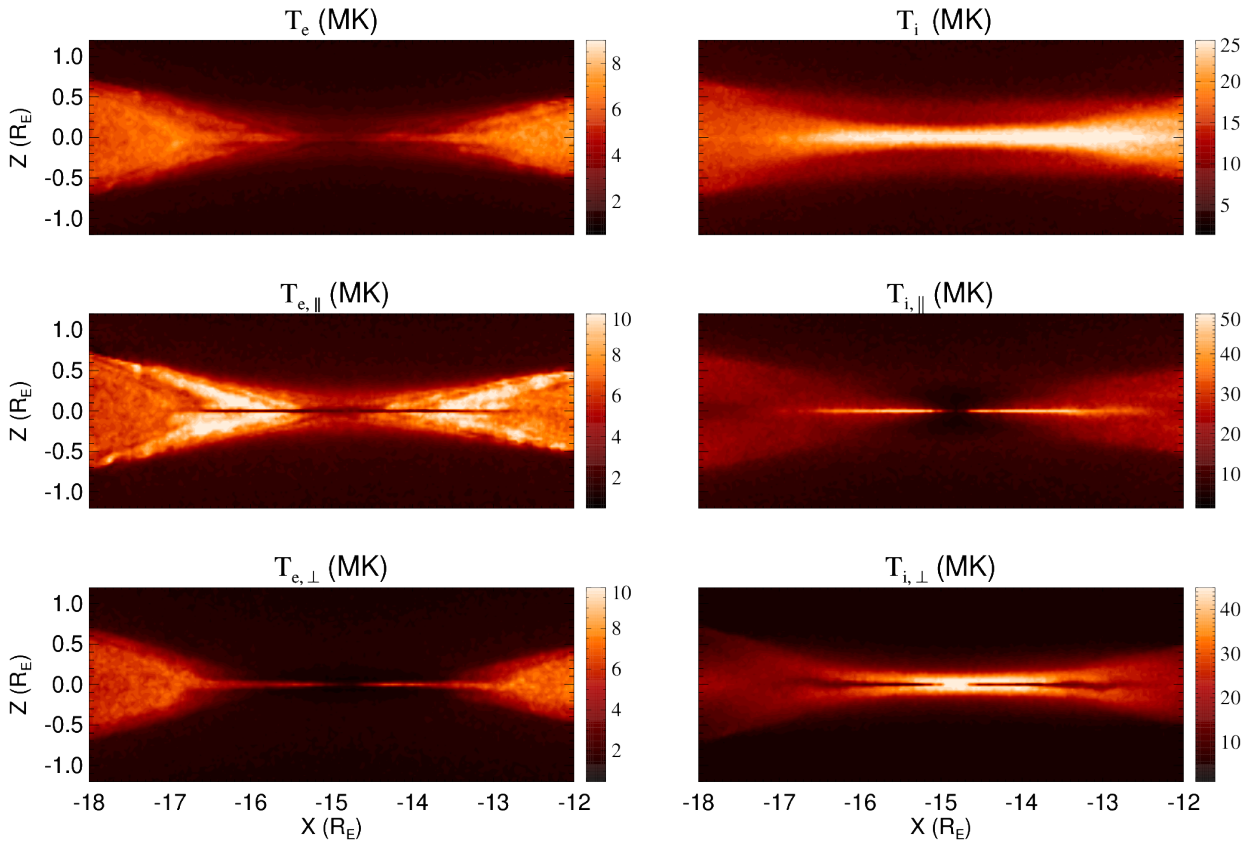


Figure 3.15: Total, parallel, and perpendicular electron and ion temperatures at t = 92 minutes. The electrons are heated preferentially in the perpendicular direction near the neutral line, while the ions are heated preferentially in the parallel direction near the neutral line.

Unlike electrons, the total ion temperature is higher near the neutral line in the outflow region, and the ions are heated preferentially in the parallel direction near the neutral line, while the perpendicular ion temperature is lower near the neutral line. These results are consistent with previous PIC studies [49]. For both electrons and ions, the total, parallel, and perpendicular temperatures are somewhat higher on the Earthward side of the reconnection site compared to the tailward side. Earth's strong intrinsic magnetic field creates an obstacle to the ion and electron jets, slowing them down and heating them up. This temperature asymmetry is more apparent for electrons than for ions.

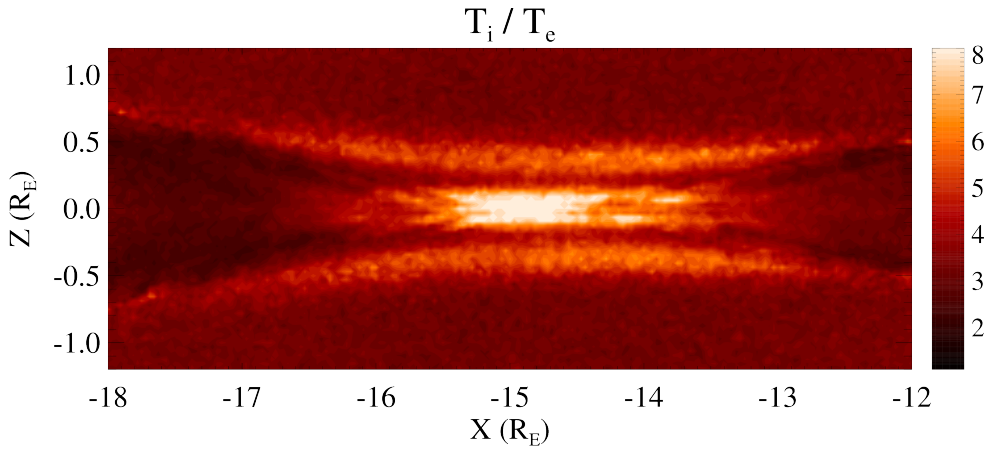


Figure 3.16: The ratio of ion to electron temperature at t = 92 minutes. The ion temperature in the electron diffusion region can be roughly 8 to 10 times higher than the electron temperature.

As shown in Figure 3.16, the ion temperature in the electron diffusion region can be roughly 8 to 10 times higher than the electron temperature. This ratio dramatically decreases away from the diffusion region to 5 in the immediate outflow and to $\approx 2-3$ in the far outflow region.

3.4 Conclusions

In this study, we have investigated the onset of magnetic reconnection in Earth's magnetotail using a coupled MHD-PIC model. We have performed a systematic parameter study to determine the optimal PIC parameters to accurately capture reconnection onset, including grid resolution, ion-electron mass ratio, and kinetic scaling factor. Our results show that resolving electron scales is crucial for accurately capturing the timing and location of reconnection onset, as well as the current sheet thickness at onset. We find that a grid resolution of roughly 1.5 cells per electron inertial length is sufficient to achieve convergence in reconnection properties. Additionally, we find that a kinetic scaling factor of $f = 16$ and an ion-electron mass ratio of $m_i/m_e = 100$ are optimal for studying reconnection onset in the magnetotail while offering significant computational savings compared to more realistic parameters. Finally, we demonstrate that both ideal and Hall MHD simulations fail to capture the true physics of reconnection and the results are grid dependent, while our coupled MHD-PIC model successfully captures the electron-scale physics that governs reconnection onset in the magnetotail. In the future, we plan to use the newly developed semi-implicit AMR-PIC model [2, 12] to resolve the electron scales only in a small region around the re-

connection site to save computational resources while still accurately capturing the physics of reconnection onset. We then plan to use our MHD with an embedded AMR-PIC model to study the onset of reconnection in the 3D magnetotail with the optimal PIC parameters identified in this study.

CHAPTER 4

Modeling Tail Reconnection Onset with AMR-PIC

This chapter focuses on using the AMR-PIC method discussed in Chapter 2 to reproduce the results of the reconnection onset problem studied in Chapter 3. The goal is to show that the AMR-PIC method can accurately capture electron-scale physics locally while maintaining similar results to the uniform grid PIC method globally.

4.1 Simulation Setup

The setup for the AMR-PIC simulation is exactly the same as the uniform grid MHD-EPIC simulation described in Chapter 3 with $\Delta x_0 = 1/16R_E$, scaling factor $f = 16$, and mass ratio $m_i/m_e = 100$. The only difference is that an AMR grid with $\Delta x_1 = 1/32R_E$ spanning from $-38R_E < x < -10R_E$ and $-2.5R_E < y < 2.5R_E$ (Figure 4.1) has been added. These runs will be compared against the uniform grid PIC run with $\Delta x = 1/32R_E$ discussed in section 3.3.7

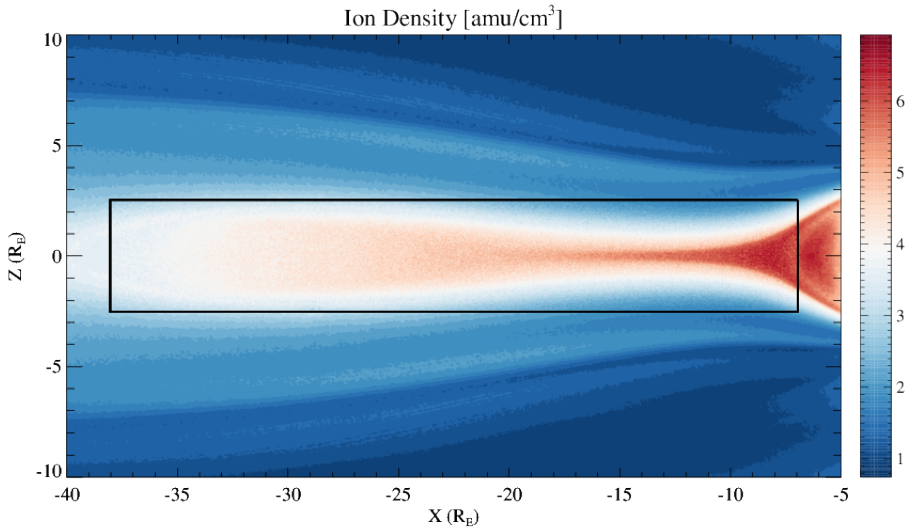


Figure 4.1: AMR grid setup for the reconnection onset problem. The black rectangle represents the refined region.

4.2 Results

4.2.1 Timing and Location of Reconnection Onset

To establish the validity of the AMR-PIC method, we first compare the timing and location of reconnection onset between the uniform grid and AMR runs.

Table 4.1: Timing and location of reconnection onset for uniform grid and AMR-PIC simulations.

Simulation	Onset time [min]	Onset location [R_E]	Thickness [R_E]
Uniform grid	83 and 85	-16.5 and -13.4	0.15
AMR	83	-15.4	0.15

Table 4.1 shows that the reconnection onset time and location are very similar between the uniform grid and AMR runs. The AMR and uniform grid reconnect at the same time at 83 minutes. The uniform grid reconnects at $-16.5R_E$ at 83 minutes and has a second reconnection site forming at 85 minutes at $-13.4R_E$. While the AMR run has a single reconnection site forming at 83 minutes at $-15.4R_E$. The occurrence of dual reconnection sites is discussed in Chapter 3. It is a somewhat random process since the system has multiple locations where reconnection sites can form. The fact that the AMR run has a single reconnection site while the uniform grid run has two reconnection sites is not surprising, since the formation of a dual reconnection site is very sensitive to small perturbations. The current sheet thickness at the reconnection site at the onset time is consistent between both runs, which shows that the electron scales are resolved in both runs.

4.2.2 Before Reconnection Onset

As shown in Figure 4.2, the plasma properties like electron number density, electron velocity, ion velocity, electron pressure, ion pressure, and out-of-plane current density just before reconnection at t=80 minutes are very similar between the uniform grid and AMR runs.

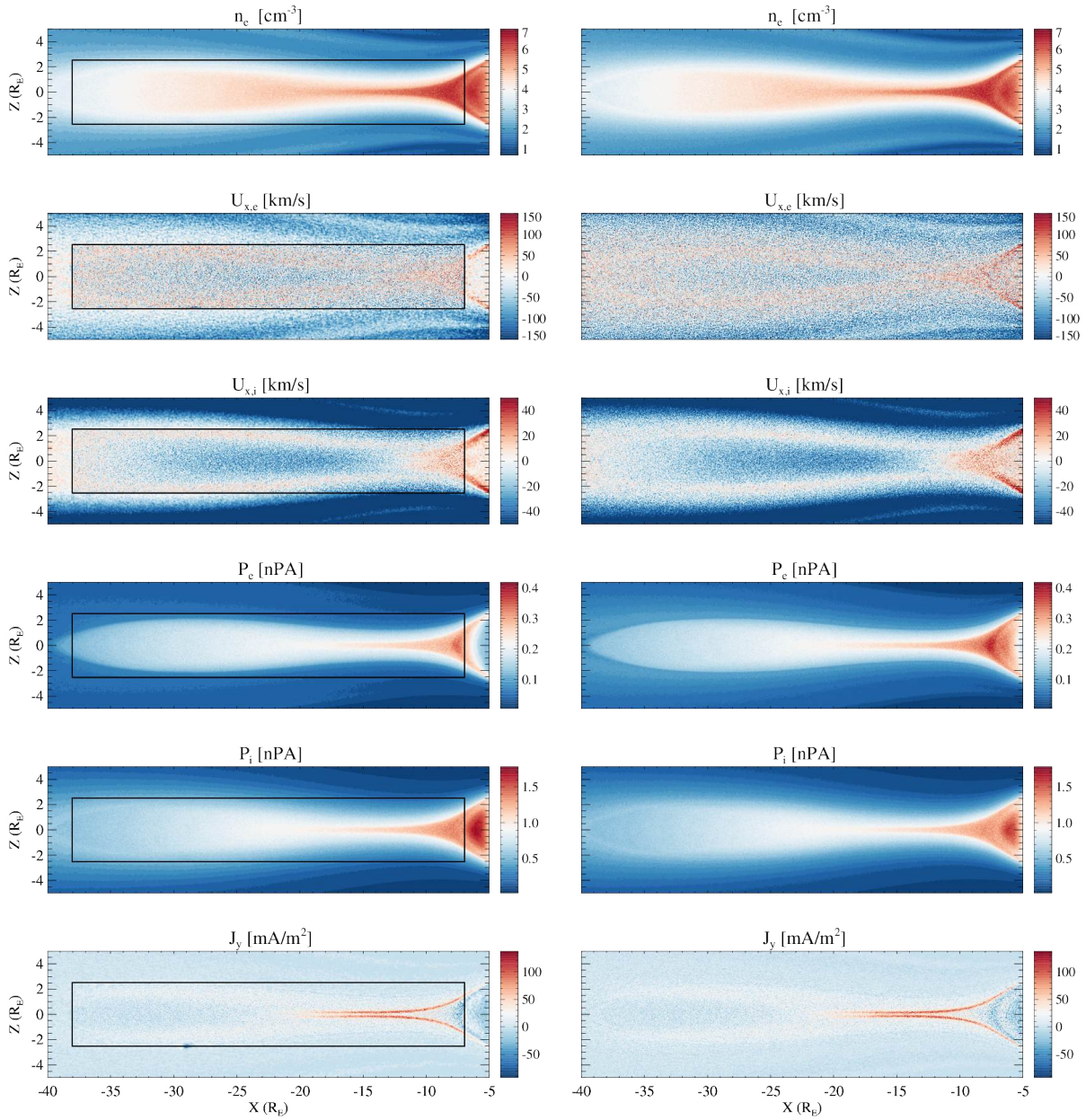


Figure 4.2: Comparison of electron number density, electron velocity, ion velocity, electron pressure, ion pressure, and out-of-plane current density between uniform grid (right) and AMR-PIC (left) simulations at 80 minutes, before reconnection onset. Refined region is outlined by the black rectangle.

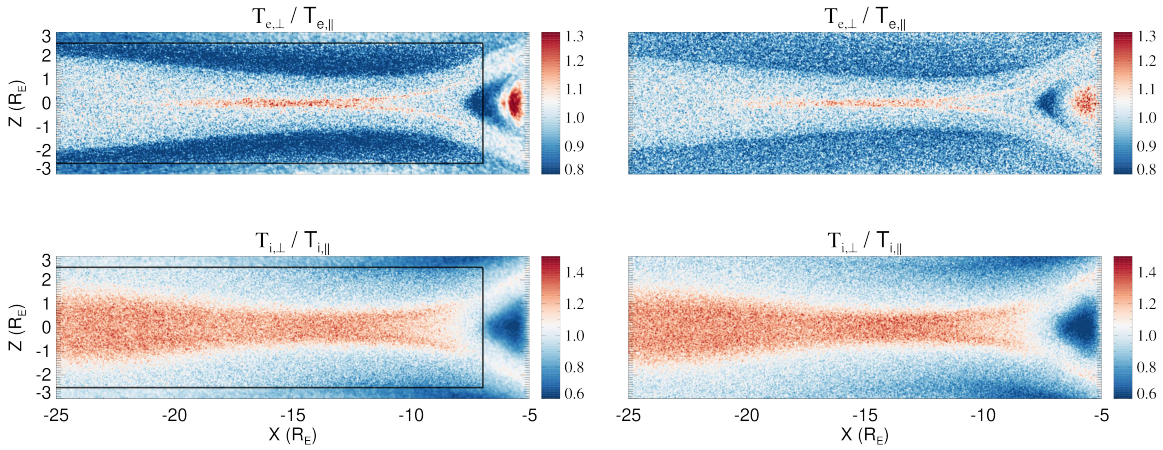


Figure 4.3: Comparison of electron and ion temperature anisotropy between uniform grid (right) and AMR-PIC (left) simulations at 82 minutes, before reconnection onset. Refined region is outlined by the black rectangle.

Figure 4.3 shows the comparison of ion and electron temperature anisotropy between the uniform grid and AMR runs at 82 minutes, just before reconnection onset. The temperature anisotropies are very similar between the two runs. The electron temperature anisotropy is also consistent with the findings of [36]. This again demonstrates that localized resolution of electron-scale physics can capture similar physics as a uniform grid PIC run.

4.2.3 After Reconnection Onset

At t=85 minutes after reconnection onset, the uniform grid simulation still has a dual reconnection structure while the AMR simulation has a single reconnection site as shown in Figure 4.4, but all properties like electron number density, electron velocity, and ion velocity are very similar between both runs.

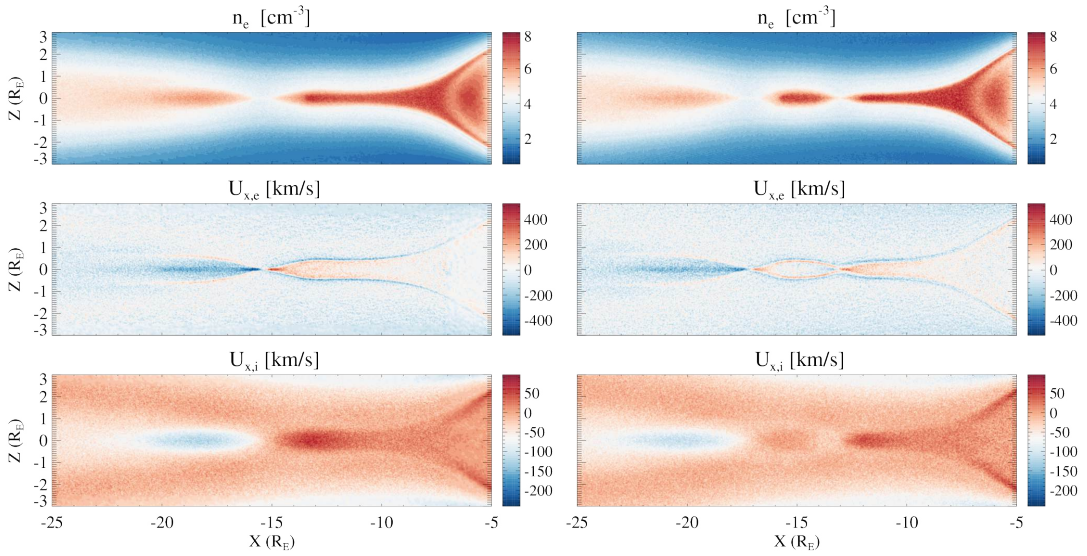


Figure 4.4: Comparison of electron number density, electron velocity, and ion velocity between uniform grid (right) and AMR-PIC (left) simulations at 85 minutes, after reconnection onset.

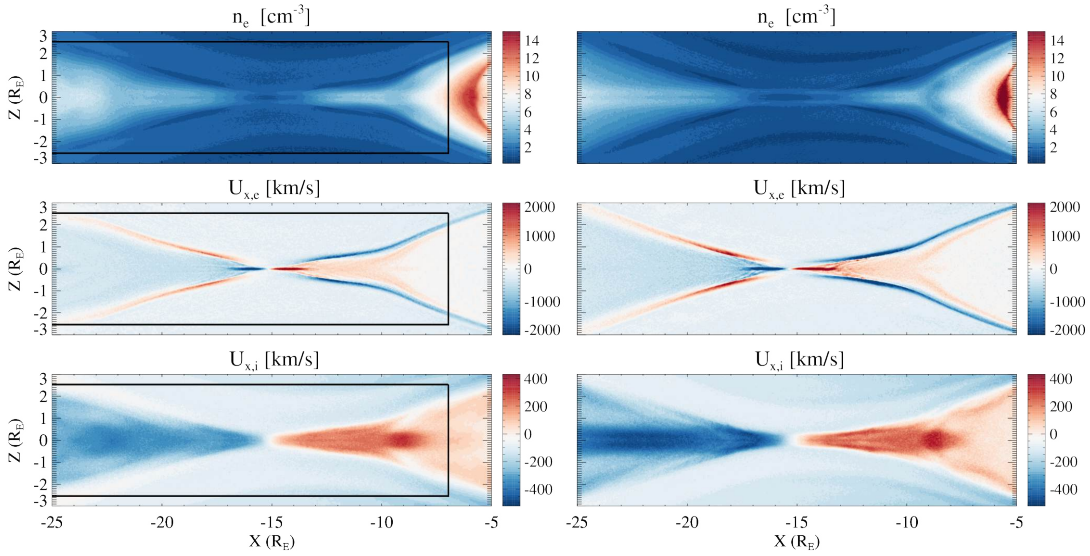


Figure 4.5: Comparison of electron number density, electron velocity, and ion velocity between uniform grid (right) and AMR-PIC (left) simulations at 92 minutes, after reconnection onset. Refined region is outlined by the black rectangle.

Figure 4.5 shows the electron number density, electron velocity, and ion velocity at 92 minutes after reconnection onset. By this time, the reconnection site in the uniform grid

run that was closer to the Earth has dominated and pushed the other reconnection site further down the tail. Both the AMR and uniform grid runs have a single reconnection site at roughly the same location, and the number density, electron, and ion velocities are very similar between both runs. This further cements the fact that the AMR-PIC method can capture localized electron-scale physics and produces similar results to a uniform grid PIC method globally. This also shows that the formation of dual reconnection sites is a short-lived process, and the system eventually settles to a single reconnection site.

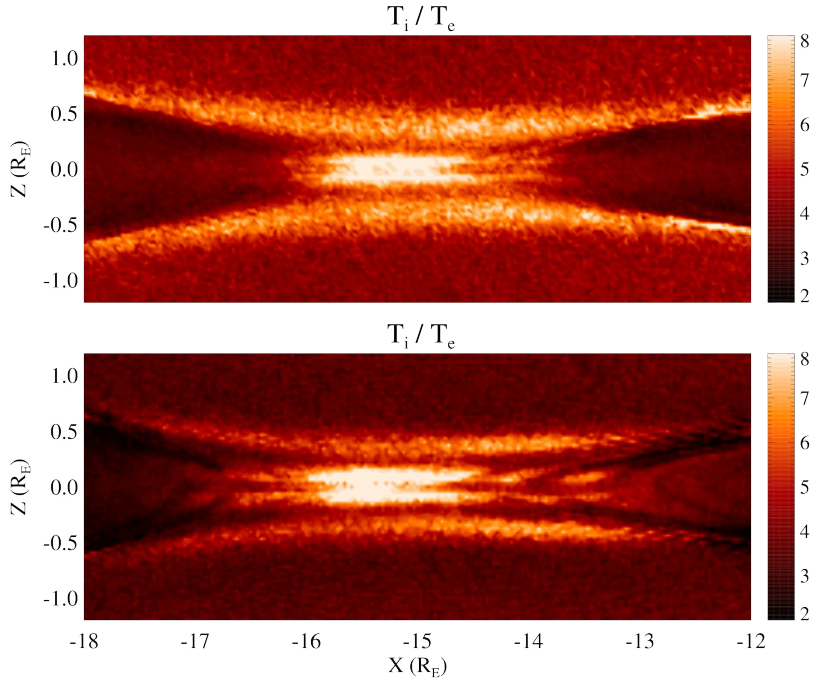


Figure 4.6: Comparison of ion to electron temperature ratio between uniform grid (top) and AMR-PIC (bottom) simulations at 92 minutes, after reconnection onset.

Figure 4.6 shows the comparison of the ion to electron temperature ratio between the uniform grid and AMR runs at 92 minutes. Both cases have a temperature ratio of roughly 8 in the electron diffusion region, which falls off rapidly to roughly 4 in the outflow region.

CHAPTER 5

Conclusion and Future Work

This thesis focuses on the development and integration of a novel semi-implicit particle-in-cell method with adaptive mesh refinement (AMR-PIC) into the Magnetohydrodynamics with Embedded Particle-in-Cell (MHD-EPIC) framework. The AMR-PIC method is based on the Gauss's Law Satisfying Energy Conserving Semi-Implicit Method (GL-ECSIM) [14]. AMR-PIC allows for local grid refinement in regions of interest, such as the reconnection sites, while maintaining a coarser grid elsewhere. This significantly reduces the computational cost compared to uniform-grid PIC methods. The AMR-PIC method also couples the electromagnetic fields as well as particle distribution functions across all refinement levels. The AMR-PIC method is implemented in the MHD-EPIC framework, which enables the resolution of all scales of interest ranging from the global MHD scales to the local electron scales in a self-consistent manner.

The near-Earth magnetotail reconnection onset problem is studied using the MHD-EPIC model with a uniform PIC grid. A robust convergence criterion (1.5 cells per electron inertial length d_e) is established for resolving electron scales in the reconnection onset problem. A multi-parameter scaling study is performed by studying the effect of the kinetic scaling factor f and the ion-to-electron mass ratio m_i/m_e on the reconnection onset problem. It was concluded that a kinetic scaling factor of $f = 16$ and a reduced ion-to-electron mass ratio of $m_i/m_e = 25$ are sufficient to accurately reproduce the global dynamics associated with the reconnection onset. It was also shown that the current sheet universally thins down to roughly $\sim 3d_e$ before the onset of reconnection. We found that an electron temperature anisotropy of $T_{e\perp}/T_{e\parallel} \sim 1.1 - 1.3$ is developed near the neutral line just before reconnection onset. Finally, the AMR-PIC model is used to reproduce the same results as a uniform-grid PIC simulations while using a coarser grid in the PIC region and only refining the grid locally to resolve the 1.5 cells per d_e criterion near the reconnection site.

Future work includes implementation of temporal subcycling to improve the efficiency of the AMR-PIC method. This will enable the coarse regions to take larger time steps

while the refined regions take smaller ones. Another important future step is determining dynamic refinement criteria for the AMR-PIC method so that the refined region can follow the reconnection site as it moves. Once suitable refinement criteria are found, the AMR-PIC model can be used to study the onset of reconnection in 3D using the optimal parameters and convergence criteria determined in this thesis.

The AMR-PIC method will also be used to study dayside magnetic reconnection, where electron-scale processes play a critical role in controlling energy transfer from the solar wind into the magnetosphere. Beyond magnetotail and dayside reconnection, the AMR-PIC framework has the potential to address a wide range of space plasma problems like magnetic reconnection in the magnetosheath and cusp regions, kinetic processes associated with dipolarization fronts and bursty bulk flows in the magnetotail. Broadly speaking, the AMR-PIC method can be used to study any space/astrophysical/laboratory plasma problem which involves kinetic processes. The ability to selectively resolve electron-scale physics only where required makes AMR-PIC particularly attractive for multi-scale physics problems in which kinetic processes are confined to relatively small regions but strongly influence global plasma dynamics.

BIBLIOGRAPHY

[1] Hannes Alfvén. Existence of electromagnetic-hydrodynamic waves. Nature, 150:405–406, 1942.

[2] Talha Arshad, Yuxi Chen, and Gábor Tóth. Adaptive mesh refinement in semi-implicit particle-in-cell method. Computer Physics Communications, 316:109806, 2025.

[3] Nicolas Aunai, Roch Smets, Andrea Ciardi, Philip Deegan, Alexis Jeandet, Thibault Payet, Nathan Guyot, and Loic Darrieumerlou. Phare: Parallel hybrid particle-in-cell code with patch-based adaptive mesh refinement. Computer Physics Communications, 295:108966, 2024.

[4] Fabio Bacchini. Relsim: A relativistic semi-implicit method for particle-in-cell simulations. The Astrophysical Journal Supplement Series, 268(2):60, oct 2023.

[5] L. Biermann. Kometenschweife und solare korpuskularstrahlung. Zeitschrift für Astrophysik, 29:274, 1951.

[6] J. Birn and M. Hesse. Forced reconnection in the near magnetotail: Onset and energy conversion in pic and mhd simulations. Journal of Geophysical Research: Space Physics, 119(1):290–309, 2014.

[7] Joachim Birn and Eric R. Priest. Reconnection of Magnetic Fields: Magnetohydrodynamics and Collisionless Theory and Observations. Cambridge University Press, Cambridge, 2007.

[8] J.U. Brackbill and D. Forslund. An implicit method for electromagnetic plasma simulation in two dimensions. J. Comput. Phys., 46:271–308, 1982.

[9] Martin Campos Pinto and Valentin Pagès. A semi-implicit electromagnetic fem-pic scheme with exact energy and charge conservation. Journal of Computational Physics, 453:110912, 2022.

[10] G. Chen and L. Chacón. An implicit, conservative and asymptotic-preserving electrostatic particle-in-cell algorithm for arbitrarily magnetized plasmas in uniform magnetic fields. Journal of Computational Physics, 487:112160, 2023.

[11] Y. Chen, G. Tóth, P. Cassak, X. Jia, T. I. Gombosi, J. Slavin, S. Markidis, and B. Peng. Global three-dimensional simulation of earth's dayside reconnection using a two-way

coupled magnetohydrodynamics with embedded particle-in-cell model: initial results. J. Geophys. Res., 122:10318, 2017.

[12] Yuxi Chen, Gábor Tóth, Erick Powell, Talha Arshad, Ethan Bair, Marc Kornbleuth, and Merav Opher. A kinetic-magnetohydrodynamic model with adaptive mesh refinement for modeling heliosphere neutral-plasma interaction. The Astrophysical Journal, 973(1):46, 2024.

[13] Yuxi Chen, Gábor Tóth, Hongyang Zhou, and Xiantong Wang. FLEKS: A flexible particle-in-cell code for multi-scale plasma simulations. Comp. Phys. Comm., 287:108714, 2023.

[14] Yuxi Chen and Gábor Tóth. Gauss's law satisfying energy-conserving semi-implicit particle-in-cell method. Journal of Computational Physics, 386:632–652, 2019.

[15] Phillip Colella and Peter C. Norgaard. Controlling self-force errors at refinement boundaries for amr-pic. JCP, 229:947–957, 2010.

[16] L. K. S. Daldorff, G. Tóth, T. I. Gombosi, G. Lapenta, J. Amaya, S. Markidis, and J. U. Brackbill. Two-way coupling of a global Hall magnetohydrodynamics model with a local implicit Particle-in-Cell model. J. Comput. Phys., 268:236, 2014.

[17] J. W. Dungey. Interplanetary magnetic field and the auroral zones. Phys. Rev. Lett., 6:47–48, Jan 1961.

[18] J P Eastwood, H Hietala, G Toth, T D Phan, and M Fujimoto. What controls the structure and dynamics of earth's magnetosphere? Space Sci. Rev., 188(1-4):251–286, 2015.

[19] X. R. Fu, Q. M. Lu, and S. Wang. The process of electron acceleration during collisionless magnetic reconnection. Physics of Plasmas, 13(1):012309, 01 2006.

[20] K. Fujimoto and S. Machida. Full particle simulation of the plasma sheet using adaptive mesh refinement technique. Adv. Space Res., 37(7):1348–1353, 2006. Reconnection at Sun and in Magnetospheres.

[21] Keizo Fujimoto. A new electromagnetic particle-in-cell model with adaptive mesh refinement for high-performance parallel computation. J. Comput. Phys., 230(23):8508–8526, 2011.

[22] Diego Gonzalez-Herrero, Elisabetta Boella, and Giovanni Lapenta. Performance analysis and implementation details of the energy conserving semi-implicit method code (ecsim). Computer Physics Communications, 229:162–169, 2018.

[23] Diego Gonzalez-Herrero, Alfredo Micera, Elisabetta Boella, Jaeyoung Park, and Giovanni Lapenta. Ecsim-cyl: Energy conserving semi-implicit particle in cell simulation in axially symmetric cylindrical coordinates. Computer Physics Communications, 236:153–163, 2019.

[24] M. Hoshino, T. Mukai, T. Terasawa, and I. Shinohara. Suprathermal electron acceleration in magnetic reconnection. Journal of Geophysical Research: Space Physics, 106(A11):25979–25997, 2001.

[25] Can Huang, Quanming Lu, and Shui Wang. The mechanisms of electron acceleration in antiparallel and guide field magnetic reconnection. Physics of Plasmas, 17(7):072306, 07 2010.

[26] M. Hubbert, Y. Qi, C. T. Russell, J. L. Burch, B. L. Giles, and T. E. Moore. Electron-only tail current sheets and their temporal evolution. Geophysical Research Letters, 48(5):e2020GL091364, 2021. e2020GL091364 2020GL091364.

[27] M. Hubbert, C. T. Russell, Yi Qi, S. Lu, J. L. Burch, B. L. Giles, and T. E. Moore. Electron-only reconnection as a transition phase from quiet magnetotail current sheets to traditional magnetotail reconnection. Journal of Geophysical Research: Space Physics, 127(3):e2021JA029584, 2022. e2021JA029584 2021JA029584.

[28] A J Hundhausen. Coronal expansion and solar wind. Physics and Chemistry in Space. Springer, Berlin, Germany, 1972 edition, November 1972.

[29] R D Hunsucker and J K Hargreaves. Preface. In The High-Latitude Ionosphere and its Effects on Radio Propagation. Cambridge University Press, Cambridge, October 2002.

[30] M.E. Innocenti, A. Beck, S. Markidis, and G. Lapenta. Momentum conservation in multi-level multi-domain (mlmd) simulations. J. Comput. Phys., 312:14–18, 2016.

[31] M.E. Innocenti, G. Lapenta, S. Markidis, A. Beck, and A. Vapirev. A multi level multi domain method for particle in cell plasma simulations. J. Comput. Phys., 238:115, 2013.

[32] Revathi Jambunathan, Henry Jones, Lizzette Corrales, Hannah Klion, Michael E. Rowan, Andrew Myers, Weiqun Zhang, and Jean-Luc Vay. Application of mesh refinement to relativistic magnetic reconnection. Physics of Plasmas, 32:013905, 01 2025.

[33] Giovanni Lapenta. Exactly energy conserving semi-implicit particle in cell formulation. Journal of Computational Physics, 334:349–366, 2017.

[34] Giovanni Lapenta. Advances in the implementation of the exactly energy conserving semi-implicit (ecsim) particle-in-cell method. Physics, 5(1):72–89, 2023.

[35] L C Lee and K H Lee. Fluid and kinetic aspects of magnetic reconnection and some related magnetospheric phenomena. Rev. Mod. Plasma Phys., 4(1), 2020.

[36] Yi-Hsin Liu, Joachim Birn, William Daughton, Michael Hesse, and Karl Schindler. Onset of reconnection in the near magnetotail: Pic simulations. Journal of Geophysical Research: Space Physics, 119(12):9773–9789, 2014.

[37] Quanming Lu, Can Huang, Jinlin Xie, Rongsheng Wang, Mingyu Wu, Andris Vaivads, and Shui Wang. Features of separatrix regions in magnetic reconnection: Comparison of 2-d particle-in-cell simulations and cluster observations. Journal of Geophysical Research: Space Physics, 115(A11), 2010.

[38] San Lu, Quanming Lu, Rongsheng Wang, Philip L. Pritchett, Mark Hubbert, Yi Qi, Kai Huang, Xinmin Li, and C. T. Russell. Electron-only reconnection as a transition from quiet current sheet to standard reconnection in earth's magnetotail: Particle-in-cell simulation and application to mms data. Geophysical Research Letters, 49(11):e2022GL098547, 2022. e2022GL098547 2022GL098547.

[39] A. T. Y. Lui. Potential plasma instabilities for substorm expansion onsets. Space Science Reviews, 113(1-2):127–206, 2004.

[40] S. Markidis, G. Lapenta, and Rizwan-Uddin. Multi-scale simulations of plasma with ipic3d. Mathematics and Computers in Simulation, 80:1509–1519, 2010.

[41] Rumi Nakamura, Wolfgang Baumjohann, Andrei Runov, and Yoshifumi Asano. Thin current sheets in the magnetotail observed by cluster. Space Science Reviews, 122(1-4):29–38, 2006.

[42] E N Parker. Dynamical theory of the solar wind. Space Sci. Rev., 4(5-6), September 1965.

[43] Eugene N. Parker. Dynamics of the interplanetary gas and magnetic fields. The Astrophysical Journal, 128:664–676, 1958.

[44] Tai D Phan, Jonathan P Eastwood, MA Shay, JF Drake, BU Ö Sonnerup, Masaki Fujimoto, PA Cassak, M Øieroset, JL Burch, RB Torbert, et al. Electron magnetic reconnection without ion coupling in earth's turbulent magnetosheath. Nature, 557(7704):202–206, 2018.

[45] P. L. Pritchett. Externally driven magnetic reconnection in the presence of a normal magnetic field. Journal of Geophysical Research: Space Physics, 110(A5), 2005.

[46] P. L. Pritchett. Onset of magnetic reconnection in the presence of a normal magnetic field: Realistic ion to electron mass ratio. Journal of Geophysical Research: Space Physics, 115(A10), 2010.

[47] P. Ricci, G. Lapenta, and J. U. Brackbill. A simplified implicit maxwell solver. J. Comput. Phys., 183:117, 2002.

[48] M. A. Shay, J. F. Drake, B. N. Rogers, and R. E. Denton. The scaling of collisionless, magnetic reconnection for large systems. Geophysical Research Letters, 26(14):2163–2166, 1999.

[49] M. A. Shay, C. C. Haggerty, T. D. Phan, J. F. Drake, P. A. Cassak, P. Wu, M. Oieroset, M. Swisdak, and K. Malakit. Electron heating during magnetic reconnection: A simulation scaling study. Physics of Plasmas, 21(12):122902, 2014.

[50] Yinsi Shou, Valeriy Tenishev, Yuxi Chen, Gabor Toth, and Natalia Ganushkina. Magnetohydrodynamic with adaptively embedded particle-in-cell model: MHD-AEPIC. J. Comput. Phys., 446:110656, 2021.

[51] Mikhail I. Sitnov, Joachim Birn, Banafsheh Ferdousi, Evgeny Gordeev, Yuri Khotyaintsev, Viacheslav Merkin, Tetsuo Motoba, Antonius Otto, Evgeny Panov, Philip Pritchett, Fulvia Pucci, Joachim Raeder, Andrei Runov, Victor Sergeev, Marco Velli, and Xuzhi Zhou. Explosive magnetotail activity. Space Science Reviews, 215(4):31, 2019.

[52] Conway W. Snyder and Marcia Neugebauer. Interplanetary solar-wind measurements by mariner ii. In Proceedings of the Plasma Space Science Symposium, pages 67–90. Springer Netherlands, 1965.

[53] Susanne F. Spinnangr, Michael Hesse, Paul Tenfjord, Cecilia Norgren, Håkon M. Kolstø, Norah K. Kwagala, Therese Moretto Jørgensen, and Tai Phan. Electron behavior around the onset of magnetic reconnection. Geophysical Research Letters, 49(23):e2022GL102209, 2022. e2022GL102209 2022GL102209.

[54] William T. Taitano, Dana A. Knoll, Luis Chacón, and Guangye Chen. Development of a consistent and stable fully implicit moment method for vlasov–ampère particle in cell (pic) system. SIAM Journal on Scientific Computing, 35(5):S126–S149, 2013.

[55] Gábor Tóth, Yuxi Chen, Tamas I. Gombosi, Paul Cassak, Stefano Markidis, and Ivy Bo Peng. Scaling the ion inertial length and its implications for modeling reconnection in global simulations. Journal of Geophysical Research: Space Physics, 122(10):10,336–10,355, 2017.

[56] Hideyuki Usui, Masanori Nunami, Toseo Moritaka, Tatsuki Matsui, and Yohei Yagi. A multi-scale electromagnetic particle code with adaptive mesh refinement and its parallelization. Procedia Computer Science, 4:2337–2343, 2011. Proceedings of the International Conference on Computational Science, ICCS 2011.

[57] M Vass, P Palla, and P Hartmann. Revisiting the numerical stability/accuracy conditions of explicit pic/mcc simulations of low-temperature gas discharges. Plasma Sources Science and Technology, 31(6):064001, jun 2022.

[58] J.-L. Vay, A. Almgren, J. Bell, L. Ge, D.P. Grote, M. Hogan, O. Kononenko, R. Lehe, A. Myers, C. Ng, J. Park, R. Ryne, O. Shapoval, M. Thévenet, and W. Zhang. Warp-x: A new exascale computing platform for beam–plasma simulations. Nuclear Instruments and Methods in Physics Research, 909:476–479, 2018. 3rd European Advanced Accelerator Concepts workshop (EAAC2017).

[59] J.-L. Vay, P. Colella, P. McCorquodale, B. van Straalen, A. Friedman, and D.P. Grote. Mesh refinement for particle-in-cell plasma simulations: Applications to and benefits for hea vy ion fusion. Laser and Particle Beams, 20:569–575, 2003.

[60] Rongsheng Wang, Quanming Lu, San Lu, Christopher T. Russell, J. L. Burch, Daniel J. Gershman, W. Gonzalez, and Shui Wang. Physical implication of two types of reconnection electron diffusion regions with and without ion-coupling in the magnetotail current sheet. Geophysical Research Letters, 47(21):e2020GL088761, 2020. e2020GL088761 2020GL088761.

[61] Masaaki Yamada, Russell Kulsrud, and Hantao Ji. Magnetic reconnection. Rev. Mod. Phys., 82:603–664, Mar 2010.

[62] Weiqun Zhang, Ann Almgren, Vince Beckner, John Bell, Johannes Blaschke, Cy Chan, Marcus Day, Brian Friesen, Kevin Gott, Daniel Graves, et al. Amrex: a framework for block-structured adaptive mesh refinement. The Journal of Open Source Software, 4(37):1370, 2019.